An Integrated Microelectronic Device for Biomolecular Amplification and Detection

by

Chih-Sheng Johnson Hou

B.S. Engineering: Biomedical Informatics
Stanford University, 2003
M.S. Electrical Engineering
Stanford University, 2003

Submitted to the Department of Electrical Engineering and Computer Science
in partial fulfillment of the requirements for the degree of

Doctor of Philosophy in Electrical Engineering and Computer Science

at the

MASSACHUSETTS INSTITUTE OF TECHNOLOGY

Feb 2007

Author .....
Department of Electrical Engineering and Computer Science
Feb 5, 2007

Certified by .....
Scott Manalis
Associate Professor, Biological Engineering and Mechanical Engineering
Thesis Supervisor

Accepted by .....
Arthur C. Smith
Chairman, Department Committee on Graduate Students

An Integrated Microelectronic Device for Biomolecular Amplification and Detection

by

Chih-Sheng Johnson Hou

Submitted to the Department of Electrical Engineering and Computer Science
on Feb 5, 2007, in partial fulfillment of the
requirements for the degree of
Doctor of Philosophy in Electrical Engineering and Computer Science

Abstract

The extraordinarily high sensitivity, large dynamic range and reproducibility of polymerase chain reaction (PCR) have made it one of the most widely used techniques for analyzing nucleic acids. As a result, considerable effort has been directed towards developing miniaturized systems for PCR, but most rely on off-chip optical detection modules that are difficult to miniaturize into a compact analytical system and fluorescent product markers that can require extensive effort to optimize. This thesis presents a robust and simple method for direct label-free PCR product quantification using a microelectronic sensor. The thesis covers the design, fabrication, and characterization of the sensing technique and its integration with PCR microfluidics into a monolithic detection platform.

The sensor used in this thesis study is an electrolyte-insulator-silicon (EIS) device fabricated on planar silicon substrates. Based on electronic detection of layer-by-layer assembly of polyelectrolytes, the sensing technique can specifically quantify double-stranded DNA product in unprocessed samples and monitor the product concentration at various stages of PCR to generate readout analogous to that of a real-time fluorescent measurement. Amplification is achieved with integrated metal resistive heaters, temperature sensors, and microfluidic valves. Direct electronic quantification of the product on-chip yields analog surface potential signals that can be converted to a digital true/false readout.

A silicon field-effect sensor for direct detection of heparin by its intrinsic negative charge has also been developed. Detection of heparin and heparin-based drugs in buffer and serum has been studied, and a study demonstrating strong correlation between electronic heparin sensing measurements and those from a colorimetric assay for heparin-mediated anti-Xa activity has been performed.

Thesis Supervisor: Scott Manalis
Title: Associate Professor, Biological Engineering and Mechanical Engineering

Acknowledgments

This journey would not have possible without the opportunities and support my research advisor, Prof. Scott Manalis, has given me to work with his Nanoscale Sensing group. Always open-minded and enthusiastic, Scott has given me not only the technical trainings to advance knowledge in our field, but more importantly the mentality to survive and conquer uncertainties and difficult times.

My most profound thanks also go to Prof. Dennis Freeman and Prof. Jongyoon Han, who have also helped me develop the numerous skills needed for my engineering career in their class 6.021 and as well as in their roles as my PhD committee members. I would also like to thank Prof. Marty Schmidt for providing guidance and insight in the 6.151 microfabrication project class that helped launch my graduate research.

I have been extremely fortunate to work with a group of very fun, diverse, talented, and inspiring labmates. With boundless creativity and humor, Dr. Nebojsa 'Nebo' Milovic has always been able to brighten up my day and do magic to my microfluidic sensor setup. 'Vial 91' and 'Shurek' are 'nice'! I would also like to thank Dr. Michel Godin for his indispensable contribution to the peltier temperature controller and a euphonious email notification message. Kristofor Payer has provided the most instrumental assistance in materializing fabrication processes that I once thought existed only on paper. Tzu-Liang Loh has taught me the meticulousness to do well in microfabrication and engineering characterization in general. Dr. Thomas Burg, Rumi Chunara, Dr. Will Grover, Dr. Scott Knudsen, Phil Dextras, Maxim Shusteff, Peter Russo, Dr. Andrew Sparks, Dr. Leo Alexopoulos, and the newbie labbers have also each helped me with various aspects of my graduate work and most importantly, make me feel as a member of a warm, close-knit community.

I would like to thank Laureen Chapman, and former administrative assistants Janet Stezzi, Tracy Skeete, and Michael Houlihan for facilitating the acquisitions of the numerous toys for my research, and making things run smoothly in general.

I thank the MIT Microsystems Technology Laboratories staff, particularly Dr.

Vicky Diadiuk, Paul Tierny, Dr. Li-Wen Wang, Kurt Broderick, Bob Bicchieri, Dan Adams, and Dave Terry for assisting me in microfabrication and making my clean-room experience that much more enjoyable. Without their help, the thesis project would not have been possible. I am also privileged to meet student members including Ole Nielsen, Bernard Yen, Ying-Chih Wang, Valerie Leblanc, Stephen Hou, Brian Chow, Tyrone Hill, David Kong, Manu Prakash, and Brian Tang, with whom I share the joy and tears of life in the fab. I would also like to thank Dr. Manlin Luo in MIT BioMicro Center and Dr. Peter Carr in the Media Lab for their indispensable help in the DNA sensing work.

This work has been funded by an Institute Fellowship, Air Force Office of Scientific Research, the NSF Center for Bits and Atoms, and the Hewlett-Packard Corporation.

Without doubt, my sojourn to MIT is not possible without the love and care of my family. Encouraging me to be adventurous, my parents have always given me the unqualified support and intellectual freedom to pursue my passion. Living half a globe away, they are nevertheless always able to provide timely support to help me endure the most difficult and insipid periods of graduate research and share the joys of occasional breakthroughs with me. I would like to thank Pei-Shan for warming my heart with her quiet but genuine affection. My brother Jack, coming from very different academic trainings, and (unfortunately) a Yankees fan, is always fun to hang out with and learn something from, and serves his duty as a younger brother well by reminding me that there is a world and life outside of the lab.

Thanks for the memories

Contents

List of Figures

List of Tables

Chapter 1

Introduction

This thesis explores the integration of biochemical signal amplification functionality to a microfabricated field-effect sensor platform for the specific quantification of biomolecules in a complex mixture. This chapter provides an introduction to biosensor technology, and presents a survey of recent developments in label-based optical DNA sensing and signal amplification methods that enable the measurements of nucleic acids at an unprecedented rate, parallelism, resolution, and accuracy. After reviewing key developments in benchtop nucleic acid analytical systems, the chapter will examine the advantages and challenges of scaling down the tools for point-of-care diagnostics and on-site testing. A survey of various label-free sensing techniques will be provided, and the prospect of integrating the label-free sensors with sample preparation functions will be studied. The motivation of this thesis work will be presented, and the chapter will conclude with a generic overview of the thesis with chapter summaries.

1.1 Principles of Biosensor Function

In the past few decades, the scientific community has witnessed the invention of many key enabling technological advances that provide the tools needed to develop new techniques to monitor biomolecular interaction events. All molecular-based biosensors rely on specific recognition events to detect their target analytes, often resulting in the

binding (antibodies, nucleic acids, peptides, etc) or biocatalytic (enzymes, microorganisms, tissue materials, etc.) event between sensing probe and target molecules. The reaction can take place either in solution, or within a 'recognition layer' on a solid surface with immobilized probes. The interaction then triggers the sensor to convert, or transduce, a biochemical event to a physical signal that is amenable to data acquisition and processing, for example, electronic output. Biosensor research is a multidisciplinary effort, exploiting many of the emerging technologies in biology, chemistry, physical sciences and engineering, and integrating many traditional assay techniques, as illustrated in Figure 1–1.

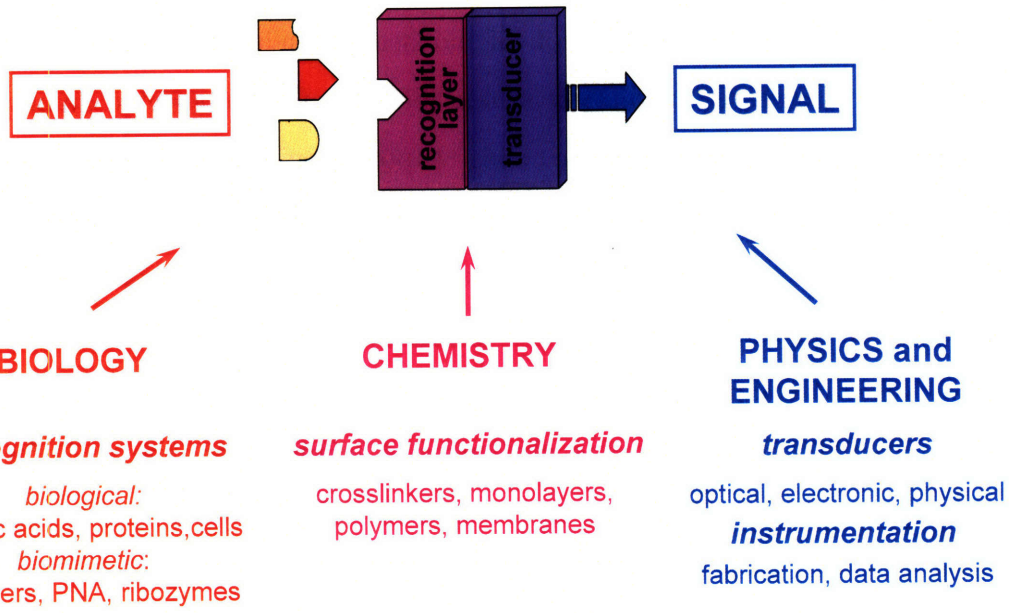

Figure1–1: Paradigm of Biosensor Research and Development. Biomolecular Interaction that takes place on a sensing surface is converted (transduced) into a physical quantity. Developing each component of a complete biosensing platform requires expertise from different branches of science.

The basic architecture of biosensor can be applied to a large variety of applications including environment monitoring, clinical care, as well as basic molecular biology research. For example, screen-printed glucose sensors for measuring the glucose levels of diabetics have revolutionized the treatment of diabetes; a wide variety of biosensors based on immobilized microorganisms to detect of environmental organic pollutants

capable of demanding continuous real-time monitoring have also been ccommercialized. [1] In contrast, the tools of molecular biology, in particular for nucleic acids quantification, have traditionally lacked throughput and resolution until the advent of revolutionary biochemical and engineering techniques such as PCR [2] and microarray [3]. To date, several major categories of biomolecular sensing techniques have achieved various levels of speed, and accuracy, and sensitivity of quantitation. Methods representing the state of the art in each attribute as well as potential tradeoffs will be discussed in the following sections.

1.2 Optical Nucleic Acid Sensing Technology

Few other engineering advances have made more contribution to biological research than fluorescence detection technology. For example, microarrays technology, which has revolutionized the field of genomics by allowing gene expression on a whole genome scale, most frequently uses fluorescence to analyze the molecular binding event. [4] The samples are pre-labeled with fluorescent dyes, and after incubating them with the microarray in chambers with careful assay conditions, the slides are subsequently washed to remove non-specific targets. The brightness of each microarray spot is read optically to determine the extent of interaction with sample. The detection is often performed by a confocal laser scanner, or more recently with CCD camera, which allows thousands of spots to be read in minutes. [3]

The use of fluorescence readout for signal transduction has many decided advantages. First, the fluorescent labeling of molecules is a general technique that enables the detection of molecules regardless of their intrinsic properties as long as they can be labeled. Optical biosensors based on fluorescence are also extraordinarily sensitive, with detection limits approaching $\sim 10^7$ molecules/cm^2. [5] Fluorescence also permits multiplexing; for example, Cy3 and Cy5 dyes can be used to label two different nucleic acids samples which are hybridized to the same array, and the ratio of fluorescent intensities is acquired for differential analysis of gene expression. Unlike radioactive labeling, which is subject to health and environmental concerns, fluorescence is safe.

Another key factor which has contributed to the rapid popularization of fluorescence-based biosensing is the availability of commercial instruments which borrow readily from the concepts developed in microscopy. The most basic optical configuration employed is an epifluorescence setup, where a beamsplitter dichroic mirror that directs the wavelength of interest i.e. emission of fluorophore to the optical detector only, minimizing background signal from the excitation source. In recent years, confocal microscopy, originally developed for optical sectioning to produce a high-resolution 3D-image of a specimen by focusing the excitation and emission lights through pinholes [6], has become increasingly popular for low-noise microarray laser scanning. Likewise, total internal reflection fluorescence, which uses evanescent waves generated by laser above a certain critical angle on the backside of a microscope slide, was an fluorophore excitation technique developed before the invention of microarray but has now been used extensively for its readout. [7] The most popular optical detectors are photomultiplier tubes (PMT) and charge-coupled device (CCD) sensor. The two sensing methods each has their own advantages and disadvantages, where the quantum efficiency of the CCD is generally higher, while the PMT can be configured for a higher gain factor and larger dynamic range. [8] Since PMT is a more mature technology, it is more widely used, but this lead is challenged by the rapid pace of advance in CCD-based systems.

The field of fluorscence biosensing technology has also benefited greatly from a wide repertoire of labeling schemes and dyes available. Direct labeling of a biomolecule involves the introduction of a covalently linked fluorophore into the nucleic acid sequence or the amino acid sequence of a protein or antibody. The choice of dye is dependent on the optical setup and type of experiments performed, and important parameters include excitation spectrum, emission spectrum, quantum yield (Q), and photodegradation. [8] The fluorescence lifetime is of particular interest recently as dyes with long life-time can be used for time-resolved imaging, where the recording of fluorescence is done after a delay following excitation which disables interference from stray excitation light and background of biological samples. [9] Organic fluorescent dyes have been the most widely used class of labels for microarray analysis due to their

ready functionalization, solubility, and biocompatibility in aqueous buffer solutions. However, many organic dyes show quenching in bioconjugates, relatively high rate of photobleaching, and sensitivity to the buffer properties, prompting the development of alternative technologies such as fluorescent nanoparticles. Polymeric nanoparticles such as polystyrene nanobeads doped with lipophilic dyes [10], encapsulated silica particles with fluorescent complexes [11], and more recently quantum dots [12] have been used as alternative fluorescent labels. The semiconducting quantum dots are of particular interest because they can be excited at virtually any wavelength shorter than 550nm, while the emission spectrum can be tuned by the choice of the material and the size of nanocrystals. Furthermore, they are insensitive to photobleaching, have a narrow emission spectrum, and silane or thiol surface chemistry can be applied to allow solubility and conjugation to a variety of biomolecules.

Despite the advantages of fluorescence analysis format, it has many intrinsic disadvantages. For example, while extremely sensitive, the use of a label may possibly interefere with the binding event, particularly when the native structure of the analyte molecule has not yet been fully established. For example, it has been shown that fluorescent moieties that differ widely in structure produce hybridization and detection artifacts that depend on the sequence of nucleic acids and the position of dye on the labeled sequence, thereby producing false positives in differential microarray experiments, and unfortunately the basis of this is poorly understood. [3, 13] Furthermore, the process of labeling is not only time-consuming and expensive, but can also cause erroneous results by introducing undesirable variations into the samples. Also, the low detection limit is difficult to achieve in practice because the signal will always be obscured by the background autofluorescence as well as the scattered light from the microarray slide. Because detection can only be performed after the sample is rinsed to eliminate signals from unbound molecules, labeling also prevents the real-time monitoring of binding kinetics.

1.3 Measuring beyond the Physical Limits of Biosensors through Signal Amplification

When physical signals such as fluorescence are near or below the detection limit of a biosensor, it is often desirable to amplify the signal by chemical or biological means. This enhancement in signal will then shift the detection limit into the analytically useful range.

The most established and commercially successful scheme for biochemical amplification of protein signal is enzyme-linked immunosorbent assays (ELISA). The ELISA format is based on two antibodies, one specific to the antigen of interest (capture antibody), and a secondary antibody with immobilized enzyme which is responsible for signal amplification following the capture antibody-antigen complex. [14] Two common ELISA enzymes: alkaline phosphatase (AP), which removes a phosphate group from its substrate, and horseradish peroxidase (HRP), which catalyzes an oxidation of its substrate. Substrates are chosen so following the reaction there is a detectable changes in the optical or chemical properties of the sample. A study has successfully adapted the technique to microarray format, employing an Alexa546-labeled tyramide coupled to a biotin HRP streptavidin system as a reporter for allergen-specific IgE's, enabling the detection of less than 1fg of allergen-bound IgE in human serum, lowering the detection limit by several orders of magnitude without amplification. [15] While ELISA does extend the detection limit of protein detection, the additional reagents require extensive optimizations and do not necessarily increase the dynamic range overall, as nonlinearity could be observed at high concentrations of analyte. [16]

In addition to use of biochemically active labels for signal amplification, approaches that exploit the reactivity of nanoparticles to achieve the same effect have also been developed. Similar to an ELISA assay, the capturing probe can be immobilized on a substrate in an array format, and a secondary nanoparticle-functionalized probe recognizing the complex generates the recognition signal. For example, Taton et al. functionalized a secondary DNA capture sequence with gold nanoparticles, which after capture and stringent rinsing to remove unbound particles, can catalyt-

ically promote the reduction of silver ions. [17] The product of this reaction can simply be read by a grayscale flatbed scanner, and a detection limit 100 times greater than that of conventional fluorescence-based assays was achieved. By encoding gold nanoparticles functionalized with particular peptides or proteins each with a unique raman dye, multiplexed study protein-small molecule and protein-protein interactions using surface-enhanced Raman scattering spectroscopy is also possible in a microarray format. [18] Another improvement in sensitivity based on nanoparticle secondary labeling has been reported in which the gold nanoparticles are replaced with polystyrene microspheres each impregnated with 10^{11} ferrocenecarboxaldehyde molecules, which is liberated for electrochemical quantification following hybridization. [19] This method has demonstrated a detection limit of 5×10^{-21} moles, the record for hybridization-based nucleic acid assay thus far. While being very sensitive, most nanoparticle-based protocols involve many complicated development steps, and the reliability of the assembled complex on surface is questionable. [5]

While a plethora of label-free and label-based amplification methods have been developed for the sequence-specific hybridization-based detection of nucleic acids, the polymerase chain reaction (PCR) for nucleic acid amplification still represents the ultimate in detection limit [2]. Using a thermophilic DNA duplication enzyme, the technique involves thermally cycling a mixture of DNA templates, two oligonucleotide primers that mark the beginning and end of a sequence of interest, and nucleotide triphosphate monomers through three temperature regimes to chemically enrich the concentration of a specific double-stranded DNA sequence exponentially in a complex mixture of DNA. The reaction theoretically doubles the concentration after each round until saturation occurs. Traditionally, the readout of the reaction is done by gel electophoresis that separates the DNA by length [20], but monitoring of reaction in real-time has been made possible by fluorescent intercalators [21] and sequence-specific reporter probes [22,23,24]. Together with the commercialization of thermocyclers capable of fluorescent measurements, real-time PCR enables an unprecedented range of nucleic acid measurements of up to 8 orders of magnitude, high sensitivity of fewer than 5 copies, and high precision of less than 2% standard deviation. [25]

Extensive studies have shown that commercial PCR-based kits for quantification of HIV, Mycobacterium tuberculosis, and Chlamydia trachomatis have clinical accuracies superior to more recent nucleic acid signal amplification techniques bDNA and NASAB. [26,27]

PCR does suffer from several key drawbacks such as complexity of protocol development, especially if sequence-specific real-time probes are used [28], sensitivity to contamination, major challenges with respect to multiplexing.

1.4 Promises of Microfabricated Total Analytical Systems and Challenges of Integration

The extraordinary capabilities of polymerase chain reaction (PCR) have made it one of the most widely used techniques for analyzing nucleic acids [29]. As a result, considerable effort has been directed towards developing miniaturized and integrated systems for PCR. Examples include the inclusion of capillary gel electrophoresis, microvalves and pumps, hybridization chambers, and sample purification stages [30,31, 32,33]. Not only is integration advantageous in terms of efficient sample handling and automation, scaling down PCR itself leads to many improvements including increased thermal response rate of up to ten folder faster than commercial systems, more uniform temperature distribution, reduced reagent consumption, and in a number of instances, more reproducible performance in single molecule PCR. [34,35,36] Given these merits, several commercial prototypes have been developed that perform favorably in real-world settings. [37,38,39].

While there have been extensive advances in miniaturized PCR systems, progress on integrated microfabricated readout mechanisms have been rather limited, and most systems rely on off-chip optical detection modules to measure the final product. [40] Existing optical detection platforms typically include CCD cameras, photodiodes, and photomultiplier tubes. [37,38,41,42,43] While such hardware has adequate sensitivity for detecting PCR product in sample volumes significantly lower than that of bench-

top systems, most are difficult to miniaturize and integrate into a compact analytical system. Both CCD and photomultiplier tubes are popular fluorescent imaging devices for microchip DNA readout, but generally occupy a large footprint. While these devices can be scaled down to offer portability for PCR microdevices, the extent to which they may be further miniaturized maybe be limited. For example, some most recent portable systems that incorporating external LEDs and photodetectors weigh between 1kg and 4kg each. [44,45,46] To address these limitations, several groups have successfully embedded photodetectors within an integrated PCR platforms [31,47,48] However, these devices still rely on external excitation sources.

Optical detection of nucleic acids in miniaturized systems is also challenging because the signal originates from dye molecules in solution, and thus the strength of the signal scales with sample volume. Therefore, there is a direct conflict between the goals of obtaining a strong optical signal and reducing reagent consumption in the microfluidic system. Furthermore, optical readout requires that PCR product markers such as Sybr Green and Taqman probes be added to the reagents, and this can induce inhibitory effects on PCR or require extensive effort to optimize. [49, 28, 50]

Another challenge faced by all designs employing microfluidics is the increased likelihood of failed reaction due to channel surface-induced reaction inhibition. Microfluidics systems possess greater surface-to-volume ratio than typical PCR reaction tubes, usually 20-times higher or more. [51] Since PCR is a multi-component reaction, the possibility of at least one of these components binding to surface of the channel is greatly increased. Of these interactions, particularly adverse to the performance of the reaction is the denaturation of Taq polymerase due to sidewall adsorption as well as the irreversible binding of the amplification target. Thus, amplification yield is usually weaker than that in a conventional PCR tube system. [52] Another issue with the scaling down of the volume is that for very low sample template concentrations, statistical effects may come into play. Consider an extreme scenario: While filling a microPCR reservoir from a tube containing only one template, there is no guarantee that the simple template will end up in the microfluidic PCR system or be flushed into waste. In practical scenarios, it is quite likely the average number of templates

in a microfabricated PCR reservoir may be below 1, which implies physically the well may contain a few or none of the templates one intends to amplify. This effect has been investigated by Matsubara et al., who demonstrated that when arrays of microPCR chambers contained only a few copies of genes per chamber, some chambers would produce positive amplification results while some would not. [53] At the same time, the author showed that the percentage of microchannels that produce positive amplification correlates with starting template concentrations for very low starting template numbers, and this feature has allowed end-point based template concentration quantitation which has not been realized on bulk-PCR systems.

1.5 Studying Molecules in their Native Form through Label-Free Sensing

To address the shortcomings associated with fluorescent biosensor technology, significant effort has been devoted to either develop labels that can be detected by other means or techniques for studying molecular interactions that obviate the need for labels all together. The most established sensing method in the field exploits surface plasmon resonance (SPR), which detects changes in the refractive index due to binding in the immediate vicinity of the surface layer where probes are immobilized, has generated over 3000 scientific publications. [54] The label-free SPR sensor is completely general, allowing a wide range of disciplines to study real-time molecular interaction kinetics for ligand fishing, apoptosis, bacteriology, epitope mapping, cell adhesion, and nucleotide-protein bindings.

Acoustic biosensors are another popular format of label-free sensing and are most often based on quartz crystal resonators. By monitoring the change in resonant frequency and resistance that occurs upon adsorption of a ligand to the surface, quartz crystal microbalance (QCM) resonators can also be applied to a wide range of biological and chemical entities with a molecular weight range from less than 200 Daltons to entire cells. [55] In addition to monitoring binding and dissociation kinetics,

a quartz crystal can also be used in an oscillation mode where an electric field of varying strength is applied to the crystal, causing the crystal to vibrate at a high frequency with enough acceleration to break bonds between a receptor and a ligand. The QCM can then simultaneously detect the acoustic noise produced when the interactions were broken. [56] While this method is very sensitive with a resolution of $3 \times 10^{-3}\,\mathrm{ng\,cm^{-2}}$, it is not amenable for multiplexing and requires highly controlled temperature chamber to maintain stability.

1.5.1 Microfabricated Label-free Biosensors

Microfabricated bio-analytical systems offer potential for function integrations and scalability comparable to microarrays. Using fabrication technology developed for microelectronics, massive arrays of micrometer-sized sensors can be fabricated at very low cost and in small footprint enabling point-of-care diagnostics. Furthermore, since the size of the sensor is scaled significantly, the sample requirement can also be reduced significantly with microfluidic integrations, a feature that saves reagent consumption and cost. Given the promise of scaling, there has been a great number of attempts to microfabricate novel biosensors to exploit the potential benefits of scaling. [57] A noteworthy example that realizes such potential for label-free biosensing is a mass-based suspended microchannel resonator technology [58], where a mass change caused by the binding of molecules inside a hollow-cantilever results a shift in the resonant frequency of the cantilever. Unlike most microfabricated cantilever-based technology, the cantilever is not immersed in fluid and can instead be packaged in vacuum, is therefore subject to far less damping force which results in superior mass-dependent frequency resolution. Based on preliminary measurements, calculations show that changes in surface mass loading on the order of $10^{-19}\,\mathrm{g\,\mu m^{-2}}$ can be detected in an optimized system. In addition, the fabrication process of the device makes it amenable for array implementation, and the possibility of integrating electronic frequency readout capability to individual cantilevers [59] eliminates the need for external optics, making the system ideal for integration into portable systems for point-of-care measurements.

For more specialized applications such as the detection of nucleic acids for genomic and functional genomic assays, techniques that directly make use of the intrinsic properties of the particular biomolecules can be used for enhanced signal to noise ratio. Electrochemical biosensors are particularly useful for miniaturized nucleic acid measurements because DNA bases are electrochemically active and the resulting reactions give an electrical signal via simple electrodes directly, eliminating the need for expensive and bulky signal transduction equipment. Therefore, the overall system can be a lot more compact than commercial instruments relying on external optical excitation sources and/or photodetectors. An archetypical example of electrochemical DNA detection is detection using direct quinine oxidation at carbon paste electrodes with inosine-modified probes. [60] Unfortunately, this method requires high potentials, which induces high background currents, and thus catalysts such as polypyridyl complexes of Ru(II) have been developed to facilitate this reaction. [61] Nevertheless, this detection format still destroys the sample and the use of catalyst restricts the choice of substrate for probe immobilization. Another approach takes advantage of the electronic structure of double-helical nucleic acid, using intercalated redox probe molecules to report perturbations in base stacking. [62] In this assay, thiolated duplexes are self-assembled into densely packed film on gold surfaces, then treated with redox-active intercalator. Upon intercalation, the reporter molecule is electrochemically reduced by DNA-mediated charge transport. The reaction occurs only if the individual duplxes in the film contain well-stacked base pairs, and a partially hybridized single-base mismatch is sufficient to shut off the reaction completely, making the assay well-suited for mutational analysis.

The possibility of a label-free electrical detection of DNA hybridization by its intrinsic molecular charge using semiconductor field-effect sensors offers a scalable approach for a fast, simple, and direct analysis of nucleic acids samples. The inherent miniaturization of such devices and their compatibility with standard silicon processing techniques make them very attractive for DNA diagnostics. This class of technique typically employs capacitive electrolyte-insulator-semiconductor (EIS) and field-effect transistor (FET) structures [63, 64, 65, 66, 67, 68, 69, 70], and when

complementary DNA or RNA hybridizes to the single-stranded probe immobilized on dielectric gate of the device, the resulting change in surface charge density shifts the distribution of mobile charge carrier in silicon [71], which can be measured as a change in the capacitance or conductivity of the electronic device. While historically there has been doubts that charge-screening effect of ions in solution would neutralize biomolecules rendering the field-effect sensors totally insensitive [72], at the turn of the 21st century there has been many reports on successful detection of DNA hybridization down to femtomolar concentration. [70] However, the resolution is still insufficient to detect potent viral sequence such as HIV RNA which can exist in zeptomolar concentrations. [73] While microelectronic biosensors are still inferior to optical detection of labeled DNA in sensitivity, the former offers scalability, low cost, small form factor, and ability to study molecular interactions accurately in their native forms, making them suitable for both low and high-throughput applications.

1.5.2 Comparison of Microscale and Nanoscale Field-Effect Sensors

Besides differences in modes of operation (EIS vs. FET), field-effect sensors can also be categorized based on dimensions into microscale and nanoscale field-effect sensors. Traditionally, silicon-field-effect sensors were fabricated using tools designed for semiconductor processing ([63]- [69]); however, the advent of 2-D nanostructures such as nanotubes and nanowires that can undero analogous changes in electrical properties due to binding of charged molecules has also lead to the development of nanoscale biosensors [70, 74, 75]. Based on electrostatics considerations, it is know that two dimensional cylindrical nanostructures are more sensitive to adsorbed charges [76]. Experimentally, the lowest detection limits for field-effect sensors have been realized on 2D-nanostructure, for example, such as femtomolar DNA and 1 ng/L protein resolution for nanowires. [70, 77]

2-D nanostructure-based field-effect sensors also enjoy more sutble advantages over conventional 1-D microfabricated sensors by considering mass transport efects.

Specifically, not only is the detection limit of a biosensor dependent on the intrinsic physical properties of the sensor, but also on the particular geometry of the biosensor which determines how many molecules can bind to the sensor to yield a detectable signal within a reasonable amount of time (settling time). Nair et al. derived a quantitative expression that describes the tradeoff between settling time and detection limit in a diffusion limited regime [76]:

$$\rho_0 t_s^{M_D} \sim k_D \tag{1.1}$$

where t_s is settling time, ρ_0 is the detection limit, M_D and k_D are sensor-dimensionality dependent constants, where microfabricated field-effect devices with a planar sensing surface are considered "1-D" and nanowire or nanotube rod-shaped sensors are considered "2-D". The former has an M_D of .5, and the latter has an M_D of 1; this means that to lower the detection limit by the same amount for both platforms, the penalty in the increase of settling time will be comparatively less for 2-D nano-sensors compared to 1-D sensors, which are typically microfabricated. Therefore, the kinetics argument could explain in part why a nanoscale sensor could potentially achieve better resolution. However, when one introduces active transport by flowing analyte through the sensor to minimize sample depletion or diffusion limited transport, the microfabricated device such as an EIS sensor with a disk-like surface in the middle of the channel benefits far more than 2-D nanoscale rod-like sensors in binding time-reduction [78]. The difference stems from the mechanism through which flow increases total flux; the fluid moves most rapidly in the middle of a channel for laminar flow, and therefore analyte is replenished most rapidly there. Thus a disk-like sensor with most sensing area along the middle of the channel benefits the most from active analyte transport, whereas a rod-like nanoscale sensor that already does not deplete significantly the analyte in solution will not experience much enhancement in binding time reduction. For example, calculations show that a disc-like sensor with 100μm radius can experience up to 100-times reduction in binding time whereas a 10 nm nanowire sensor only improves 3-fold at 1000μL/min volumetric flowrate compared

to zero flowrate. Thus when sample volume is relatively large compared to channel volume, and active flow is used to expedite sample analysis, the advantage enjoyed by nanosensors will become less clear. Despite the various possible performance advantages of 2-D nanoscale biosensors, a factor that has severely limited the parallelization and mass-production is the lack of high-throughput fabrication method. For example, nanowire and nanotube sensors are typically grown off the device, then deposited on a substrate. While recently there has been effort to orient and position the nanostructures at defined locations using techniques such as microfluidic alignment [79], the technique can only guarantee an 'average case' positioning accuracy for the nanostructures, but the exact positions of individual nanostructures can still be uncertain. Thus electrical contacts are frequently customized for each device, requiring e-beam lithography for patterning electrodes. The limitations in scalability requirement for device fabrication is a major challenge that needs to be overcome if the performance advantages is to be realized in a real-world setting.

1.6 Thesis Outline

A goal of the thesis is to develop a label-free nucleic acid detector that can measure at comparable resolution as an optical system without the drawbacks associated with optics and fluorescent dyes. The strategy is to incorporate biochemical amplification through PCR as a sample pre-processing stage to extend the detection limit and dynamic range of the sensing platform. In addition, to facilitate rapid adaptation to new applications, another goal is to simplify and generalize the overall protocol as much as possible for the specific detection of different sequences.

This thesis study reports a microelectronic nucleic acid sensor with integrated PCR amplification functionality. In particular, the thesis explores a sensing method which does not rely on hybridization to detect product in an unprocessed PCR mixture, thus eliminating the need to develop immobilized capture probe sequences for each application. In addition, the sensing technique based on layer-by-layer assembly of polyelectrolytes permits multiple rounds of measurements required for real-time

PCR applications. By combining amplification and detection on the same device, the device is designed to produce analog output that can readily converted to a simple digital true/false readout for the presence or absence of a target sequence.

The thesis also explores the feasibility of using the same sensing principles for detection of clinically relevant targets. The label-free electronic sensing of heparin using polyelectrolyte multilayer assembly will be studied and compared to established clinical tests.

In Chapter 2, quantitative circuit models for EIS systems and polyelectrolyte multilayers will be presented. Using empirically derived parameters for calculations, the model will be used to intepret the qualitative features of electronic measurements of polyelectrolyte multilayer assembly. Chapter 3 discusses the design and fabrication of the device, and Chapter 4 examines the tests carried on the device to characterize its basic basic electronic, thermal, and microfluidic properties. Chapter 5 describes a label-free electronic sensing method that can quantify PCR at various stages of the reaction, and Chapter 6 illustrates protocols to improve yield of microfabricated PCR systems and to perform end-point detections of PCR product on chip. Chapter 7 studies detection of heparin and heparin-based drugs in both buffer and serum using a differential electronic sensing scheme. The conclusions presented in Chapter 8 will review the specific contributions of this thesis and propose directions for future work.

Chapter 2

Theory

This chapter presents a theoretical framework for electronic detection of polyelectrolytes such as DNA. First, a qualitative description of field-effect sensing of charge molecules immobilized on sensor surface will be presented. Overviews of the physical and chemical properties of the sensing system and polyelectrolyte multilayer will be given independently, after which an unifying circuit model that describes the electrical characteristics of the platform will be introduced. Based on the model, the scaling of key parameters and their impact on both sensor signal and PCR protocol design will be discussed.

2.1 Equivalent Circuit Model for EIS Structure

Molecular adsorption at the solid-liquid interface plays an important role in a wide spectrum of applications including biomedical implants, drug carrier systems, and biosensors. Making use of the physical and chemical properties of biomolecules, surface-based field-effect devices such as electrolyte-insulator-semiconductor (EIS) and field-effect-transistor (FET) sensors transduce the adsorption of intrinsically charged molecules to the sensor surface to changes in capacitance and conductance of the device, respectively. The field effect sensor used in this study is an EIS device, which is conceptually similar to a MOS capacitor with gate metal replaced by electrolyte. The device consists of two primary components - a metal signal electrode

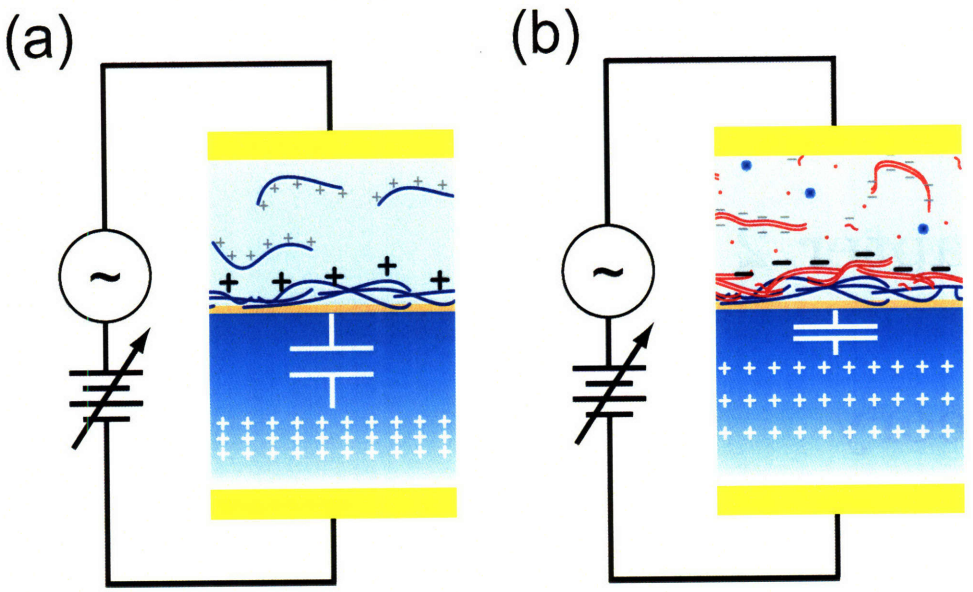

Figure 2–1: Conceptual Illustration of EIS structure, showing the effects due to adsorption of (a) positively charged and (b) negatively charged species on sensor surface. The mobile charge carriers are repelled or attracted to the sensor surface, and the measured capacitance value is inversely proportional to the size of the depleted region devoid of charges.

and lightly doped silicon region covered by a dielectric gate (Figure 2–1). Variation in the insulator-electrolyte surface potential, arising from binding of charged molecules to the sensor surface, changes the distribution of mobile charge carriers in the doped silicon, which in turn affects the depth of the depletion region in the silicon beneath the sensor surface. This effect is quantified by monitoring the capacitance of the space-charge region. The depletion region capacitance is indirectly measured by applying a small AC voltage on the metal signal electrode, and the signal is propagated to the sensor through solution. The resulting AC current through the EIS structure is amplified and recorded. In practice, it is difficult to directly calibrate the measured current value with respect to surface potential by applying a well-defined potential to the sensor surface. However, since the silicon depletion capacitance is a function of the potential difference between the electrolyte and sensor body, as will be derive later, the potential response of the sensor can be calibrated easily by applying a change in sensor substrate bias and observing the resulting change in the measured

current.

To quantify and predict how the adsorption of charged molecules on field-effect sensor surface, as well as changes in experimental conditions such as buffer composition will affect the electrical characteristics of an EIS system, the components of the EIS structure through which an AC current traverses will each be modeled as an impedance element as shown in Figure 2–2:

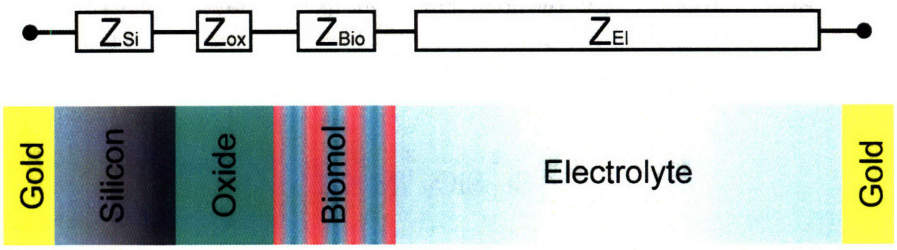

Figure2–2: Equivalent Circuit Model of an EIS Structure.

The current travels through an excitation metal electrode, electrolyte, a layer of biomolecules adsorbed on sensor surface, the sensor gate dielectric, bulk silicon with a surface-potential sensitive depleted region, and finally a metal line connected to silicon. Thus, the current due to a small signal AC excitation voltage can be expressed as:

$$I_{\mathrm{AC}} = \frac{V_{\mathrm{AC}}}{Z_{\mathrm{Si}} + Z_{\mathrm{ox}} + Z_{\mathrm{ox}} + Z_{\mathrm{El}}} \tag{2.1}$$

The values of the impedance elements depends on the 'DC' conditions of an experimental system such as adsorbed charged molecule density and electrolyte composition. In the following sections, quantitative expressions for the components will be derived. The electrostatics of each circuit element will first be considered individually, then a unifying circuit model will provided.

2.2 MOS Electrostatics

First, consider an EIS structure with no adsorbed biomolecule but a finite charge density at the dielectric-electrolyte interface. The following interfaces are present in

an EIS structure:

$$\mathrm{Au}' \overset{1}{|} \mathrm{Si} \overset{2}{|} \mathrm{SiO_2} \overset{3}{|} \text{electrolyte} \overset{4}{|} \mathrm{M} \overset{5}{|} \mathrm{Au}'' \tag{2.2}$$

Where M is the metal signal electrode, which consists of gold in Figure 2–2, and Au is the gold wire. While it is possible to analyze the structure directly, one sees that the MOS capacitor, for which an extensive knowledge base is developed in the electronics industry, can be conceptually thought as a special case of the EIS device with electrolyte removed:

$$\mathrm{Al}' \overset{1}{|} \mathrm{Si} \overset{2}{|} \mathrm{SiO_2} \overset{3}{|} \mathrm{M} \overset{4}{|} \mathrm{Al}'' \tag{2.3}$$

The electrostatics of the simplified case - MOS capacitor - will be studied first, and the results will be extended to the general EIS structure. Define $\mathrm{V_a}$ as the voltage applied to the metal interconnects Al' and Al''. Due to equilibrium between interfaces 1 and 4, it follows:

$$\mathrm{V_a} = \frac{1}{q}\left(\Phi_{\mathrm{M}} - \Phi_{\mathrm{Si}}\right) + \left(\delta\chi_{\mathrm{ox}}^{\mathrm{M}} - \delta\chi_{\mathrm{M}}^{\mathrm{ox}}\right) + \left(\delta\chi_{\mathrm{Si}}^{\mathrm{ox}} - \delta\chi_{\mathrm{Si}}^{\mathrm{ox}}\right) - \frac{\mathrm{Q_{ox}}}{\mathrm{C_{ox}}} + \psi_{\mathrm{Si}} \tag{2.4}$$

where Φ_{M} and Φ_{Si} are metal and silicon work functions, $\delta\chi_{\mathrm{ox}}^{\mathrm{M}} - \delta\chi_{\mathrm{M}}^{\mathrm{ox}}$ and $\delta\chi_{\mathrm{Si}}^{\mathrm{ox}} - \delta\chi_{\mathrm{Si}}^{\mathrm{ox}}$ are the difference of inner potential across the metal gate/oxide interface and across oxide/silicon interface, $\mathrm{Q_{ox}}$ is the trapped charge at the $\mathrm{Si/SiO_2}$ interace, and ψ_{Si} is the potential drop in Si. $\mathrm{V_{FB}}$ is defined the applied voltage when $\psi_{\mathrm{Si}} = 0$. In the simplified scenario, the trapped charges and inner potential differences across interface are not present, then $\mathrm{V_{FB}}$ simply reduces to $\Phi^{\mathrm{M}} - \Phi^{\mathrm{Si}}$. At thermal equilibrium, the electrical potential of silicon Φ^{Si} can be computed as a function of electron and hole concentration:

$$\Phi_{\mathrm{Si}}(x) = \frac{kT}{q}\ln\left(\frac{n_o(x)}{n_i}\right) = -\frac{kT}{q}\ln\left(\frac{p_o(x)}{n_i}\right) \tag{2.5}$$

where k is Boltzmann constant, T is temperature, q is electron charge, $n_o(x)$ and $p_o(x)$ are electron and hole concentrations at depth x from silicon/insulator interface,

and n_i is the electron concentration in undoped silicon. Extrinsic dopants such as phosphorus and boron are used to create an excess of electrons or holes in silicon, and in this case n_o or p_o are simply N_d or N_a, the concentrations of donor or acceptor dopants, respectively.

To ensure a continuous potential across the different physical elements of the MOS capacitor, the Fermi levels are aligned at thermal equilibrium and an electric field is created in silicon. This creates a potential difference in silicon (hence the term ψ_{Si}), which makes extrinsic dopant concentrations alone insufficient in describing the potential and charge density of the doped silicon at position x. A combination of Boltzmann statistics and Poisson equations can be used to relate charge density and potential in silicon:

$$\frac{d^2\Phi_{\mathrm{Si}}}{dx^2} = -\frac{qN_A}{\varepsilon_{\mathrm{Si}}}\left(\left(e^{-\frac{q\Phi_{\mathrm{Si}}}{kT}}-1\right)-\frac{n_i^2}{N_A^2}\left(e^{\frac{q\Phi_{\mathrm{Si}}}{kT}}-1\right)\right) \tag{2.6}$$

A formula that computes the total charge density $\mathrm{Q_{si}}$ can be derived using the potential value at $\mathrm{Si/SiO_2}$ interface, $\Phi_{\mathrm{Si/SiO_2}}$.

$$F\left(\Phi_{\mathrm{Si}}\right) = \frac{\Phi_{\mathrm{Si}}}{|\Phi_{\mathrm{Si}}|}\sqrt{\left(e^{-\frac{q\Phi_{\mathrm{Si}}}{kT}}+\frac{q\Phi_{\mathrm{Si}}}{kT}-1\right)-\frac{n_i^2}{N_A^2}\left(e^{\frac{q\Phi_{\mathrm{Si}}}{kT}}-\frac{q\Phi_{\mathrm{Si}}}{kT}-1\right)} \tag{2.7}$$

$$\mathrm{Q_{Si}} = -\sqrt{2\varepsilon_{\mathrm{Si}}kTN_A}F\left(\Phi_{\mathrm{Si/SiO_2}}\right) \tag{2.8}$$

The small-signal capacitance of silicon in an EIS structure is the change in space charge region due to a small change in silicon surface potential:

$$C_{\mathrm{Si}} = \frac{d\mathrm{Q_{Si}}}{d\Phi_{\mathrm{Si/SiO_2}}} = -\sqrt{2\varepsilon_{\mathrm{Si}}kTN_A}\frac{dF\left(\Phi_{\mathrm{Si/SiO_2}}\right)}{d\Phi_{\mathrm{Si/SiO_2}}} \tag{2.9}$$

Several assumptions can be made to simplify the equation. In the case of a MOS structure with electron acceptors (p-dopant), when the applied voltage is higher $\mathrm{V_{FB}}$, the positively charged extrinsic carriers near the $\mathrm{Si/SiO_2}$ surface are expelled into bulk silicon while the embedded negatively charged atoms remain fixed to their lattice sites. Also referred to as the depletion approximation, this allows the silicon capacitance to

be expressed simply as:

$$C_{\mathrm{Si}} = \frac{\varepsilon_{\mathrm{Si}}}{x_{\mathrm{dep}}} \tag{2.10}$$

where x_{dep} is the width of depleted region in silicon. In this region, the potential-independent charge density is equivalent to dopant ion concentration multiplied by their charge polarity. The size of the depleted region is however dependent on the applied voltage:

$$x_{\mathrm{dep}} = \frac{\varepsilon_{\mathrm{Si}}}{C_{\mathrm{ox}}} \left(\sqrt{1 + \frac{2C_{\mathrm{ox}}^2 \left(\mathrm{V_a} - \mathrm{V_{FB}}\right)}{\varepsilon_{\mathrm{Si}} q N_a}} - 1 \right) \tag{2.11}$$

As will be shown later, this capacitance will dominate the signal in an EIS setup. To optimize the sensor response, it is desirable to maximize the change in depletion region width with respect to change in applied voltage, $\frac{dx_{\mathrm{dep}}}{d\mathrm{V_a}}$:

$$\left| \frac{dx_{\mathrm{dep}}}{d\mathrm{V_a}} \right| = \frac{C_{\mathrm{ox}}}{q N_a \sqrt{1 + \frac{2C_{\mathrm{ox}}^2 (\mathrm{V_a} - \mathrm{V_{FB}})}{\varepsilon_{\mathrm{Si}} q N_a}}} \tag{2.12}$$

the expression reduces to $\frac{C_{\mathrm{ox}}}{q N_a}$ when $\frac{2C_{\mathrm{ox}}^2 (\mathrm{V_a} - \mathrm{V_{FB}})}{\varepsilon_{\mathrm{Si}} q N_a} \ll 1$. This relation is especially instructive in guiding device scaling to maximize capacitive response to changes in applied potential: one should maximize gate dielectric capacitance C_{ox} by minimizing its thickness and/or minimizing the dopant concentration. In the case of ultra-thin gate dielectrics, however, significant deviations from classical MOS model is observed since quantum mechanical effects start to become significant and Fermi-Dirac statistics must be applied to describe the operation of the device. Furthermore, issues in stability and carrier lifetime becomes more pronounced. [80] A Detailed discussion and quantitative modeling of MOS scaling is provided in [81].

2.3 EIS Electrostatics

Having analyzed the electrostatics of a MOS capacitor, the basic concepts can be extended to EIS modeling. First, consider the effect of replacing the gate metal

with electrolyte and introducing a sheet charge σ to the oxide/electrolyte interface. The surface charge will induce a potential on the surface, and let ζ represent the electrostatic potential as a function of distance y from the surface in electrolyte. Similar to the potential-charge relation in silicon, Poisson-Boltzmann equations can be written for distribution of ions in solution in thermal equilibrium:

$$c^{\pm}(y) = Ie^{\mp\frac{ze\zeta}{kT}} \tag{2.13}$$

$$\frac{d^2\zeta}{dy^2} = \frac{-\rho(x)}{\varepsilon_{\mathrm{w}}} = \frac{ze\left(c^{+}(x) - c^{-}(x)\right)}{\varepsilon_{\mathrm{w}}} = \left(\frac{2zeI}{\varepsilon_{\mathrm{w}}}\right)\sinh\left(\frac{ze\zeta}{kT}\right) \tag{2.14}$$

where z is the valence of ions, I is the ionic strength of bulk solution, e is the elementary charge, $c^{\pm}$ are the positive and negative ionic concentrations, and ε_{w} is permittivity of water. In the absence of an applied voltage on the metal electrode, at a distance far away from the oxide surface there is a balance of ionic charges, and thus $\zeta(\infty) \equiv 0$. Solving the equation yields:

$$\zeta = \left(\frac{4kT}{ze}\right)\tanh^{-1}\left[\tanh\left(\frac{ze\zeta_0}{4kT}\right)e^{\left(\frac{-y}{L_D}\right)}\right] \tag{2.15}$$

where $L_D \equiv \sqrt{\frac{kT\varepsilon_{\mathrm{w}}}{2Iz^2e^2}}$ is known as the Debye length. At the oxide/electrolyte interface, the sheet charge imposes a boundary condition $\frac{d\zeta}{dy} = \frac{\sigma}{\varepsilon_{\mathrm{w}}}$. which leads to the following expressions:

$$\sigma = \left(\frac{2kT\varepsilon_{\mathrm{w}}}{zeL_D}\right)\sinh\left(\frac{ze\zeta_0}{2kT}\right) \tag{2.16}$$

$$C_{\mathrm{G}} = \frac{d\sigma}{d\zeta_0} = \frac{\varepsilon_{\mathrm{w}}}{L_D}\cosh\left(\frac{ze\zeta_0}{2kT}\right) = \frac{\varepsilon_{\mathrm{w}}}{L_D}\sqrt{1 + \left(\frac{\sigma zeL_D}{2kT\varepsilon_{\mathrm{w}}}\right)^2} \tag{2.17}$$

where ζ_0 is the potential at the oxide/electrolyte interface, and C_{G} is the differential capacitance of the counter-ions in diffuse layer that are involved in surface-charge screening. In fact, between the diffuse layer and dielectric surface, there also exists an inner layer of specifically adsorbed ions on the dielectric surface, and an outer layer of

hydrated ions, which define the inner and outer Helmholtz planes, respectively. These planes alter the charge and potential distribution across the interface, and contribute to a series capacitance that is collectively called C_S, or Stern capacitance. The potential drop across this layer can also be described by $(\chi^{Sol} + \delta\chi^{Sol}_{ox}) - (\chi^{ox} + \delta\chi^{ox}_{Sol})$, that considers the energy cost for a test charge to move from the electrolyte phase to oxide phase. [71] However, this capacitance is typically much greater than C_G which is in series, thus the series capacitance at the interface converges to C_G.

Having derived the potential-charge relations in electrolyte, insulator, and silicon, it is now possible to match the boundary conditions to obtain a potential profile in the sensor region. To first order, the abrupt potential jumps at the interfaces are ignored, which leads to a potential profile illustrated in Figure 2–3:

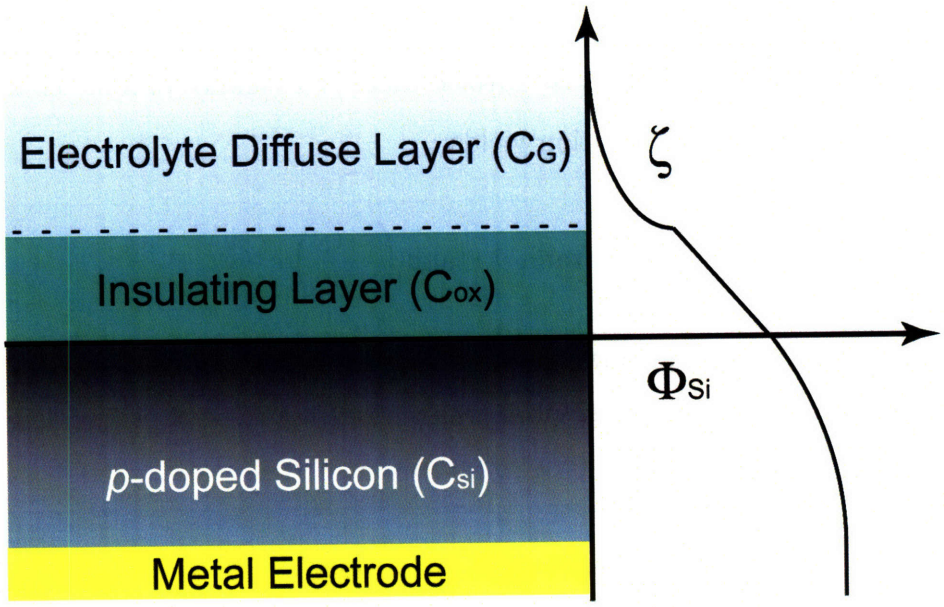

Figure2–3: Conceptual Illustration of potential profile of EIS sensor. Structure and potential profile not drawn to scale.

The structure can be modeled as three capacitor in series, and potentials are exponentially, linearly, and quadratically related to distance in the diffuse, oxide, and silicon regions, respectively.

2.3.1 Calibration of EIS sensor

Of particular interest to the users of an EIS sensor is how a change in electrolyte-oxide surface potential translates to a change in AC conductance through the entire structure, which is a parameter measured by the user. This information is important since it allows one to convert a differential current output to a relative surface potential response caused by binding of charged molecules to sensor surface. Unfortunately, unlike a MOS capacitor, in practice there is no straightforward way to impose a known quantity of charge or potential value on the surface of an EIS structure. An indirect way to obtain this information is to apply a step change in the silicon-bias and measure the change in impedance value of the structure. This approach relies on the assumption that the overall impedance is dominated by the silicon capacitance whose value is a function of the potential difference across the structure. Thus, if all potential drop occurs across the silicon, altering the potential at the oxide surface has the same effect on the capacitance of silicon as applying the same magnitude of potential change to the metal bias of bulk of silicon.

To analyze the validity of this approach, the change in potential profile across the entire EIS structure must be analyzed quantitatively. In particular, the following analysis will focus on the change in the electrolyte/oxide potential value as a function of an applied voltage change on silicon back-bias, since in an ideal case the former should be 0. Define C_{OS} as the series capacitance of oxide-silicon, and $C_{\mathrm{T}} = \left(\frac{1}{C_{\mathrm{G}}} + \frac{1}{C_{\mathrm{ox}}} + \frac{1}{C_{\mathrm{Si}}}\right)^{-1} = \left(\frac{1}{C_{\mathrm{G}}} + \frac{1}{C_{\mathrm{OS}}}\right)^{-1}$ as the total series capacitance, then the potential drop across C_{G} for a differential applied voltage V is.

$$dV = \frac{C_{\mathrm{G}}}{C_{\mathrm{T}}} d\zeta \tag{2.18}$$

The expression can be integrated yielding exact solutions for potential drop across diffuse layer as a function of applied voltage:

$$\zeta = \frac{2kT}{ze} \sinh^{-1}\left[\left(\frac{zeL_{\mathrm{D}}C_{\mathrm{T}}}{2kT\varepsilon_{\mathrm{w}}}\right) V + \zeta_0\right] \tag{2.19}$$

where ζ_0 as derived previously is the surface potential due to fixed charge on

dielectric surface in the absence of applied voltage. Therefore, for the calibration to be accurate, $C_G \gg C_T$, or equivalently, $C_G \gg C_{OS}$ must hold. Using typical values in biological experiments and silicon microfabrication, the effects of varying dopant concentration between 10^{13} and 10^{19} cm^{-3}, oxide thickness between 1 and 330 nm (typical native oxide thickness is 1.5 nm [81]), and ionic strength between .32 and 100 mM on the $d\zeta$ to dV ratio are shown in Figure 2–4.

As can be seen on all curves, the ratio is minimized by reducing the dopant concentration, which as shown previously, minimizes the capacitance of the depleted region in silicon. Interestingly, minimizing the gate oxide thickness, which improves sensor sensitivity by optimizing dC_{Si}/dV ratio, actually causes more shift in zeta-potential given a change in V. Intuitively, this makes sense since reducing oxide thickness increases the series capacitance C_{OS}, which reduces the C_G/C_{OS} ratio. This analysis shows there is a trade-off between maximizing sensitivity by scaling down oxide thickness at a risk of reducing the accuracy of sensor calibration through changing the sensor-bias. Given the same zeta-potential, lowering ionic strength actually improves the accuracy of the calibration, as higher concentration of ions increases C_G. However, it is normally undesirable to increase ionic strength, as it reduces Debye screening length, making the sensor less sensitive to charges near the surface. Overall, this analysis reveals that a $d\zeta$ to dV ratio of less than 1% is achieved in most cases, making the method a practical approach for calibrating the capacitive response for change in surface potential. However, in all cases $dC_{Si}/d\zeta_0$ is always overestimated by this method, since the total change in voltage differential across the series oxide/silicon capacitor due to an applied an applied voltage dV on substrate is $dV + d\zeta_0$, and $d\zeta_0$ is a non-zero quantity that has the same sign as dV.

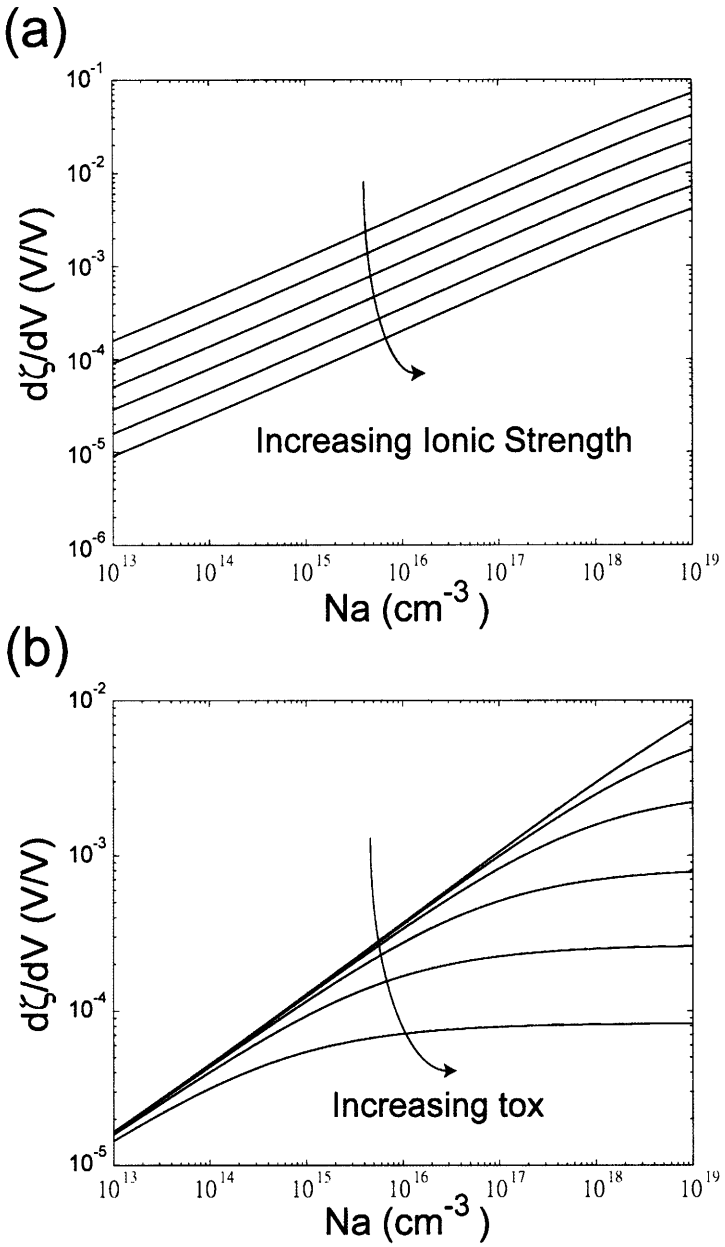

Figure2–4: The effect of scaling electrolyte and fabrication parameters on C_G to C_{OS} ratio. In (a), the oxide thickness is held constant at 1 nm and ionic strength is varied between .32 and 100 mM for the different curves, and in (b) the ionic strength is held at 30 mM while oxide thickness is varied between 1 and 330 nm for the different curves. ζ potential of -.1 V is used, and the silicon is biased half-way between the threshold and flatband voltage.

2.4 EIS Measurement of Polyelectrolyte Multilayer Deposition

This previous section deals with the electrostatics of an EIS system with no adsorbed biomolecules but only an infinitesimally thin layer of adsorbed charges on sensor surface, but in most practical situations the analyte of interest is specifically captured on the sensor surface within the Debye screening length so charges can be sensed. This section introduces a circuit model for the surface-based sensing of nucleic acids through polyelectrolyte multilayer assembly using an EIS device.

2.4.1 Qualitative Overview of Electronic Multilayer Deposition Sensing

Single-stranded nucleic acid is typically attracted and captured to the surface by hybridization with immobilized capture probe. The capture probe can be immobilized through covalent attachment [82] or physisorption [64]. The latter can involve first passivating the sensor gate oxide surface with positively charged polymers such as poly-L-lysine (PLL), then introducing unmodified single-stranded DNA probe. Since DNA carries an intrinsic negative charge per base, it can be attached to the sensor surface through electrostatic interaction. While the orientations of the immobilized nucleic acid probes may be less defined, such an approach has several advantages over the covalent attachment methods including simplicity and robustness. The electrostatic attraction between oppositely charged polymers has the least steric demand of all chemical bonds and the polymer can bridge over underlying defects on the substrate and ensures uniform and high-density surface functionality. [83] Another feature of functionalization based on electrostatic interaction of charged polymers is that it permits layer-by-layer assembly. For example, after depositing DNA on PLL, a surface charge reversal occurs due to overcompensation of negative charges by the former, which gives the surface again the ability to adsorb another layer of positively charged molecules, and so on. Robust assembly of multilayers of oppositely charged

polymers can be repeated hundreds of times to yield films on the order of 10μm thick. [84] While the film thickens after deposition of each layer, Fritz et al. observed that the electronic sensor response oscillates depending on the charge of the newest layer deposited (Figure 2–5), and the amplitude of the signal did not seem to decrease significantly as the thickness grow

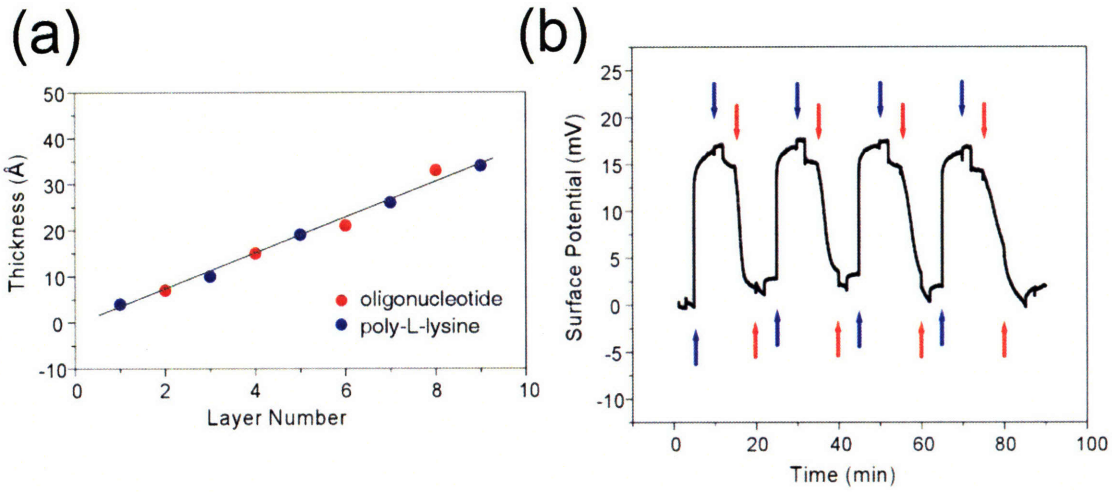

Figure 2–5: Thickness (a) and potential (b) values following the injections of poly-L-lysine (blue arrow) and oligonucleotide (blue arrow) were acquired using an ellipsometer and field effect sensor. Figures are adapted from [64].

Even though the EIS structure measures the overall series impedance of the electrical pathway including that of the multilayer film, the signal amplitude does not decay appreciably with increasing multilayer thickness. The observation suggests that the sensor is primarily sensitive to changes in surface potential of the multilayers rather than that in the dielectric properties of the surface. This feature allows one to perform multiple rounds of DNA measurements by resetting the baseline signal by re-depositing PLL onto the surface. At the same time, the additive surface regeneration process ensures that the surface is saturated by positive charges and the binding capacity does not degrade for multiple DNA analyses. Thus, the thesis explores the practicality of using layer-by-layer assembly technique for multiple measurements of PCR product.

2.4.2 Modeling of Multilayers and EIS Excitation Electrodes as Circuit Elements

An aim of the equivalent circuit analysis for EIS monitoring of polyelectrolyte growth is to avoid limiting oneself to a particular implementation and material of EIS sensor. In Section 2.2, the electrolyte, insulator, and semiconductor portion of the device was each modeled as a capacitor, and their dependence on ionic strength and applied voltage was provided.

Even though there is a lack of quantitative understanding of the electrical characteristics and how they are affected by external physical parameters, order-of-magnitude extrapolations are still possible given experimental results reported in the literature. The dielectric and ionic conductance of polyelectrolyte multilayers have both been measured [85, 86], and thus it is reasonable to model the film as a resistor in parallel with a capacitor (Figure 2–6). The dielectric properties of the films are very sensitive to temperature and moisture content, and ionic conductivity depends on solution pH and internal layer chemistry. [87, 88] Permeability has also been shown to be proportional to layer thickness. [89] The conductivity of the multilayer film is low, for example, 1×10^{-12} S/cm has been measured for poly(allylamine hydrochloride)/poly(acrylic acid) multilayer. [85] The effective dielectric constant measured is greater than 100 when the film is solvated, which is more than an order of magnitude greater than that of oxide (3.9). Direct evidence of surface charge alteration has been verified on colloids by electrophoresis [90] that shows ζ-potential alternates between positive and negative values depending on the layer number. In addition, the amplitude of oscillation reported is very consistent throughout, as has been measured by EIS sensors. [81]; futhermore, the bulk of the multilayer complex has been shown to be electrically neutral [91] with very low concentration of counterions [92]. Thus in DC analysis, one can model the multilayer as a dielectric layer that has finite resitivity with a sheet charge on the multilayer-electrolyte interface.

The equivalent circuit of signal electrode has been provided in Ref. [93]. At the electrode/bulk electrolyte interface there exist a Stern and diffuse layer capacitance

(C_S and C_G, respectively) just like that of the insulator/electrolyte interface for EIS structure. Since the electrode may be conductive, a charge transfer resistance R_{ct} may also be present. The charge transfer resistance is in series with in series with Warburg impedance Z_w, which reflects the impedance due to diffusion limited ionic charge transport whose magnitude scales inversely with frequency. [94] However, for ideally polarized electrode, charge can only cross the electrode/electrolyte interface via capacitive coupling, thus R_{ct} and Z_w will not be present (Figure 2–6).

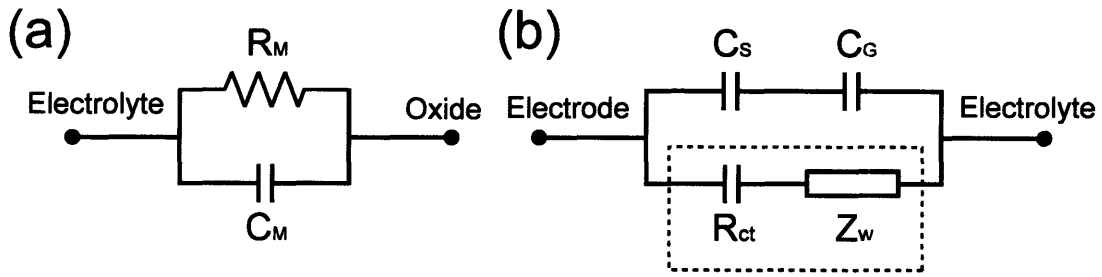

Figure 2–6: Equivalent circuit models for (a) polyelectrolyte multilayer and (b) excitation electrode. The components inside rectangle are not present if the electrode is ideally polarized.

2.4.3 Complete Equivalent Circuit Model for EIS Sensing of Polyelectrolyte Multilayer Deposition

To combine the individual elements into a complete equivalent, the bulk electrolyte impedance must also be considered. The permittivity of NaCl salt solution with concentration 0.1 M differs from that of water by less than 1% [95], but conductance is enhanced strongly by the addition of strong electrolyte. The overall conductivity of bulk solution can be estimated by considering the spread resistance given by:

$$R_b \approx \frac{1}{\kappa}\sqrt{\frac{\pi}{WL}} \tag{2.20}$$

where κ is the electrolyte conductivity, and W and L are the effective width and length of the sensor surface. The equation applies if its area is small compared to that

of the excitation electrode. A small-signal equivalent circuit for EIS measurement of polyelectrolyte multilayer deposition is as follows:

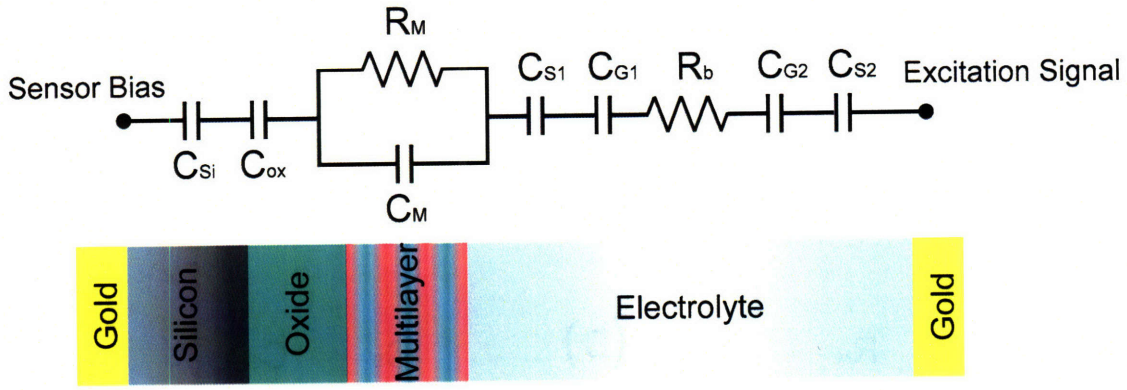

Figure 2–7: Combined small-signal circuit model for EIS sensing of polyelectrolyte multilayer assembly.

Define C_{GS} as the series capacitance of C_S and C_G. Typical values are derived from calculated [93] and empirically measured parameters [64,85] for a solution containing 10 mM NaCl 10^{15} cm^{-3} p-doped silicon, and oxide thickness of 10 nm. Assuming the excitation frequency is 5 kHz, and sensor area is 100×100 μm^2:

Parameter	Value	Actual Impedance (Ω)
C_{Si}	$0 \sim 1.2 \times 10^{-8}$ F cm^{-2}	$0 \sim 2.7 \times 10^{7}$ Ω
C_{ox}	3.5×10^{-7} F cm^{-2}	9×10^{5} Ω
C_M	$\sim 1 \times 10^{-5}$ F cm^{-2} for 10 layers	$\sim 3 \times 10^{4}$ Ω
R_M	5 Ω cm^2	$5 \times 10^{4}\Omega$ cm^2
C_{GS}	$1 \times 10^{-5} \sim 1 \times 10^{-4}$ F cm^{-2}	$3 \times 10^{3} \sim 3 \times 10^{4}$ Ω
R_B	3×10^{5} Ω	3×10^{5} Ω

Table 2.1: *Impedance values for equivalent circuit elements*

The effective impedance of multilayer is approximately $2 \times 10^4\Omega$. The total impedance of the structure ranges from $1.3 \times 10^6\Omega$ to greater than $2.8 \times 10^7\Omega$. The series impedance value is clearly dominated by the impedance of the depletion region in silicon, which can contribute to 20-fold change in series impedance value. Furthermore, the calculated impedance value of the polyelectrolyte multilayer is relatively negligeable compared to the total impedance of the equivalent circuit. Assuming the overall thickness of a multilayer grows linearly with respect to number of layers de-

posited, then about 100 layers is required in order for the impedance of the multilayer to become 1% of the maximum impedance value of depleted region in silicon. The validity of these assumptions will be examined in the following section. The difference in capacitance values can explain the cyclical response observed on an EIS platform that does not seem to degrade with increasing number of layers. In particular, most surface potential voltage will drop across the silicon depletion zone, and this cyclical shift in bias condition due to depositions of oppositively charged polyelectrolytes will induce a greater change in C_{Si} than thickness-induced change in C_{M}. Thus, the resulting overall impedance value, which determines the EIS sensor signal output, will follow a cyclical pattern.

2.5 Physical Characteristics of Layered Polyelectrolyte Complexes

Unlike MOS or EIS, the study of multilayer assembly is still nascent [96], and theories describing polyelectrolyte multilayer assembly range from phenomological descriptions of layer composition to quantitative models based on mean-field and electrostatics. This section aims to provide a survey of current literature emphasizing the structural composition, electrical attributes, and scaling parameters of polyelectrolyte multilayer relevant to electronic sensing.

2.5.1 Experimental Observations of Polyelectrolyte Multilayer Properties

Multilayer formation begins with the adsorption of polyelectrolyte in solution to oppositely charged surface, and has been the subject of a large number of experimental studies. [97, 98, 99] The general understanding is that highly charged chains adsorb as thin layers with a flat chain conformation, and the most important consequence is charge overcompensation occurs on the surface, which serves as a prerequisite for the subsequent deposition of oppositely charged polymers. Through pH variations, salt

screening or charge dilution along the chain, more flexible chains in thicker 'loopy' first layers can be observed. [100] At high ionic strength, electrostatic interactions become less relevant, thus a stronger charge overcompensation can be achieved.

The adsorption of a polyion layer to preformed polymeric layers differs largely from adsorption to rigid, charged surfaces. [101] An important process is the entanglement into the outer surface of a multilayer, as this is driving the complexation and determining the segment distribution width of each layer. For most polyion payers, a linear growth regime for layer thickness with layer number is observed. [64, 96, 102] This is consistent with the assumption made in Section 2.4. However, substantially lower absorbed amount in the first few layers before a stationary regime of a constant increase per layer has been observed for weakly charged surfaces, and is explained by the multiplication of surface functionality. [83, 103] Interstingly, in some rare cases, no linear regime of regular growth is reached, and the thickness increase can be pseudo-exponential e.g. poly-L-glutamic acid/poly-L-lysine pair [104], which has been correlated with an increasing surface roughness and additional surface area providing more charges for complexation [105].

The adsorption of polyelectrolyte multilayer from salt solutions of varying ionic strength was the first approach to control layer thickness over a wide range. [96] However, thus far no single power law explained the scaling of thickness with respect to salt concentration observed experimentally. Some publications reported a linear dependence on salt [106, 107], while others found it scales with concentration to the power of between 0.05 and 0.5 [105, 108]. A theoretical model predicting linear dependence of thickness increment on salt concentration will be summarized in Section 2.5.2.

The internal structure and distribution of the adsorbed polyelectrolytes within the multilayers have also attracted major interest. Results have shown that about one third of the charges of the terminating layer are complexing with the underlying polyion layer, and the remaining charges are compensated by counter-ions, which can be released on adsorption of a next layer. [109, 110] The density of the multilayer film has been measured by X-ray reflectivity experiments that reported an increased

density in the complexation region between the interface of oppositely charged polyelectrolyte layers, whereas the first layer close to the surface and the loops of the outermost layer are less dense. [111] The strong layer complexation and interpenetration also prevent the formation of well-separated layers with defined interfaces. For example, by neutron reflectivity, only after the formation of a multilayer with the distance between the deuterated layers exceeding several monolayers could a clear contrast leading to interferences between reflections at internal interfaces be observed. [101]

An important property of the multilayers is macroscopic electrical neutrality within the multilayers. [91] The neutrality can be fulfilled this way by intrinsic charge compensation i.e. a layered complex being formed with an exact 1:1 stoichiometry of polycation and polyanion charges, involving ion pair formation with the previous layer until the charges of the latter are compensated. However, whether counter ions facilitated extrinsic charge compensation within multilayers has remained controversial. [112] For example, a model has proposed that if Debye length is less than the layer extension, some polyion charges can remain extrinsically compensated within the multilayer. [113] This creates a layered arrangement of positive and negative excess charge which makes the structurally globally but not locally neutral. However, studies using neutron reflectivity and radioanalytical studies showed no substantial amount of counter-ions was found in multilayers. [91, 114] Also, in electrochemical experiments, because the internal counterion concentration was very low, there was virtually no exchangeable ions, and ion transport was mediated by salt ions in solution, which made multilayers a 'reluctant' ion exchanger. [92] The low concentration of ions within multilayers implies that charge screening does not charge-screening law in an ionic solution does not apply within the structure, which could potentially explain why the field-effect sensor is able to detect surface charges on a multilayer several Debye lengths away from its surface.

Another noteworthy aspect of multilayer is that surface charge on the outermost terminating layer has been known to affect the electrostatic properties of the multilayer bulk. IR spectroscopy showed that the dissociation of carboxylic groups in multilayers was increased by a terminating polycation layer, and decreased by a ter-

minating polyanion layer [115], an observation that formed the experimental basis of a model that describes the internal dissociation in dependence of the outer potential[1]. [113] Furthermore, water mobility in multilayer also oscillated in dependence of the surface potential as observed by water spin measurements. [116]

2.5.2 Theoretical Study of Polyelectrolyte Multilayer Growth

This section presents a quantitative model which could be used to predict how changes in buffer conditions could affect the electronic measurements of polyelectrolyte multilayer assembly, in particular, by affecting the multilayer thickness. In recent years, a number of theoretical models have been developed for multilayer growth. [117,118,119] A common feature among these models is that simultaneous equations of Edwards mean-field equation for polymer adsorption to surfaces and Poisson-Boltzmann equation for potential profile near surface are solved numerically or analytically with appropriate boundary conditions at the multilayer-electrolyte interface. This section will summarize the approach taken by Castelnovo et al. who derived simple analytical solutions to describe the adsorption of polyelectrolytes onto a charged wall and the concentration profiles of the subsequent multilayer formation.

The model relies on several assumptions that either reflect experimental observations or simplify the analysis. First, as discussed in the previous section, after several layers of deposition, the thickness of one layer depends on the salt concentration but not the surface charge on the substrate. Second, the net charge of the multilayer is carried by the last year, with the preceding layers being globally neutral. Only symmetrical complexes where the polycations and polyanions have same degree of polymerization and carry the same charges are considered. The analysis only applies to the limit of high ionic strength. The solution contains monodisperse flexible polyelectrolytes in a Θ solvent with salt, each chain of length N having Nf positive charges. The monomer size is a, and the substrate has a charge density of $-\sigma$.

The analysis begins with the adsorption of the first layer. Polymer concentration

[1]The same model also claims the existence of extrinsic ionic compensation within multilayer. See previous paragraph for more details.

and electrostatic potential near the surface are governed by Edwards equation and Debye-Hückel equation:

$$\frac{a}{6}\frac{\partial^2\psi}{\partial z^2} = (fV(z) - \mu)\,\psi(z) \tag{2.21}$$

$$\frac{\partial^2 V}{\partial z^2} = \kappa^2 V(z) - 4\pi l_{\mathrm{B}} f \psi^2(z) \tag{2.22}$$

where $\psi(z)$ is the polymer order parameter and is related to the local polymer concentration by $\psi^2(z) = c(z)$. μ is the chemical potential of the surface, and $V(z)$ is dimensionless electrostatic potential $V(z) = q^2\varphi(z)/kT$. l_{B} is the Bjerrum length $l_{\mathrm{B}} = q^2/4\pi\varepsilon kT$, and κ^{-1} is the Debye length. This leads to the following boundary conditions on the substrate must be included:

$$-\frac{1}{\psi}\frac{\partial\psi}{\partial z}\Big|_{z=0} = \frac{1}{d} \tag{2.23}$$

$$\frac{\partial V}{\partial z}\Big|_{z=0} = 4\pi l_{\mathrm{B}}\sigma \tag{2.24}$$

The first boundary condition for order parameter describes the short-range potentials whose strength is characterized by an extrapolation length d. The second boundary condition is Poisson's equation for charges on the substrate. The above equations and boundary conditions must be satisfied for solutions to concentration profiles of polyelectrolyte adsorbed onto a charged surface.

Essentially, the strategies employed by Castelnovo et al. is to simplify analysis in the limit of high ionic strength by eliminating the need to solve Poisson-Boltzmann equation by modifying the boundary conditions of mean-field equation for polymer adsorption to take into account of electrostatic interactions. It can be shown that in the limit of high ionic strength, the typical length scale of variation of the order parameter is much larger than the screening length i.e. $d \gg \kappa^{-1}$. In this case, the extrapolation length d can be replaced with d_{eff}, which describes interactions of nonelectrostatic origin (van der Walls, hydrogen bonding, hydrophobic effects etc.) as

well as of electrostatic origins. In the same light, the characteristic excluded volume for short-range excluded-volume interactions of polymers can be computed based on screened electrostatic interactions where $v_{\mathrm{el}} = \frac{4\pi l_{\mathrm{B}} f^2}{\kappa^2}$.

By transforming the original equations into this simplified form described above, the original polyelectrolyte adsorption problem now has the same format as the problem of neutral polymer adsorption, and can be solved by the same techniques. The solution for concentration reads as:

$$c(z) = \frac{a^2}{3v_{\mathrm{el}}\left(z + d_{\mathrm{eff}}\right)^2} \tag{2.25}$$

and the total adsorbed amount is $\Gamma_1 \simeq \frac{2\sigma}{f}$ after integration.

For adsorption of additional layers, it is assumed the total amount of adsorbed polyelectrolyte remains fixed, since experimentally desorption has been known to be a very slow process. The concentration profile of the subsequent layers can be derived by the following arguments. Since electrical neutrality is assumed to exist in the bulk of the multilayer, c_+ and c_-, the concentrations of polycations and polyanions, must be equal. However, in the region near substrate surface, there is attractive or repulsive interaction with the charges on the surface, and therefore an excess of one species over another is expected in order to compensate the surface charge. The difference decays from the substrate surface with a characteristic length $\xi_{v_{\mathrm{el}}}$ until $c_+ = c_- = c_{\mathrm{c}}$, which means the density of the multilayer bulk is $2c_{\mathrm{c}}$. Again, by analogy to the neutral polymer adsorption problem, the concentration profile of the outermost polyelectrolyte layer decays in a way similar to that in an adsorbed polymer layer of neutral polymers with an excluded volume v_{el} (Figure 2–8):

$$c_-(z) \sim \frac{a^2}{v_{\mathrm{el}}\left(z + d\right)^2} \tag{2.26}$$

assuming the substrate is negatively charged. The length d is imposed by matching the profile with the equilibrium density inside the complex $c_-(z = 0) = c_{\mathrm{c}}$. By integrating to obtain the total net charge on the outermost layer:

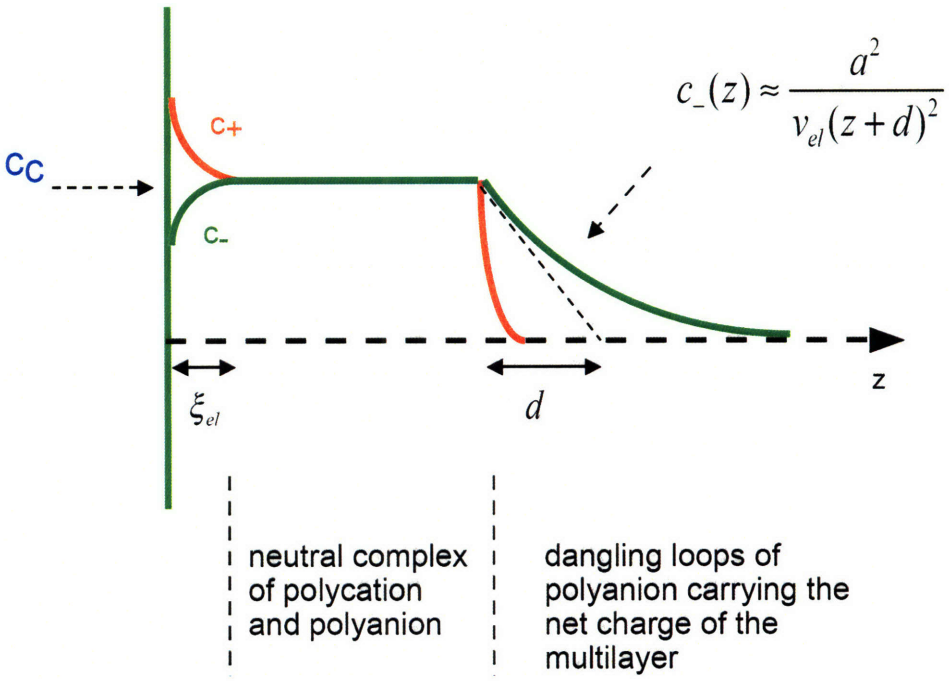

Figure2–8: The concentration profile of polycation and polyanions desposited on a negatively charged substrate, as predicted by a physical model at the limit of high ionic strength. Image adopted from [117].

$$\Delta\Gamma = \int_0^\infty dz c_- (z) = \frac{a^2}{v_{\mathrm{el}} d} \sim a \left(c_{\mathrm{c}}/v_{\mathrm{el}}\right)^{1/2} \sim \frac{1}{w^{2/3}} \left(1 - \frac{f^2}{n^{2/3} l_{\mathrm{B}}^{1/2} a^2 w^{2/3}}\right) \tag{2.27}$$

where w is three-body interaction parameter, n is the ionic strength, and an approximation of c_{c} is derived by considering the thermodynamics of polyelectrolyte complexation[1]. [117] The increase in thickness per layer adsorbed can be estimated by:

$$L \sim \frac{\Delta\Gamma}{c_{\mathrm{c}}} \sim \frac{w^{2/3} n a^2}{f^2} \tag{2.28}$$

Therefore, the model predicts that incremental thickness per layer deposited scales with ionic strength but not substrate surface charge density, which is consistent with experimental observation. The model does have limitations; in particular it is only valid for high ionic strength, and at lower ionic strength, the range of electrostatic interactions increases and polyelectrolyte layers interact more strongly with each other, introducing non-trivial correlations.

2.6 Optimizing PCR for Electronic Sensing

A recurring theme in the previous sections is the interactions of ionic strength, polyelectrolyte multilayer formation, and electronic sensor signal. Due to charge screening effects, it is often desirable to minimize ionic strength for higher sensor sensitivity. Since a goal of this thesis is to implement direct label-free detection of PCR product without post-processing steps such as desalting using electronic sensing of multilayer assembly, PCR buffer will be used as a flow buffer to for sensor stabilization, surface rinsing, and baseline establishment. In this section the effects of tuning various PCR parameters, particularly ones concerned with ionic conditions of the PCR mix, will be considered. Strategies to optimize PCR buffer for electronic sensing will be presented.

[1] $c_{\mathrm{c}} \sim \frac{f^2}{a^2 n w^{4/3}} \left(1 - \frac{f^2}{n^{2/3} l_{\mathrm{B}}^{1/2} a^2 w^{2/3}}\right)$

2.6.1 Effects of changing concentrations of different PCR components

The effects of changing the concentrations of various PCR components on amplification [120, 121] and sensing will be discussed. In general, as long as there is sufficiently high concentration of Taq polymerase in the reaction mixture (typically 2 Units/25μL), the reaction will saturate to a level that is relatively independent of the enzyme concentration. A concentration that is too high may however result in unspecific product. Increasing starting template concentration also has similar effect when performing multiplex PCR, but for PCR reaction involving only one primer-pair the template concentration dependence is usually less pronounced. The concentration of the primers must be carefully optimized to balance between product yield and specificity, and generally between 100 and 1000 nM of each primer is used. The product yield can correlate strongly with dNTP concentration, but since dNTP tends to bind and trap Mg^{2+} from Taq polymerase, which requires the cation for processivity, the concentration of this electrolyte must be carefully adjusted. The side effects of adjusting $MgCl_2$ will be considered in the following section. Given the same concentration of reagents, the performance of the reaction is generally independent of total reaction volume in the absence of surface adsorption effects. [51] However, interestingly, small volume PCRs may be very beneficial when using small amounts of DNA template. It has been shown that at a constant amount of template DNA, the yield of PCR product per microliter reaction is higher when the reaction volume is 5 μL compared to 100 μL. This suggests that micro-PCR systems may enable successful amplification that otherwise fails when larger reaction volumes are used.

The most commonly used PCR buffer contains Tris, KCl, and $MgCl_2$, and the last two rank among the most important determinants of a well-designed reaction. Tris-HCl concentration does not typically influence the outcome of the reactions over a large range of concentrations (from 0.75x to 5x of 20 mM), but KCl concentration can have great impact on the yield and specificity of the reaction. Empirically, an increase in salt concentration makes shorter molecules amplified preferentially if the reaction is

designed to amplify multiple products. KCl can also be used to decrease the strigency of the reaction when it is desirable to maintain a certain annealing temperature, allowing primers that have low melting temperature to anneal successfully. Magnesium ion concentration has impact on multiple parameters in reaction in addition to changing the melting temperature of the primers. As mentioned previously, dNTP and Taq both bind $MgCl_2$, thus often small increases in the dNTP concentrations can rapidly inhibit the PCR reaction due to $MgCl_2$ trapping, whereas subsequent increases in magnesium concentration often compensate for this inhibition. Thus, $MgCl_2$ is often required to increase melting temperature of primers and increasing enzyme activity, which reduces specificity; however, increasing [$MgCl_2$] above certain level can actually make the reaction more specific sometimes, as higher concentrations of MgCl2 appeared to inhibit the polymerase activity. This feature makes $MgCl_2$ one of the most sensitive parameters in PCR optimization.

2.6.2 Effects of Changing Concentrations of different PCR components

The melting temperature of the primers, which is defined as the temperature at which statistically half of the primers will anneal to its complement sequence, depends directly on the ionic strength of the solution, since screening of negative charges on the backbone of nucleic acids is critical to duplex stability. Therefore, the effects of adjusting ionic strength such as specificity and yield can be primarily explained by whether a particular annealing temperature is appropriate for a primer given its melting temperature. If the melting temperature is too high, then it is likely the primer will bind incorrectly leading to amplification artifacts, but if the melting temperature is much lower than the annealing temperature, no primer extension can take place. Furthermore, because extension begins immediately upon enzyme's binding to the primer/template pair, the annealing temperature, hence the melting temperature, must not be too much below the optimal reaction temperature for Taq polymerase, 72 °C, or the partially extended primers may denature prematurely when

the tube temperature is ramped to extension temperature. To obtain maximum signal from field-effect sensor, however, it is desirable to maximize the charge screening length which is inversely proportional to ionic strength. The ionic strength of PCR buffer is:

$$I_{\text{PCR Buffer}} = [\text{NaCl}] + 3\,[\text{MgCl}_2] + I_{\text{Tris-HCl}} \tag{2.29}$$

Since Tris-HCl is a weak base, its contribution to the ionic strength is secondary to that of strong electrolytes NaCl and $MgCl_2$. It follows that a first simple target is then to minimize ionic strength by varying the concentrations of NaCl and $MgCl_2$ simultaneously while preserving the same annealing temperature for a particular primer sequence to allow successful initial extension during annealing.

The melting temperature T_{m} depends on factors such as salt concentration, oligonucleotide concentration, and the oligonucleotide sequence. Salt reduces the effect of charge-repulsion along phosphate backbones and stabilizes double-stranded DNA. Higher nucleotide concentration favors the formation of duplex pair, and because G-C pair contains 3 hydrogen bonds rather than 2 for A-T pair, GC-rich sequences have a higher T_{m}. An equation taking these effects into account has been derived by fitting empirical data [122]:

$$T_{\text{m}} = 81.5 + 0.41\,(\%GC) - \frac{500}{L} + 16.6 \log [M] \tag{2.30}$$

where L refers to the length of the oligonucleotide, and $[M]$ is the concentration of monovalent cations. However, the formula lacks a theoretical basis, and does not consider nearest neighbor hydrophobic base-stacking interaction. This is taken into account in the model developed by Santa Lucia et al. [123] who considers the enthalpy and entropy changes associated Waston-Crick nearest neighbor base-stacking and hydrogen bonding interactions:

$$T_{\text{M}} = \frac{\Delta H}{\Delta S[K^+] + R \ln \left[\frac{C_{\text{T}}}{2}\right]} \tag{2.31}$$

where ΔH is the enthalpy term, $\Delta S[K^+]$ is the entropy term as a function of potassium ion concentration, R is the gas constant, and C_T is the total oligonucleotide strand concentration. The entropy and enthalpy terms can be derived by summing the energies of nearest-neighbor interactions. Divalent cations Mg^{2+} also influence the stability of DNA hybrids but their effects are quantitatively different from that of monovalent cations and are still under investigation. To incorporate the effects of magnesium ions to the nearest-neighbor equation, one simplifying strategy is to consider an 'equivalent sodium ion concentration' $[K^+_{equivalent}]$ [124]:

$$[K^+_{equivalent}] = [K^+] + 140 \times [Mg^{2+}] \tag{2.32}$$

This simplifying assumption is backed by the observation that magnesium ions have about 140-fold higher stabilizing effect than monovalent ions in stabilizing DNA duplex in the PCR-relevant concentration. Melting temperature predictions have been calculated for a 20 bp sequence at a typical 200 nM concentration used in PCR in Figure 2–9.

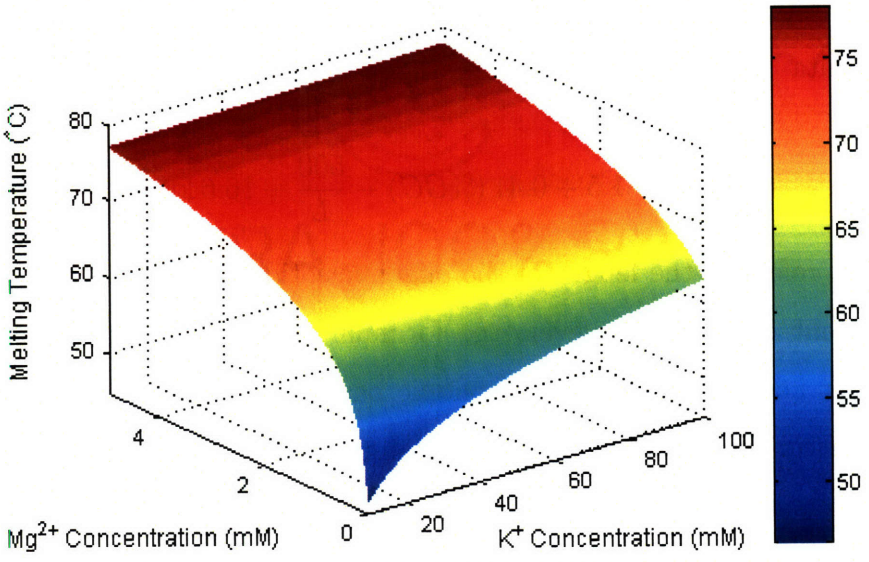

Figure 2–9: Melting temperature calculations as a function of monovalent and divalent salt concentrations. The sequence used in this calculation is 5'-ATCAAGCAGCCATGCAAATG-3' and concentration is 200 nM.

As one can see, only 0.8 mM of $MgCl_2$ is required to achieve equivalent melting temperature as that achieved by 2 orders of magnitude higher concentration of potassium salt, which translates to more than 40-times higher ionic strength. Thus in theory, one can use $MgCl_2$ exclusively in a PCR buffer in order to provide best sensitivity for field-effect sensing. However, given the side effects divalent salt ions have on other components such as polymerase activity and dNTP accessibility, in practice this extreme scenario is most likely not feasible. This analysis does suggest one can potentially lower the ionic strength of a functional PCR buffer without changing the annealing condition, by reducing the potassium chloride concentration significantly and compensating with a slight increase in magnesium chloride concentration to maximize electronic signal from DNA binding.

Chapter 3

Design and Fabrication

This chapter presents the design and fabrication of an integrated microelectronic device for biomolecular amplification and detection. A major goal of this thesis study is to incorporate thermocycling functionality to a standalone silicon-field effect sensor fabricated by a process introduced in [125]. An overview of the sensor design and fabrication will be given, and various fabrication strategies to implement on-chip microfluidic controls and thermal measurement will be reviewed. Finally, a microfluidic architecture that brings together the independently functional sensing and amplification units will be illustrated.

3.1 Field-effect sensor design and fabrication

The field-effect sensors used in this work (Figure 3–1) are oxide-based electrolyte-insulator-semiconductor (EIS) capacitors fabricated on planar silicon substrates and encapsulated by microfluidic channels, which are either etched in glass or molded in poly(dimethylsiloxane) (PDMS) bonded to the silicon substrate. The field-sensitive region is formed by ion-implanation of boron into bulk silicon with phosphorous impurities. The gate dielectric of the sensor region consists of native oxide grown on silicon following an acid treatment of hot piranha (1:3 30% H_2O_2 in H_2SO_4) and HF. The non-sensor region of silicon is covered by a 0.8μm thick field-nitride. To make electrical contact to the sensor, buried conductive traces embedded in silicon formed

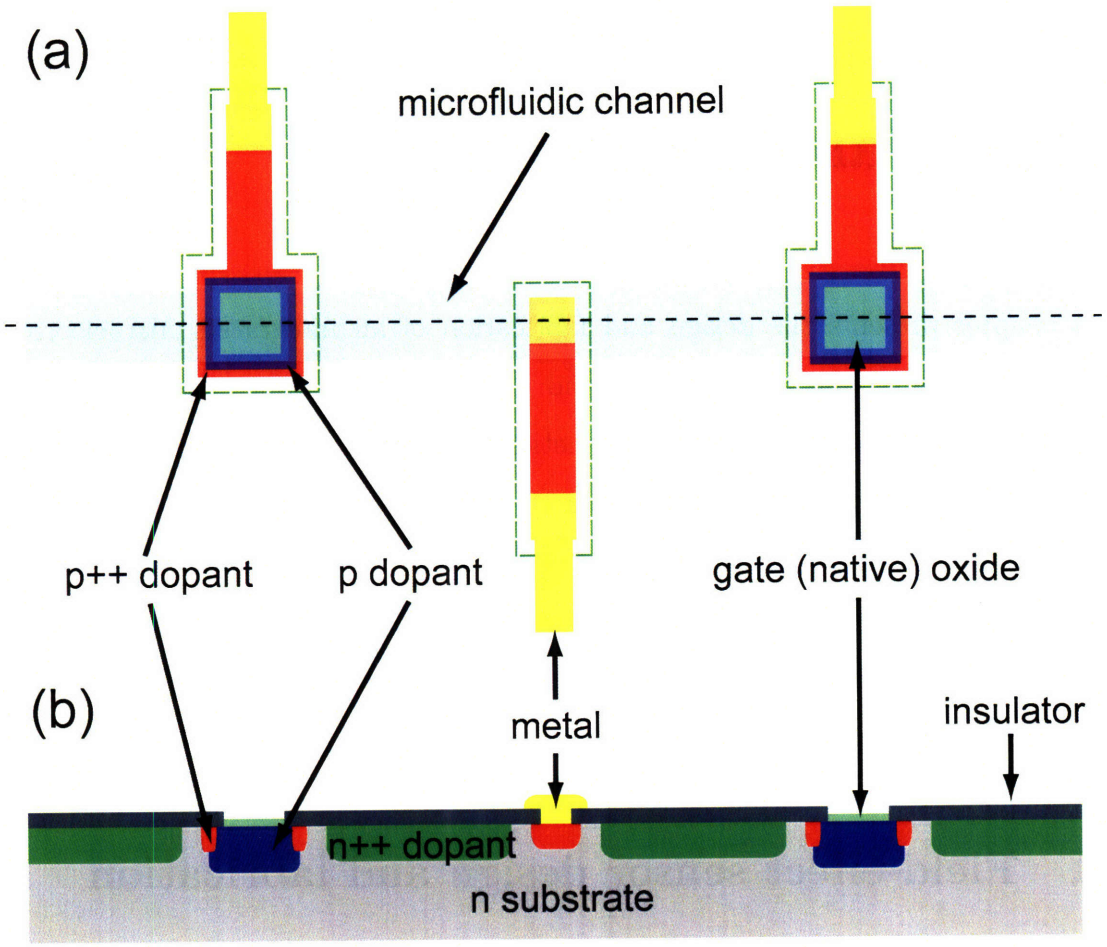

Figure 3–1: Field-effect sensor structure. (a) Top view of field-effect sensor encapsulated by a microfluidic flow-through channel drawn to scale. Shown are a pair of field-effect sensors with sensor area of $80 \times 80\ \mu m^2$ and a gold excitation electrode in between. (b) Cross-sectional view of the field-effect sensor structure at the position outlined by dotted line in (a).

by a concentrated dose of boron ion-implementation are used as an electrical interface to gold traces. This strategy is employed to minimize protrusion on the silicon device around the sensor area to ensure good sealing of microfluidic channels while maintaining a sufficiently conductive electrical pathway to the sensor. Signal is delivered to the sensor through a metal electrode in the microfluidic channel, which is also interfaced to the signal generation source by a metal and buried conductive trace. To ensure that the signal propagates between an excitation electrode and a sensor through a solution but not silicon bulk coupling between the buried conductive traces, the silicon that does not have sensor or conductive-trace dopants are implemented with high dose of n-dopant, which can be electrically biased to serve as a 'ground plane.'

As discussed in Section 2.2, key determinants of field-effect sensor signal strengths include gate oxide thickness and sensor doping level, and these parameters guide the sensor fabrication process design. The maximum signal amplitude scales inversely with gate dielectric thickness, and thus the minimum oxide thickness generated after HF-oxide strip treatment is used. While in theory, it is most desirable to simply minimize sensor dopant concentration for widest range of depletion depth, in practice this strategy is limited by background dopant concentration. The concentration profile of ion-implant in silicon can be modeled as a Gaussian distribution around a depth that is proportional to the ion implanation energy [126], and subsequent thermal-annealing causes the dopants to diffuse and activate electrically. Since the overall polarity and concentration of mobile charge carriers is determined by the difference of the implanted species and background doping level, if the implanted atom concentration is not sufficiently high, inversion of mobile charge carrier polarity can occur near the sensor surface where the background dopant concentration can actually exceed implanted atom concentration. Thus in simulating implant profile, a conservative estimate background dopant concentration that corresponds to the lower end of the wafer resistivity specification is used. When designing the dose levels and annealing parameters for the conductive traces and ground plane, effort is devoted to maximize conductivity while maintaining a reasonable dose level that will not cause the resist

to fail during ion-implantation, or cause excessive surface sputtering or other bulk silicon damages. Using parameters summarized in Table 3.1, a simulated ion-implant profile as shown in Figure 3–2 is obtained.

Implant Species	Dose	Energy $[keV]$	Tilt
Boron, $p++$	2×10^{15}	150	7
Boron, p	2×10^{11}	180	7
Phosphorous, $n++$	1×10^{15}	160	7

Table 3.1: *Implant Parameters*

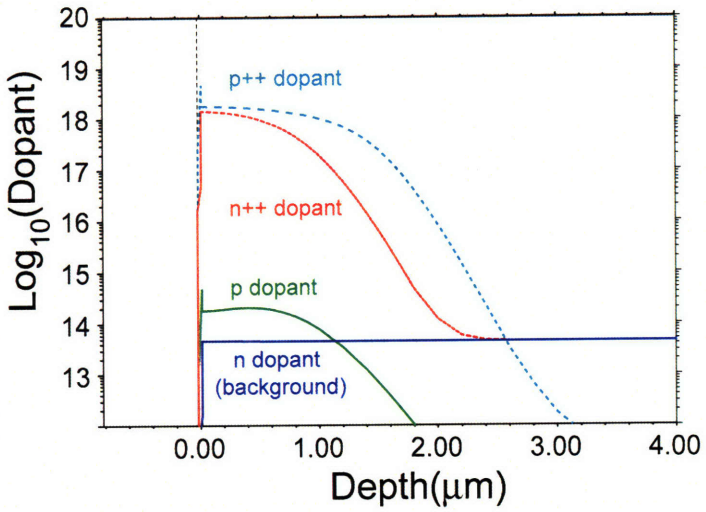

Figure 3–2: Simulated implant profile. An initial background phosphorus concentration corresponding to 10 Ω-cm resistivity is assumed.

The fabrication process of field-effect sensor uses mostly CMOS-compatible tools. [125] First, a 20 nm silicon oxide is thermally grown on 6" n-type (phosphorus doped) 20-50 Ω-cm silicon substrates to form a protective layer against surface sputtering. Ion implantation of active sensor areas (lightly-doped p-type), conductive traces (heavily-doped p-type), and an insulating ground plane (heavily-doped n-type) is then carried out in sequence using photoresist implant masks. The implant oxide mask is then stripped and a 30 nm dry-thermal oxide is regrown to ensure good adhesion with field-nitride, which is deposited by LPCVD. Annealing of the substrate at 1050 °C for 4 hours is then performed to activate and drive in the dopants. Metal contact holes and sensor areas are then etched in the dielectric layer in a single step. Finally,

30 nm Cr and 1 gm Au or Pt are evaporated on the substrate and patterned as conductive traces using a liftoff proces.

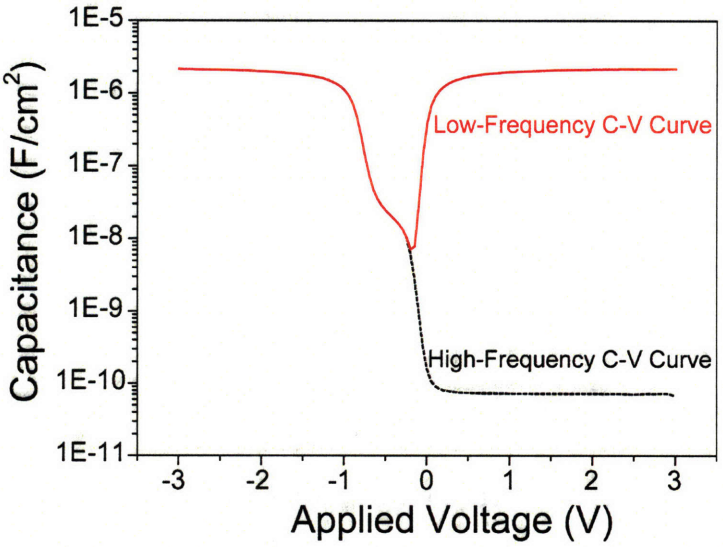

Figure3–3: Calculated MOSCAP C-V characterstic of sensor region. Both low and high-frequency C-V curves are computed with a 1.5nm gate oxide and an imaginary gate metal using the Supreme IV.

Gold traces are expected to account for less than 10 Ω resistance overall. Using Supreme IV process simulation package, additional important electrical characteristics of the device can be obtained. The sheet resistivity of the n++ and p++ areas are 65 and 54 Ω, respectively. This implies that the conductive traces contribute at least 150Ω each to the resistance of the conduction path without taking into account of other bias-dependent depletion effects and contact resistance with metal. By placing an imaginary metal gate on the thin 1.5 nm native oxide gate of the field-sensitive region, a MOS-capacitor C-V curve can be calculated as shown in Figure 3–3. While at less than 10 kHz excitation frequency, one typically expects low-frequency C-V characteristics, experimentally high-frequency behavior is observed [81, 125], thus high-frequency C-V behavior has also been computed. In both cases, a series oxide-silicon capacitance of less than 2.3 F/cm^2 is observed. Furthermore, in high-frequency regime, capacitance on the order of 10^{-10} F/cm^2 can be realized, which is 1000-fold smaller than the minimum computed value used in Chap-

ter 2.4 to estimate the extent to which the overall impedance is dominated by silicon sensor capacitance. Since the effective capacitance spans 5 orders of magnitude, the analysis shows that in the best case scenario silicon is not only essentially a short circuit element at accumulation mode, it is can also be thought of as an open-circuit at depletion or inversion, suppressing any possible current through the EIS electrical pathway. However, in practice, an AC current that travels through other parasitic pathways such as substrate and wire coupling can still be measured, and this defines the background signal of the EIS circuitry.

3.2 Integrated heater design and fabrication

The goal of new process flow design for integrated sensor and heaters is to incorporate the EIS structure with a heater design and microfluidic system that could successfully facilitate both spatial [127] and temporal PCR and its subsequent detection all on-chip. To achieve good thermal isolation for localized heating, a variety of suspended structures has been previously fabricated by several different etching techniques. [128] In this work, fabrication of suspended heaters utilizing a backside KOH etch with a p++ etch stop was attempted. The process involves etching the backside of field-effect sensor device to release a nitride membrane with p++ conductive trace on its backside that can conduct electrically to heat up the membrane locally. A modification to the fabrication process for standalone field-effect sensors to that added additional anisotropic back-side etching for heater release is summarized in Figure 3–4, and temperature profile simulation using FEMLAB thermal modeling was employed to guide heater geometry design (Figure 3–5).

Even though successful fabrication of suspended heater was clearly demonstrated in [129], many challenges were encountered during process development, many of which still requires significant optimization. First, the membranes were less than 1 micrometer thick and required very careful handling during fabrication to prevent their rupture. In addition, the suspended membrane cannot withstand a pressure differential between the frontside and the backside of the wafer, thus rendering the

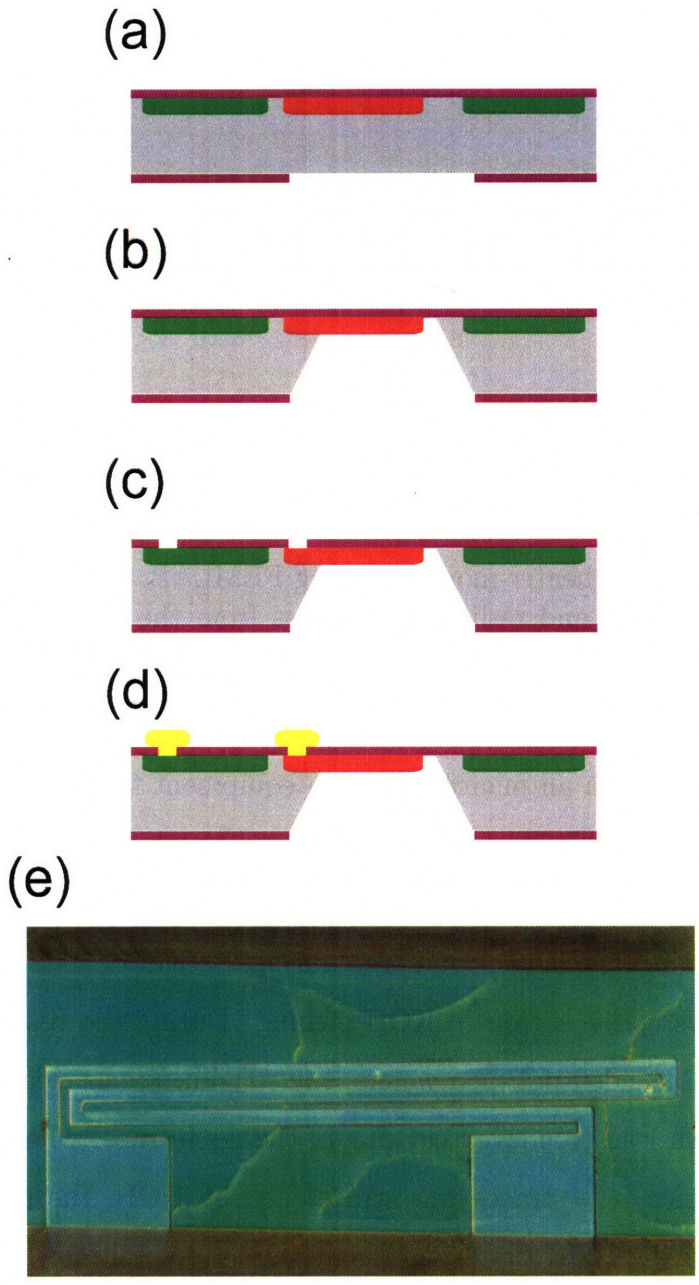

Figure 3–4: Fabrication of suspended p++ heater traces under nitride membrane. (a) Following the annealing of dopants and deposition of nitride, a backside etch exposed bare silicon. (b) KOH etched away exposed silicon anisotropically and terminated at p++ traces and nitride membrane. The good adhesion of p++ silicon to silicon nitride allowed the heaters to stay attached to the nitride membrane. (c) and (d) are standard processing steps to etch the frontside of silicon for sensor and metal contact holes, followed by metal desposition and patterning (e) Optical micrograph of a successfully released serpentine heater trace.

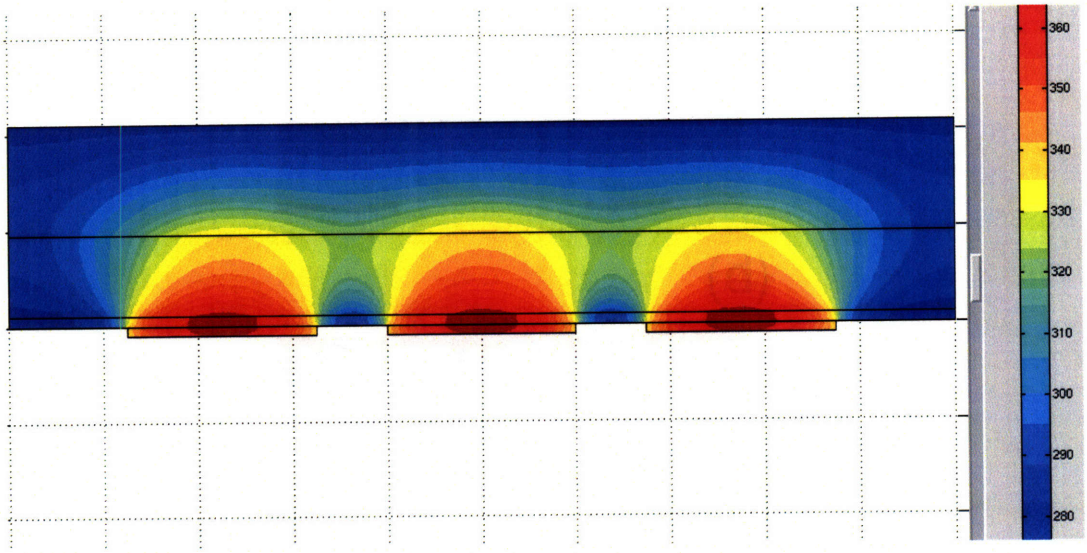

Figure3–5: Suspended heater modeling using FEMLAB. The thermal analysis considered fluid convection and radiative heat loss from the nitride membrane. Fluid flow in the following simulations has been ignored for simplicity.

wafers incompatible with all microfabrication equipment that handles wafers by applying a vacuum to its backside. This can be solved by 'gluing' a piece of handle wafer to the backside of etched wafer, but the procedure is quite finicky and lacks scalability. The most significant issue encountered during fabrication is the low selectivity of undoped silicon vs. p++ silicon to KOH etching. During the KOH backside silicon etch, for non-double-sided-polished wafers, the roughness was clearly preserved during the etch, which lead to uneven clearing of the p++ traces when the etch reached the endpoint. Since p++ traces was still etched by KOH, the parts of the traces that were exposed by KOH first would continue to be etched while one waited for the remainder of the heater traces to clear, resulting in uneven p++ trace thickness. For example, Figure 3–4(e) shows a heater where some undoped silicon remained on the nitride membrane, which could potentially alter the electrical characteristics and temperature uniformity of that particular heating trace drastically. While locally the uniformity can be optimized by slowing the etch rate by lowering the temperature of the bath and monitoring the etch endpoint carefully, globally traces at different locations often reached etch endpoints at significantly different times, hence high

processing yield on a wafer was not possible. However, there exist several options to improve etch selectivity. Diluting the KOH solution with isopropanol could potentially improve the etch selectivity. However, this would greatly have reduced the etch rate and increased the complexity of the etch step. Using TMAH was another option, but it was not clear if it had better etch selectivity than KOH.

Another issue with the device design is the lack of a simple and direct temperature sensing structure for feedback control of the p++ heater traces, leaving power-feedback of the traces the only viable method to maintain certain temperature. However, due to low thermal conductivity, it is also unclear whether the temperature-dependent properties of the heaters will accurately reflect the thermal-profile of the sample in microfluidic sample. Together with yield and robustness issues, alternative on-chip heater fabrication strategies were considered. To overcome these problems, the decision was made to trade-off thermal efficiency for sturdiness and finer control. The goal became to heat up the entire chip uniformly using metal traces that are fabricated in the same step as metal connections to sensors and excitation electrodes. In this design, the fabrication process is identical to that for discrete sensor devices, as there is no need to release any membranes for thermal insulation. Futhermore, this strategy isolates heaters from sensors electrically, making completely independent testing and calibration possible. Temperature sensing metal traces that measure chip-temperature based on temperature coefficient of resistivity can also be fabricated in the same step for in-situ temperature feedback control. The calibration and accuracy of the temperature sensing mechanism will be discussed in the next chapter.

3.3 Active Microfluidic Control

The design and integration of active microfluidic control elements to field-effect sensor design is one of the most critical components of the fabrication process that has not been explored for discrete sensor devices. On-chip microfluidic control is important for the following reasons. First, it isolates the PCR channels from contamination by sensor surface-functionalizing agents. Second, sealing of PCR channels prevents content

evaporation when the device is heated during thermocycling. Microfluidic valves can also eliminate the need for off-chip sample selection valve and enable combinatorial reagent preparation on chip. [130]

Many integrated microfluidic valve fabrication techniques have been published in recent years. [131, 132, 133] Of these, the multilayer lithography-based PDMS integrated microfluidic structure contains both valves and channels in the silicone plastic and can be directly bonded to the silicon sensor device. A detailed characterization of the fabrication process can be found in Ref. [129]. Briefly, fluidic layer and valve layer molds are created by coating a silicon wafer with photoresists, and then exposing and developing. The wafers are treated with HMDS to prevent the PDMS from irreversibly bonding to the silicon. To fabricate the elastomeric structure for microfluidics and valves, 80 g of 7 part A: 1 part B RTV (General Electric, Wilton, CT) was cast over the valve mold and baked at 80 °C for 20 minutes. The partially cured elastomer was peeled off the mold and access holes were punched with a 19-guage needle. 20 part A: 1 part B RTV was spin-coated on the fluidic master at 1100 rpm for 40 seconds, and baked in the oven at 80 °C for 15 minutes. The partially cured valve layer was then aligned and bonded to the fluidic layer and baked overnight. The bonded devices were then peeled off the fluidic master, and access ports to the fluid channels were then drilled. To assemble the silicon and elastomer layers, the silicon and elastomer substrates were first rinsed with ethanol, then the surfaces to be bonded were exposed to air plasma for 20 seconds in a Harrick PDC-32G RF plasma cleaner (Harrick Plasma, Ithaca, NY), and finally the two pieces were aligned and bonded shortly after plasma treatment. The bonded device is left in air for 10 minutes before use to strengthen the elastomer-silicon bond. The valves are filled with water before being pressurized by air to prevent gas permeating through the valve membrane and inject bubbles into fluid channels.

While a hybrid double-layered PDMS-silicon device can be directly used for PCR experiments, several concerns remain. The push-down geometry of the PDMS valve demands low aspect ratio channel profile (1:10). This requirement not only increases surface-to-volume ratio leading to increased chance of bimolecular adsorption to chan-

nel sidewall, but also limits the total sample size volume per area when a higher volume is desirable initially for high PCR yield. To solve this problem, a modified PDMS fabrication process that uses multiple fluid channel depths was developed. The fabrication procedure to create a mold for the valve layer remains the same, as do the PDMS assembly and silicon bonding procedures. However, the new process incoporates patterns of different thicknesses on the microfluidic mold to make deep channels for PCR reagents and shallow channels for valves in PDMS. The shallow channels can be sealed completely when a pressure is applied, whereas the deep channels that have rectangular cross sections can be used at locations that do not require valves for larger fluid handling capacity. 10 μm shallow rounded features based on AZP4620 resist were deposited on fluid-layer master as before, and 60 μm rectangular SU-8 50 features had also been added to the mold. In order to prevent streaking during spin-coating, the thinner structure must be deposited and patterned first, followed by spinning and patterning of the thicker resist. However, since AZP4620 resist can be dissolved by the solvent of SU-8 50, a thermal treatment by heating up the patterned AZP4620 resist to 200 °C, which is above its glass transition temperature [134], was necessarily to alter the chemical properties in order to make it insoluble. Subsequently, SU-8 50 photoresist was spun on the wafer, and patterned with respect to AZP-4620 alignment features. The mold was then hard-baked and silanized at identical conditions described previously. The 200 °C bake step rendered the resist feature fragile, however, and rapid cooling of the wafer should be avoided to prevent resist cracking.

3.4 Robust Glass Microfluidics Fabrication

While multilayer microfluidics offers active control of samples on-chip, because the structure is based on PDMS, it is not compatible with acids such as sulfuric acids which are used for sensor surface cleaning procedures [64]. Thus, if an application requires only passive fluidics, it is desirable to employ more robust materials. This section describes the fabrication procedures for the glass-encapsulated field-effect sen-

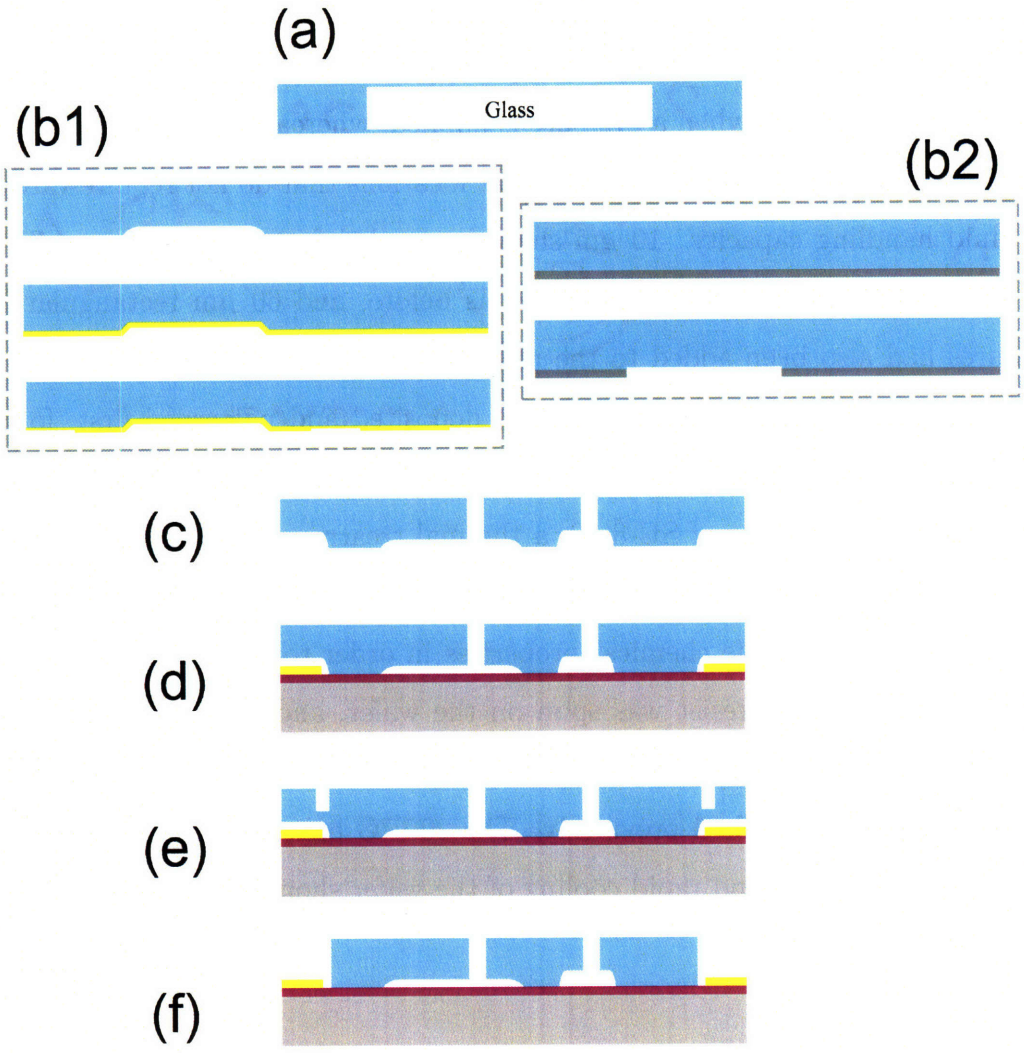

Figure 3–6: Glass encapsulated field-effect sensor fabrication. See text for more details.

sor arrays used for heparin sensing discussed in Chapter 7.

Instead of using gold, platinum which is known for its stability at elevated temperature required for anodic-bonding of glass to silicon is used. Glass patterning begins with blank Pyrex (Corning 7740) glass wafers. Figure 3–6 illustrates the two possible processes to define microfluidic channels in glass. The first strategy attempted used evaporated gold/chrome film as a mask against hydrofluoric acid-based etchant [135] (Figure 3–6(b1)), since standard photoresist would peel off following extended incubation in HF, resulting in significant undercutting. After etching the glass with using a photoresist mask using buffered oxide etchant to define 1 μ deep channels in glass to define recesses over bonded areas that have metal traces, the photoresist is removed from pyrex glass, which subsequently goes through piranha and UV-Ozone clean to ensure a clean dehydrated surface, followed immediately by 100nm Au/20nm Cr deposition. Photolithography is used to define etch regions on metal mask, and aqua regia (3 HNO_3:1 HCl) and commercial chrome etchant CR-7 was used to expose glass area to be etched. The pyrex wafer is submerged in H_2O:HF:HNO_3: (66:14:20) for 40 μm etch. The etch step is completed after stripping the metal mask with aqua regia and CR-7. The second strategy (Figure 3–6(b2)) uses an amorphous silicon mask for 40%HF etchant. 100-nm amorphous silicon was deposited onto the substrate following RCA-clean in an LPCVD furnace. Following photoresist patterning, the exposed amorphous silicon area was dry-etched by SF6 plasma. Glass etching occurred in undiluted HF, and following patterning, the silicon-mask can be dissolved in HNA (8 CH_3COOH: 3 HF: 1 H_2O). After clean pyrex wafers are recovered after channel etch, through-holes are drilled through pyrex ultrasonically (Figure 3–6(c)). The pyrex and silicon device wafers are then bonded anodically (Figure 3–6(d)). Finally, two rounds of diesaw sessions (Figure 3–6(e),(f)), one cutting through glass only to expose metal bond-pads, and another releasing individual dies, complete the fabrication of individual glass-encapsulated field-effect devices.

Both glass microfluidics fabrication processes were successfully carried out, with difficulties encountered mostly during the glass-etching steps. When metal-masking was used, significant undercutting far above the ideal 1:1 undercut:etch-depth ratio

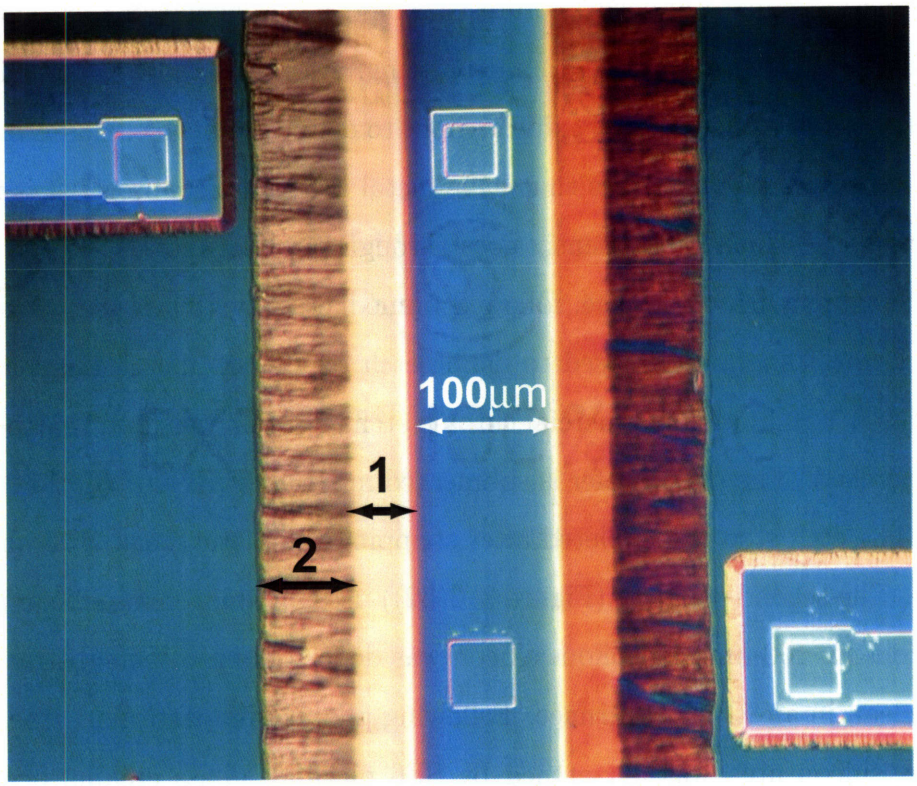

Figure 3–7: Glass-etching using gold/chrome mask. The original exposed area defined by etching of gold/chrome mask is about 100μm wide, and etch depth target is 40μm. Label 1 and 2 show the two regimes of etching, where 2 shows that undercutting became much more significant when a particular etch depth was reached and metal started to delaminate more rapidly.

was observed (Figure 3–7). For an estimated etch-depth of 40 μm, an undercut of more than 100 μm was observed on each side of the channel. The undercut seems to occur in a two-stage process, where the metal served as good mask initially, producing an undercut ratio of about 1.5:1, but beyond certain depth, the metal seemed to delaminate much more rapidly, showing much more undercut per etch depth increment. For example, Figure 3–7 shows that the fluid channel over the sensor and excitation electrode almost merged with the 1μm channels over the metal traces. Therefore, the masking technique is most appropriate for glass etching up to tens of microns. Granted, the etch solution produced channels with smooth sidewalls, and the channel depth was appropriate for measurement-only applications that do not require deep channels, and thus this glass-etching procedure was used to fabricate robust sensor array devices for heparin measurement (Chapter 7). While amorphous silicon-masking achieved 1:1 ideal undercut, the concentrated HF etch produced sidewalls that were inconsistent in smoothness, and depending on etchant stirring condition, the etch rate was found to be feature-size and wafer-location dependent, indicating that etching was limited by etchant transport. Unfortunately, since the etch solution that produced smooth sidewalls for metal-masking is known to attack silicon, it is incompatible with amorphous-silicon masks. The etch uniformity can potentially be improved by using a milder etching solution with surfactant such as BOE at the expense of etch rate. Because the gold-mask process resulted in etches that are more uniform across the entire wafer, hence higher device yield, the technique was chosen for making field-effect heparin sensor arrays.

3.5 Integrated Device Design

Figure 3–8 shows the final device design, which consists of a PDMS microfluidic layer with integrated valve bonded to a silicon field-effect sensor chip. The device consists of two subunits (field-effect sensors and PCR thermocycler) that are independently functional. The device is designed to carry out end-point detection of PCR product: the sample is thermocycled in the PCR channel which is isolated by on-chip valves,

and the electronic sensor can be functionalized at the same time. The channel content is then flowed through the sensor to analyze product concentration. On-chip temperature control and sensing are accomplished by metal traces located outside of the channels along the edges of the device. The overall dimension of the device is 23 mm $\times$ 10.3 mm $\times$ $\sim$5 mm.

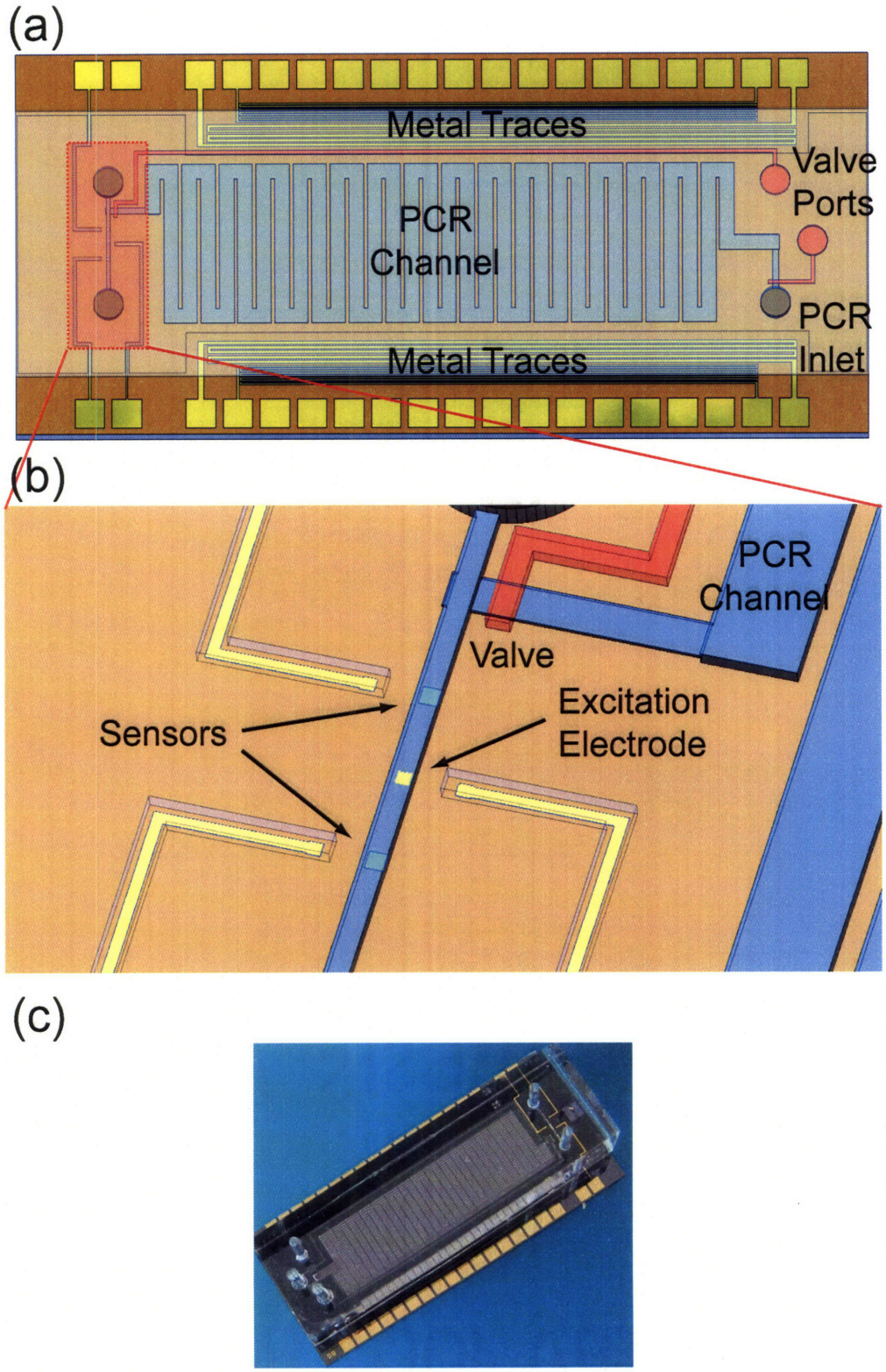

Figure3–8: Layout of integrated device. (a) Top view of device, drawn to scale. (b) Close-up view of the sensor region. (c) Photograph of an integrated device.

Chapter 4

Characterization

4.1 Electronic Sensor Characterization

The electrical characteristic of EIS sensing system can be modeled as a capacitor in parallel with a resistor with an overall impedance magnitude of $|Z_{\text{EIS}}|$. A purely AC signal with an amplitude of V_{AC} is applied to the metal pad connected to the excitation electrode, while a DC bias V_{bias} is applied on the metal pad leading to the field-effect sensor. Therefore the effective input signal on the EIS system is:

$$V_{\text{input}}(t) = V_{\text{AC}} \cos(\omega t) - V_{\text{bias}} \tag{4.1}$$

In an ideal system with no leakage current through EIS structure, the resulting current through the system will also be an AC sinusoid, and this current is amplified by a current amplifier (Keithley 428, Keithley Instruments, Cleveland, Ohio) with a transimpedance gain factor G_{amp} to produce an amplifier output voltage v_{amp}:

$$V_{\text{amp}}(t) = \frac{G_{\text{amp}}}{|Z_{\text{EIS}}|} V_{\text{AC}} \cos(\omega t + \Phi) \tag{4.2}$$

The output of a current amplifier signal is then connected to a lock-in amplifier, which uses a reference signal from the AC function generator to convert the current amplifier signal to a DC signal of which the level can be adjusted with a DC offset:

$$V_{\text{lock-in}}(t) = \frac{G_{\text{lock-in}} G_{\text{amp}}}{|Z_{\text{EIS}}|} V_{\text{AC}} - V_{\text{offset}} \tag{4.3}$$

As discussed in Section 2.2, the output of the amplifier can be converted to a relative surface potential value by applying a step change to the sensor bias and measuring the resulting change in output of the lock-in amplifier i.e. $\frac{\Delta V_{\text{lock-in}}}{\Delta V_{\text{bias}}}$. By identifying a range of bias value where this value is approximately constant, the relative change in surface potential, or $\Delta\zeta$, can then be approximated as the difference in measured lock-in amplifier output divided by this calibration ratio.

The pH sensitivity of sensors has also been characterized. The response of EIS structure to variation in pH has been explained by a site-dissociation-site-binding model of the electrolyte-oxide interface. [136] In this model, the oxide surface is assumed to contain amphoteric groups S-OH, which can take or release protons, resulting in alteration of surface charge due to variations in pH condition, thus changing the surface potential. In this work, the pH response of the sensor in the absence of ionic strength effects was tested with injections of 10 mM phosphate-citrate buffers with same ionic strength but different pH. Figures 4–1(a) and (b) show pH measurements over a wide range and over a narrower range at higher resolution. In these measurements, a continuous flow of buffer with pH 7.0 was used, and an autosampler was used to inject known volumes of samples without disturbing the flow condition.

Both plots show that the response of sensor to different pH values is approximately linear in the range of pH 2.2 to pH 7.8. In addition, given a noise level with standard deviation on the order of 10 μV, sensitivity of up to 0.00013 pH unit can potentially be resolved. The almost linear pH response, however, contrasted with the parabolic curve profile reported in literature for silicon dioxide-based EIS sensors. [137] In particular, it has been reported that pH sensitivity of the device decreases near the point of zero charge of the dielectric film, which is around pH 2 for SiO_2 film. However, since the dielectric used in this study is a native oxide layer whose chemical properties may differ from that of a silicon dioxide film with defined thickness, a direct comparison is not necessarily appropriate. In addition, a slope of 25 mV/pH unit was fitted for the

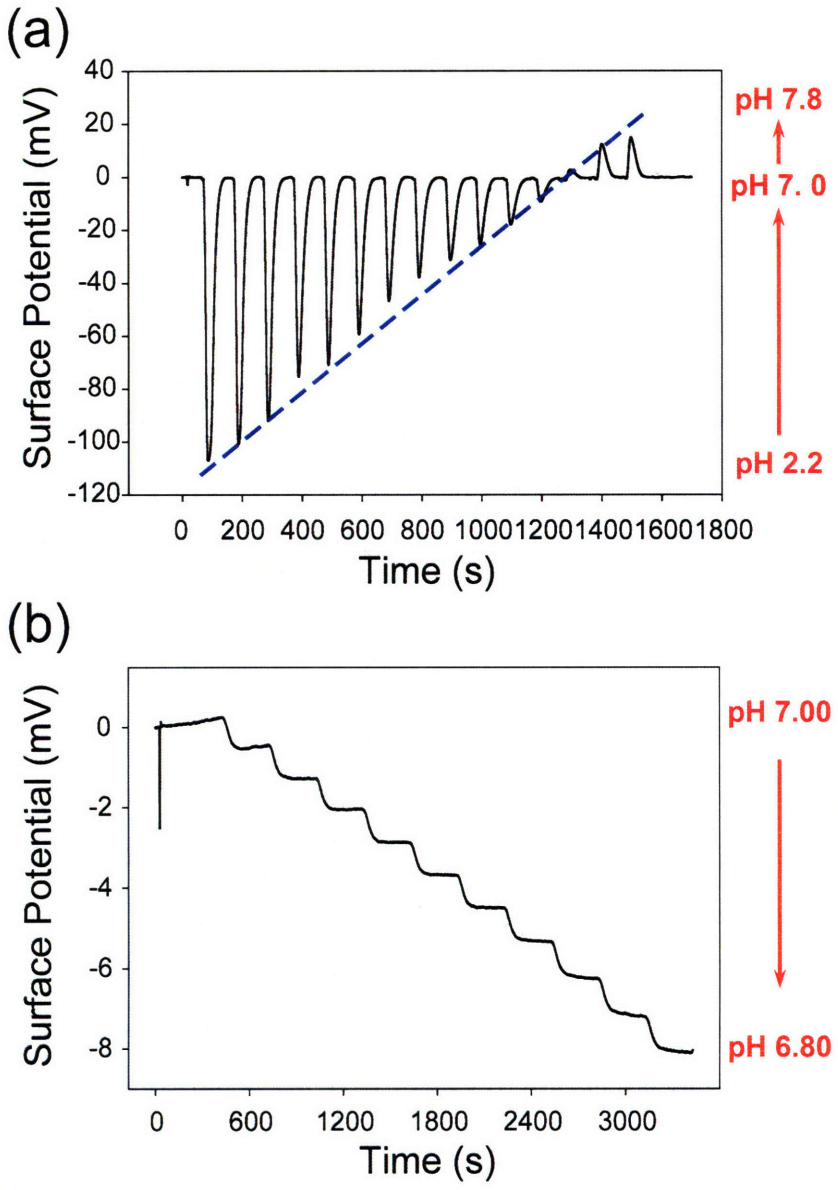

Figure4–1: pH response of field-effect sensor. (a) pH response of field-effect sensor to injections pH 2.2 to pH 7.8 phosphate citrate buffer. Samples were injected increments of pH 0.4, and a constant flow of pH 7.0 buffer was used as baseline. An imaginary dotted line outlines the trend between sensor signal and pH values. (b) Sensor response to pH values between pH 6.8 and pH 7.0 injected in steps of pH 0.2.

data, a value which is within the 25 - 48 mV/pH range reported in the literature. [138] An acid treatment following the HF treatment that increases surface silanol group density could potentially be used to increase the pH sensitivity of the device. [139]

4.2 On-chip Heater Calibration

Three methods have been use to calibrate the temperature of the device: thermochromic liquid crystal, temperature-sensitive fluorescent dye, and resistance measurement of metal traces on-chip.

4.2.1 Thermochromic Liquid Crystal Measurement

Imaging of thermochromic liquid crystals (TLC) was the first approach used to monitor the temperature of microfluidic channel. Two types of thermochromic crystals: R90C5W and R38C5W, were purchased from Hallcrest, Glenview, and have red-start temperature at 90 °C and 38 °C, respectively. Since the crystals have a 5°C bandwidth, they turn blue at 95 °C and 43 °C, respectively, and according to product specification, a 5 °C bandwidth implies the crystal will also become green at 1 °C above their red-start temperature. Figure 4–2 demonstrates temperature measurement inside sections of a microfluidic channel heated by suspended microheaters. The crystals are reported to have temperature measurement error of less than 1% of the TLC effective temperature range [140], and thus these crystals can potentially yield temperature measurement accurate to within 1 °C at the red-start temperature. However, a major limitation of the crystal is that it does not yield any information below the red-start temperature and offers poor temperature resolution above green-start temperature. In addition, the crystal sizes range between 5 and 15 μm, and come in as concentrated slurry, which easily clogs microfluidic channels with depth of comparable dimensions. In practice, it has also been found that they tend to melt and leave behind residue at elevated temperature, potentially contaminating the microfluidic channels and adversely affecting PCR performance. Therefore, while these crystals are excellent for visualizing temperature uniformity at the specified red-start temper-

ature, a feature which was eventually used to prove the accuracy of other methods of calibration, they did not offer the capability for measurement of temperature over a continuous range which is required for a primary temperature calibration method.

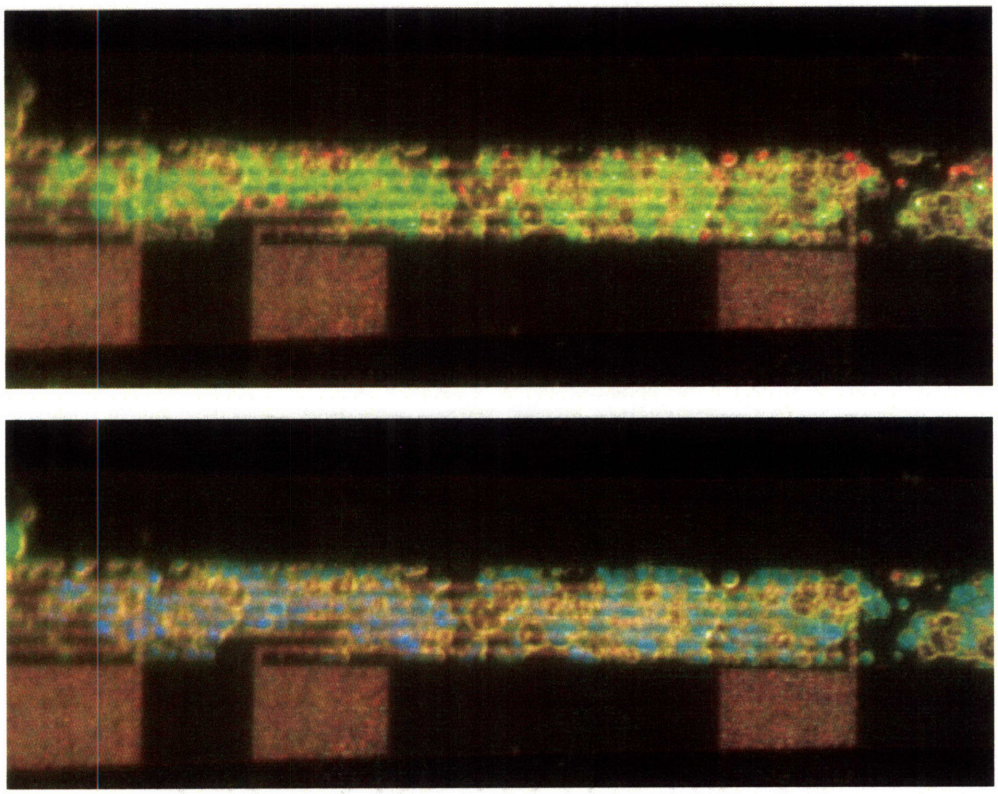

Figure 4–2: Temperature measurement using thermochromic liquid crystals. Top and bottom images are photos of microchannels with different voltages applied to the suspended heaters under the nitride membrane. Images courtesy of T. Loh.

4.2.2 Heater calibration using Fluorescent Dyes

Temperature measurement using temperature-sensitive fluorescent dyes is a powerful method to obtain spatial temperature distribution in microfluidic channels. [141] The fluorescence intensity of the temperature-sensitive dye varies continuously over a wide range of temperature. The dye can be dissolved in buffer, providing a calibration medium that resembles the reagent which will undergo heat treatment in thermal characteristics. Also, the dissolved dye will not clog the channel, unlike thermochromic liquid crystals. For these reasons, this technique has been chosen

to monitor the temperature of microfluidic channel that are heated by suspended conductive traces. [129]

The particular implementation of fluorescent dye calibration method uses D-1824 Dextran-rhodamine B Conjugate probe purchased from Molecular Probes Inc., Carlsbad, California. Because channel heights can vary between devices, and the channels do not necessarily have a rectangular profile, a ratiometric approach that compares the pixel intensity at a particular location at certain temperature to the intensity at the same location at some reference temperature acquired previously yields a ratio that can be quantitatively converted to a temperature based on calibration data. The calibration data were acquired by heating an entire device on a hotplate and measuring the resulting fluorescent intensity at temperatures of interest. The ratios of pixels are then averaged spatially, and plotting the intensity ratio with respect to temperature reveals a relation that can be fitted by a second order polynomial i.e.:

$$I_{\text{ratio}}(x, y, T) = \frac{I(x, y, T)}{I(x, y, T_0)} = \mathrm{C}_1 T^2 + \mathrm{C}_2 T + \mathrm{C}_3 \tag{4.4}$$

where C_1, C_2, and C_3 are best-fitted parameters derived from calibration data, and t_0 is the reference temperature on which the calibration data were based. By implementing various image stabilizing algorithm to ensure the analyzed image does not shift spatially during image acquisition, accuracy to within 5 °C can be achieved for the actual experimental setup. During the actual temperature measurement step, a matlab-based software that communicates with a CCD camera which continuously obtain snapshots of the channel fluorescence also performs real-time temperature conversion and outputs spatial temperature information. An example of temperature-map acquired during operation of a suspended heater is shown in Figure 4–3.

Once the technique was developed, it was applied to the calibration of heaters and immediately yielded important information. For example, only 30 mW was required to heat boil liquid in channel on top of a heater, and thermal isolation ensured that the elevated temperature remain confined to less than 100 microns away from the edges of the heaters. The heaters can also transition between the high and low end

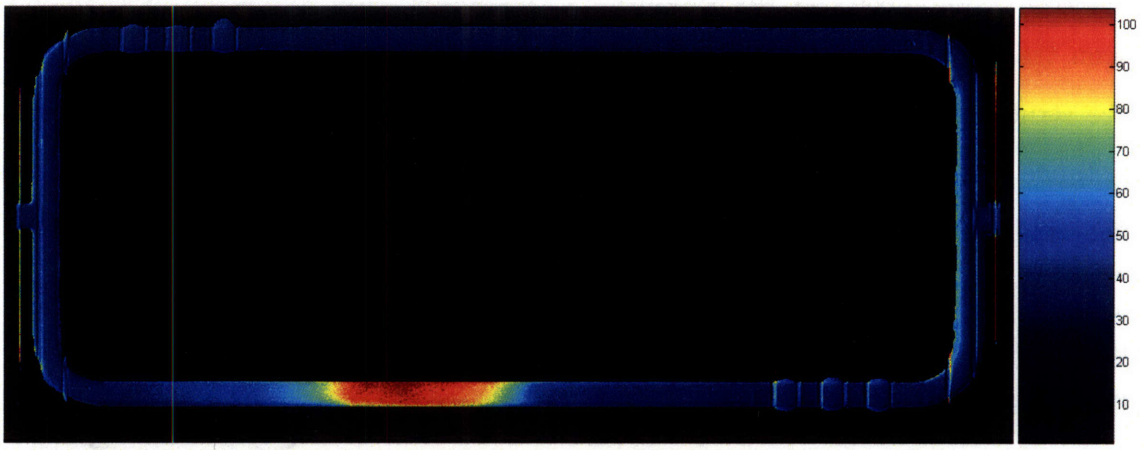

Figure 4–3: 2D temperature map of microfluidic channel obtained using custom matlab software and a rhodamine dye. One heater at the bottom of the channel was turned on when during the image acquisition. Image adopted from [129].

of PCR temperatures within seconds, a property enabled by the low thermal-mass of the system. This study, however, also exposed flaws of the original 3-heater design for spatial thermocycling; in the initial design, the heaters were sufficiently far apart that two temperature zones do not sufficiently overlap to ensure a smooth spatial temperature transition, which is critical for a well-designed spatial-PCR system. Also, it was realized that it is difficult to fabricate heaters of uniform thicknesses even on the same die with the KOH release process, and frequently a certain area of a single heater would produce more heat than another, leading to temperature variation within a single temperature zone. Problems associated with the temperature sensing method were also encountered. In the case of PDMS-silicon chip, the device frequently became cloudy due to content evaporation. Also, while the solution never clogged the PDMS channel, it is possible that the dye could remain bound to the microfluidic channel and inhibit PCR.

4.2.3 Metal Resistive Temperature sensors

One aspect discovered during the testing of suspended heaters that makes the open-loop control very difficult is drift. Therefore, practically, it is most desirable to have a temperature sensing element on-chip located at a position that can accurately reflect

the actual temperature of the channel for closed-loop heater control. Conductive silicon traces have a negative coefficient of resistivity, and a suspended conductive trace structure could also be used for temperature measurement by monitoring its resistance. However, given the excellent thermal insulation property of silicon nitride membrane, unless a temperature sensing trace is placed directly above or under a corresponding heater trace, an accurate thermal profile cannot be obtained, but fabricating such a structure requires introducing additional steps to an already complicated fabrication process that has limited yield.

To overcome these issues, the decision was made to trade-off thermal efficiency for sturdiness and finer control. The KOH etch step was removed from the process, making the process flow identical to that of the original discrete sensor devices, and heaters were redesigned to heat up the entire chip uniformly. Heaters now consist exclusively of metal traces on silicon nitride and make no contact to the bulk silicon, therefore completely isolating the heaters from sensors electrically. The electrical isolation is important for usability, since the resistance of the original suspended p++ trace heater design depends on n++ ground-plane bias condition, a parameter that could be changed between experiments. Thus a complete calibration of suspended heaters requires measurement of heater resistance values with respect to different bias conditions.

Temperature sensing gold traces that make use of gold's temperature coefficient of resistivity have been added on-chip for in-situ feedback control. The temperature measurement method is quite straightforward to calibrate; the entire device was simply placed in a convective oven and the resistance of the temperature sensor traces were recorded at different temperatures, and analysis revealed a linear dependence at the range of temperatures required for PCR Figure 4–4. Subsequent experiments using thermochromic liquid crystals, R90C5W and R38C5W, showed that even though the traces are outside of channels, the high thermal conductivity of silicon substrate spread the heat from heaters uniformly, the temperature measured by conductive traces and crystals inside channels were identical.

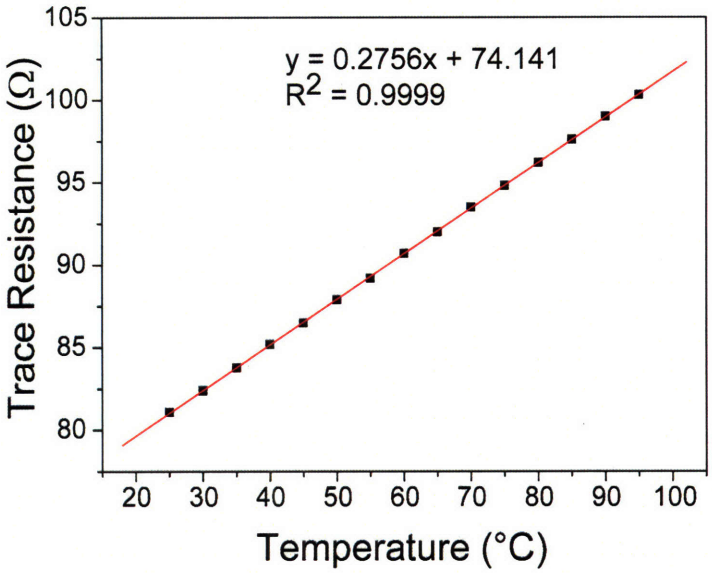

Figure 4–4: Calibration data for metal resistive temperature sensor. Linear regression was used to fit the data.

4.2.4 On-chip Temporal Thermocycling

A temperature controller software was written in Labview. The system implements on-off control of heaters based on the acquired resistance value acquired from the temperature sensing metal traces. To maximize the temperature ramp rate in order to speed up PCR reactions, the following strategies are employed. First, the silicon/PDMS hybrid device is glued on the PCB package with thermally insulating double-sided polyurethane tape, in order to minimize heat loss through conduction and speed up heating. Second, a hole is drilled through the backside of the PCB package to enable nitrogen-gun forced convective cooling. A custom circuit board was made to control solenoid valves (Lee Company, Westbrook, CT) to blow 15 psi compressed air on the backside of the device to accelerate cooling. Thanks to these strategies, the devices achieve heating and cooling rates exceeding 50 °C/s, more than an order of magnitude faster than typical thermocyclers with on average 2 °C/s ramp rates. During temperature transition, the entire chip heats or cools uniformly, whereas benchtop systems often require tens of seconds for the content PCR tube to equilibrate in temperature. Moreover, the package is robust since it does not require

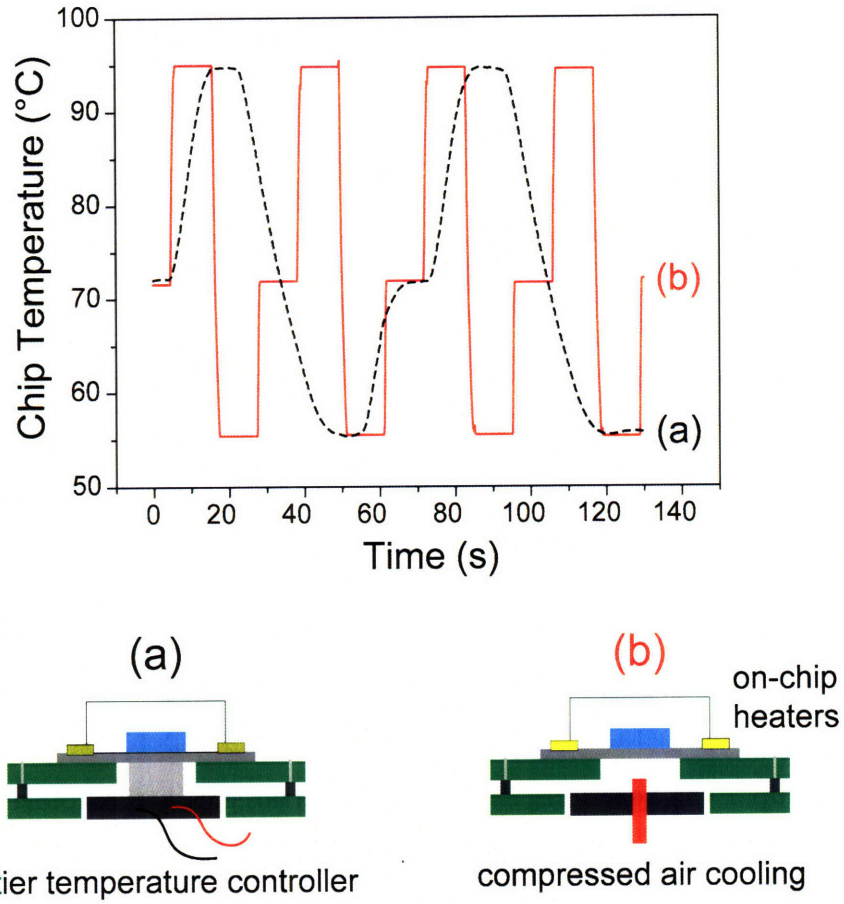

Figure4–5: Performance comparison of on-chip and off-chip temperature controllers running the same PCR protocol of 95 °C for 10 s, 55 °C for 10 s, and 72 °C for 10 s. Off-chip heating uses an external thermoelectric stage pressed against the backside of the device (black solid trace a), and on-chip heater configuration consists of integrated metal resistive heater and temperature sensors with compressed air cooling (red dotted trace b).

the various etching techniques many fast chip-based thermocyclers used for optimal thermal performance. Temperature calibration is straightforward and done by placing the entire package in a convection oven and measuring the temperature sensor trace resistance at various temperatures. Custom Labview software was written to control the temperature of the chip with 0.1 °C resolution, 0.4 °C stability, and less than 1 °C variation across the chip, as verified by thermochromic liquid crystals.

For comparison, an off-chip temperature controller setup has also been implemented. Off-chip temperature control was achieved using a thermoelectric module (mounted against the chip) powered by a pulse-width-modulated PID controller (model 5C7-378, McShane Inc., Medina, Ohio). A custom Labview program was implemented for thermocycling applications. Although the temperature ramp rate is slower than that of the integrated heaters, the off-chip configuration eliminates the need to recalibrate the temperature sensing traces for each new device that is used. Figure 4–5 demonstrates a performance comparison of on-chip and off-chip thermocycling configurations carrying out the same PCR protocol but requiring different temperature transition times.

4.3 On-chip Microfluidic Control Characterization

The performance of on-chip active microfluidic control was evaluated in terms of the fluid sample switching speed and sharpness of injection peaks. In any fluidic system designed for sample selection, there is a certain passage volume from the sample leading to the location of interest, in this case the sensor, and this can greatly affect the measured sample concentration profile. This phenomenon is best described by a fluid dispersion theory developed by Tayloer [142]: When a fluid flows through a tube, a velocity profile develops. This profile is not uniform over the cross-section of the tube; the laminar profile for Newtonian fluids has a parabolic velocity distribution. When there is a plug of liquid sample in a continuous flow of running buffer, the flow will cause this plug to disperse and induce radial composition gradients. This leads to diffusive fluxes at the front and back sides of the plug. If the radial diffusive

fluxes are roughly of the same order of magnitude as the convective axial fluxes, which occurs when either the axial velocity is very low, or when the radial distances are very small, then diffusion tends to keep the plug together. Through the combined action of convection and diffusion, the plug will leave the tube as a broadened plug with a concentration lower than that of the original injected sample. In most circumstances, especially for sensing applications, it is desirable to minimize this sample dilution effect, a phenomenon that is determined by the design of microfluidics.

In this study, both on-chip and off-chip sample selection mechanisms have been employed, and detailed protocols of their uses will be discussed in detail in Chapter 6. A 'T' junction exists on the device, with one path leading to sensors, one connected to a 'sensor channel input' port, and another interfacing with PCR channel. The external sample selection valve employed in this work is a nanopeak selection valve with 6 inputs and 1 output (Upchurch Scientific, Oak Harbor, WA), which is connected to the inlet of the sensor channel. There is an integrated valve which can be programmed to isolate the sensor channel from PCR channel. While there is no active on-chip valve to shut off the sensor channel input port connected to the external selection valve, thus a reverse flow into the valve is possible when injecting sample through the PCR channel. However, in practice the 'upstream' flow path resistance is significantly greater than that of the downstream path leading to the sensors, so approximately all the injected content flows through the sensors.

The following on-chip and off-chip selection mechanisms were tested. For off-chip sample selection, PCR channel valves were shut, and the external valves were used to choose from two samples in vials pressurized by nitrogen. Evaluation of on-chip sample selection performance includes filling the PCR channel and the tube connecting to the input port of sensor channel with different buffers. The on-chip valves were not used, as it induced other effects which will be discussed in Chapter 6, and therefore only 'passive valves' which resulted in differences in fluid pathway resistances prevented flow in the reverse directions. 10 mM phosphate citrate buffer and PCR buffer (20 mM KCl, 2 mM $MgCl_2$, and 10 mM Tris-HCl pH 8.3) were used. Figure 4–6shows that the on-chip valve both reduced sample injection delay due to the passage

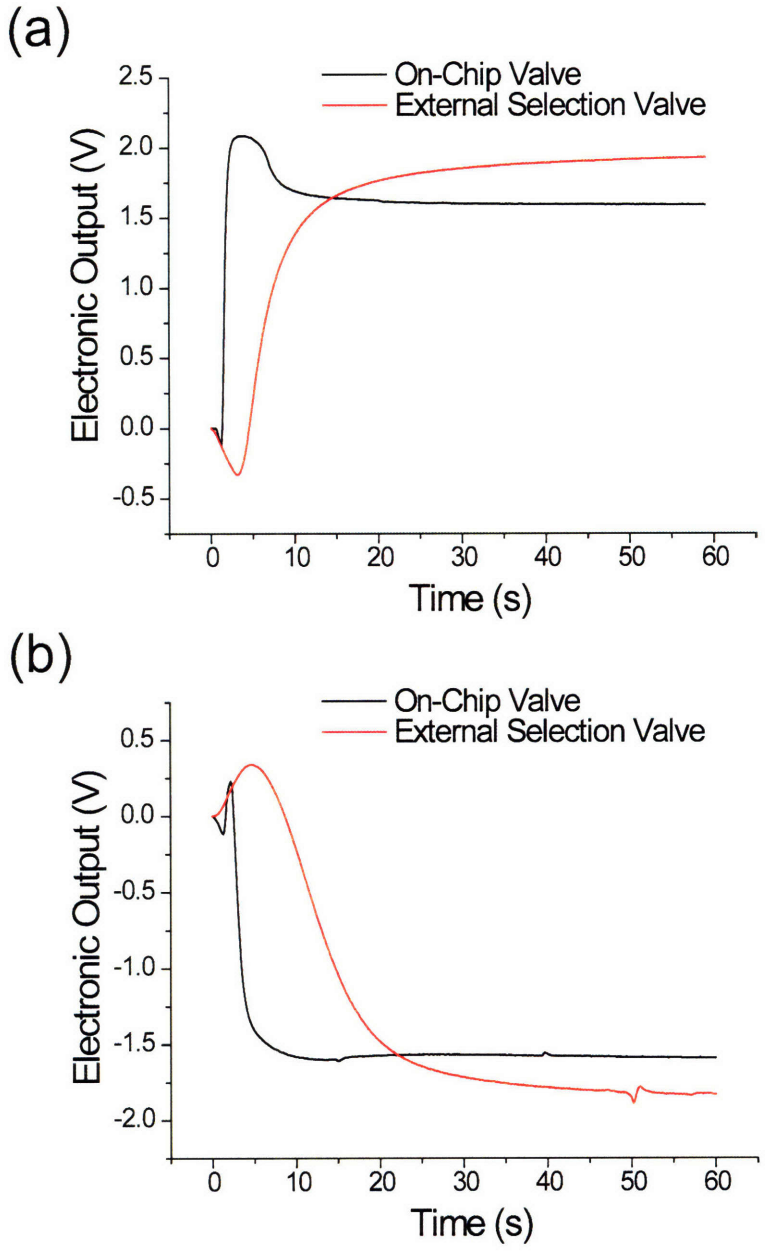

Figure4–6: Sample-switching performances of on-chip and off-chip selection valves. (a) Switching from PCR buffer to phosphate citrate buffer at time = 0 s. (b) Switching from phosphate citrate buffer to PCR buffer at time = 0 s.

volume and maintained a sharper injection peak, suggesting less Taylor dispersion. This study therefore confirms the advantage of moving the sample selection mechanisms as close to the sensor as possible, although one must also consider whether the mechanical and electrical disturbances due to sample switching can cause artifacts on sensors and obscure the measurements.

Chapter 5

PCR Sensing

This chapter explores the feasibility of label-free electronic quantification of unprocessed PCR product using layer-by-layer assembly of polyelectrolyte multilayers. First, the properties of electronic readout for DNA-PLL multilayer depositions will be examined. Second, a series of control experiments measuring the individual components of PCR reagents will establish the basis of this quantification approach. Finally, the use of sensor to monitor product concentration at various stages of PCR will be demonstrated, and a performance comparison to existing real-time optical measurement methods will be presented.

5.1 Electronic sensing of multilayer film assembly

After establishing the EIS structure's pH sensitivity in the previous chapter, the ability of the device to carry out biomolecular measurement was tested by using the sensor to monitor the formation of polyelectrolyte multilayers through alternating depositions of poly-L-lysine (PLL), a positively charged polypeptide, and DNA, which carries two negative charges per base pair. The thickness of polyelectrolyte multilayers is known to increase with alternating depositions of oppositely charged species due to electrostatic associations, thus yielding rising signals when measuring their mass or thickness. As discussed in Section 2.1, polyelectrolyte multilayer deposition on the intrinsically negatively charged field-effect sensor surface reveals markedly different

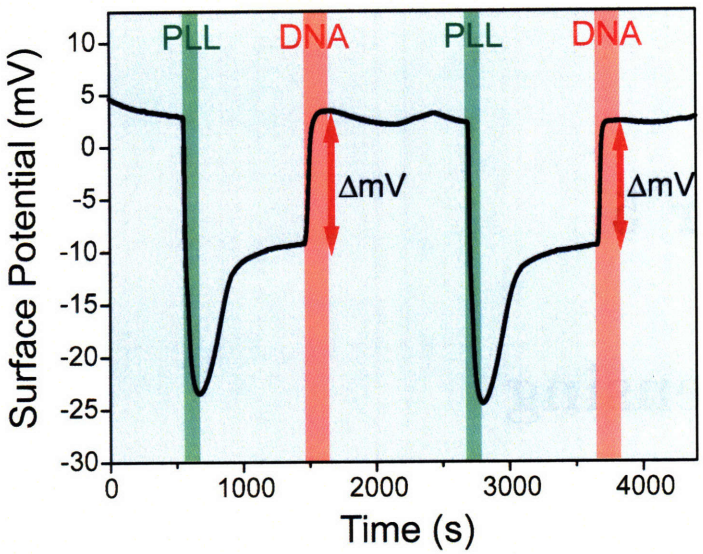

Figure5–1: Electronic detection of DNA-poly-L-lysine multilayer depositions. PLL was introduced to the sensor for 3 minutes (green window) followed by 10 min rinsing with buffer, after which DNA was introduced for 5 min (red) followed by a 15 min wash.

behavior; the deposition of a positively charged polymer consistently results in a decrease of signal and the subsequent adsorption of a negatively charged species results in an increase. Figure 5–1 shows the sensor response to two consecutive rounds of alternating PLL and DNA injections within an experiment where 18 dielectric layers were deposited. The cyclical pattern was observed without noticeable degradation in the amplitude of the equilibrated signal, where 13mV was recorded for both the first and final layer of DNA deposition, indicating that the overcompensated surface charge at the top layer is effectively measured by the field-effect sensor. In addition, even though the technique measures the overall series impedance of the electrical pathway including that of the multilayer film, because the signal amplitude does not decay with increasing multilayer thickness, the observation indicates that the sensor is primarily sensitive to changes in surface potential rather than that in the dielectric properties of the surface, which is consistent with the theoretical calculations in Section 2.4. This feature allows one to perform multiple rounds of DNA measurements by resetting the baseline signal by re-depositing PLL onto the surface. At the same time, the

additive surface regeneration process ensures that the surface is saturated by positive charges and the binding capacity does not degrade for multiple DNA analyses. After multilayer deposition, cleaning with piranha acid can restore the sensor to its initial state without degrading sensitivity. This cleaning procedure has been repeated on a device which was reused for more than a month.

One notable feature observed during the PLL disposition step is the characteristic overshoot in surface potential during the injection of the PLL solution. Unlike the binding of DNA, which results in a relatively stable surface potential during rinsing, flushing the sensor with buffer after introducing PLL results in a significant increase in signal and requires additional time in order to reach equilibrium. Similar observations were also made when we constructed multilayers of poly-L-glutamic acid (PG), the negatively charged analogue to PLL, and PLL. In contrast, studies which used surface plasmon resonance spectrometry monitor the multilayer assembly process does not reveal a sharp change in the signal upon rinsing, suggesting that the polymer did not desorb rapidly due to flushing. [143, 144] This phenomenon cannot be caused by conductivity change in the solution, since dissolved polyelectrolyte should increase the conductivity in the solution, which would lead to an increase in sensor signal when PLL was in solution, but instead the signal was higher after switching back to rinse buffer. It is likely that there is a rearrangement of the polymer or ionic distribution in the film which in turn changes the potential profile at the film-electrolyte interface. However, recent studies of the kinetics of PLL/hyaluronan (HA) multilayer formation reveal that PLL in the film diffuses into the film away from the electrolyte-solution interface during the PLL solution injection, and diffuses back to the surface during HA injection, a phenomenon that could explain the exponential increase growth in film thickness in this particular system. [145] Thus, it is also possible that changes taking place in the bulk of the multilayer film in addition to those in the multilayer-electrolyte interface contributes to the signal overshoot.

To further investigate this phenomenon, the kinetics of the overshoot was studied. In particular, the goal was to determine whether the presence of diluted PLL in solution due to Taylor-dispersion sample broadening effect at the tail-end of the sample

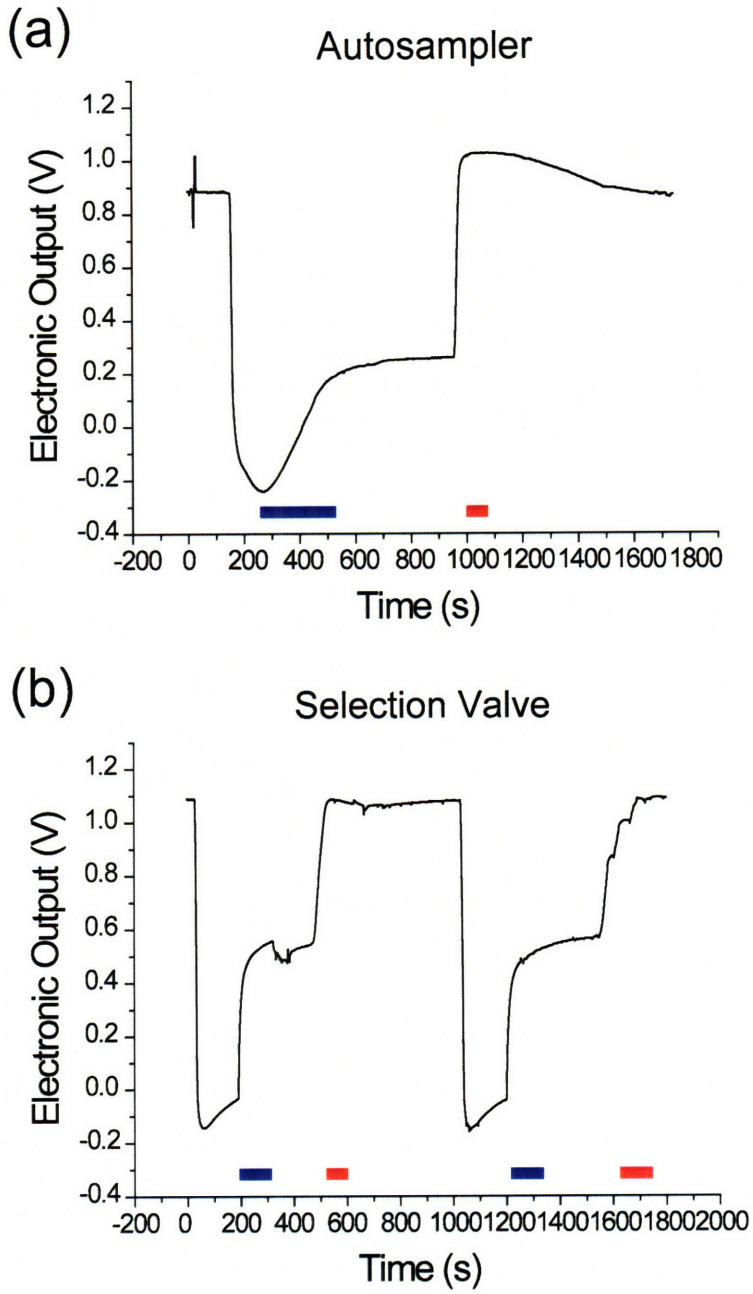

Figure 5–2: Investigation of post-PLL injection overshoot effect using different microfluidic sample delivery systems. PLL-DNA multilayer deposition was measured electronically using two sample delivery systems: (a) autosampler and (b) selection valve, the latter of which has less sample dispersion effect on the tail end of sample plugs. The blue lines outline the post-PLL injection recovery times, and the red lines show the time the sensor took to reach a full response after DNA injection.

plug could have direct influence on the recovery time of the overshoot response, or there was some slow rearrangement process that happened in the film independent of the buffer solution composition. This was achieved by comparing the results using two microfluidic sample delivery systems: an autosampler (Hitachi High Technologies America), which has significant sample dilution effect at the end of a sample plug, and a selection valve (Upchurch Scientific) which has lower passage volume. If the recovery time was reduced by using a system with faster sample switching time i.e. PLL was removed from solution more quickly, then the response is related to presence of PLL in solution. This is in fact what was observed in the comparative study (Figure 5–2), where the overshoot recovery time was reduced approximately 10-fold by using a sample selection system with lower passage volume, indicating the presence of PLL in solution seems to make surface potential more 'positive,' even though as mentioned in the previous paragraph studies have shown that there is no apparent multilayer film thickness reduction following post-PLL injection buffer rinse. Interestingly, the results also show that the time required to reach a full sensor response was not improved by using a microfluidic system with lower passage volume.

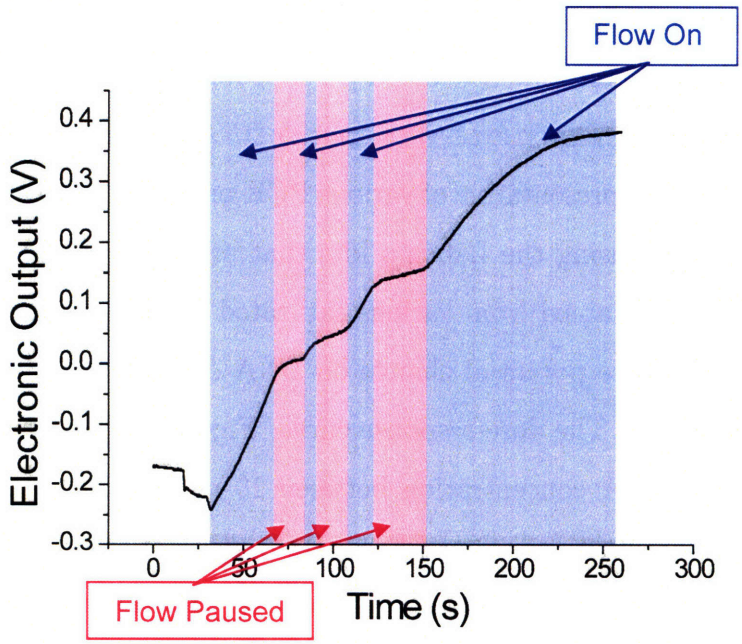

Figure 5–3: Flow rate dependence of DNA signal kinetics. Flow of DNA sample through PCR buffer was turned on and off intermittently until the response saturated.

Also studied was the kinetics of DNA response in relation to sample flow rate. A pressure driven flow to inject DNA, and the pressure was turned on and off intermittently during sample injection. Because there was no significant pressure build-up in the microfluidic system, the flow could be assumed to start and stop with instantaneously following a switch in pressure. The result is shown in Figure 5–3. When fluid flow was paused, the slope of the signal was significantly reduced, and a subsequent restoration of flow would increase the slope again. This suggests the possibility of DNA depletion in channel near the sensor area due to irreversible deposition of DNA onto the surface, and a flow must be used to replenish DNA for the signal to continue rising. However, an increase in flow rate did not have significant impact on the kinetics of DNA response. While each round of DNA deposition at the same concentration produced signal of almost identical amplitudes, the slope of the signal does seem to decrease gradually with increasing number of layers. This effect was also observed and investigated in detail in Reference [81].

5.2 PCR reagents sensitivity characterization

The sensor's response to DNA concentrations in the range relevant to PCR conditions was tested in order to determine if it could be used for PCR analysis. To obtain the DNA mass concentration response of the sensor, a DNA ladder of lengths between 50 bp to 1350 bp which is representative of various PCR product sizes was chosen. It was empirically determined using the Labchip kits that product concentrations between 20 and 50 ng/μL are obtained from various saturated PCR experiments. Therefore, the dependence of surface potential change on DNA concentration between 2.5 and 80 ng/μL was measured. The dose-response curve (Figure 5–4) shows that the device is most sensitive to DNA concentration between 10 ng/μL and 40 ng/μL, a range relevant to PCR quantifications. One noteworthy feature of the electronic multilayer assembly technique is that the response from a DNA injection is independent of the history of prior DNA injections. For example, the dose response data were obtained at no particular order. This makes the sensor amenable to blind sequential quantitation

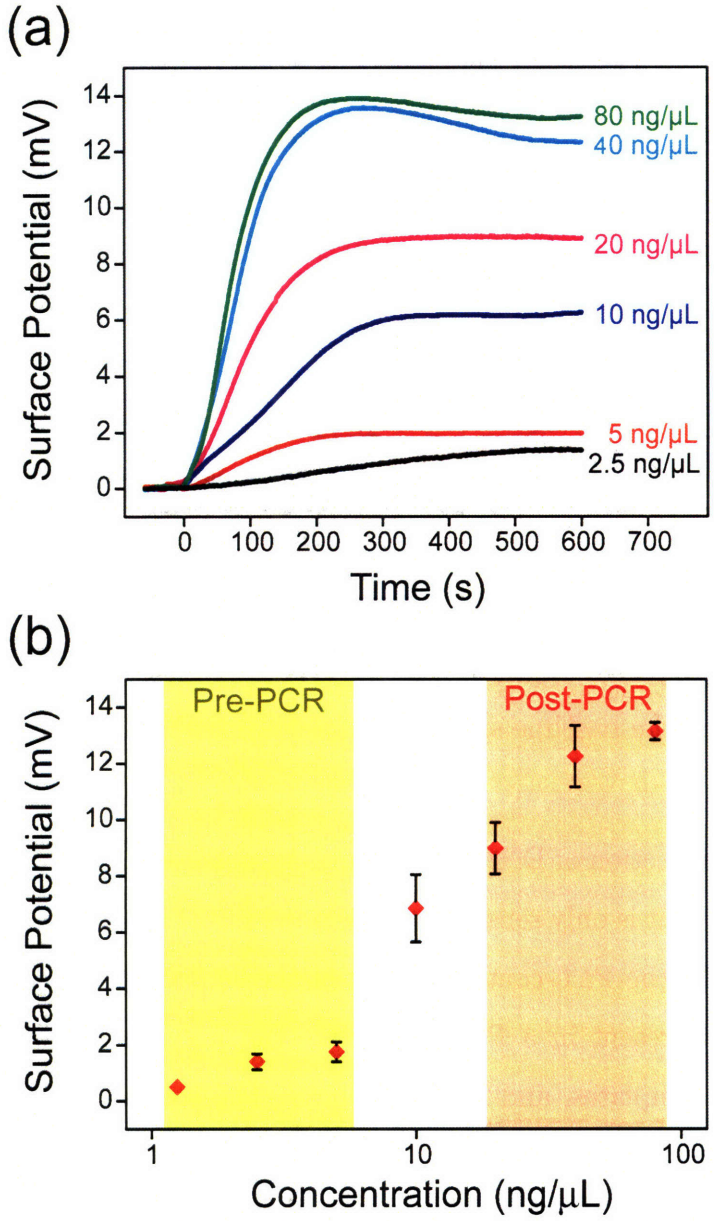

Figure 5–4: DNA concentration response of the electronic sensor.a) DNA ladder (50bp to 1350bp) were injected at various dilutions in the order of increasing concentrations. (b) Steady state response as a function of DNA concentration. The yellow window indicates the typical total concentration of nucleic acid at the start of the PCR reaction including the primers and templates; the red window indicates a range of expected product concentrations at PCR saturation. Error bar represents one standard deviation above and below the average sensor output for multiple injections of a given concentration. Samples were injected in no particular order.

of unknown DNA samples.

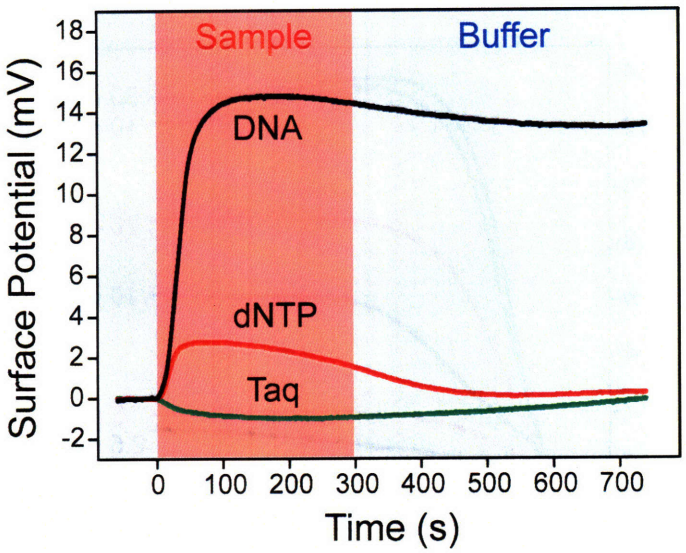

Figure5–5: Sensitivity assessment for individual components in a PCR reaction including DNA (40 ng/μL), dNTP (0.1 mM each), and Taq Polymerase (0.05 U/μL) at concentrations relevant to PCR conditions. Upon rinsing, only DNA yielded consistent changes from the baseline signal.

The electronic detection of DNA/PLL multilayers is useful for PCR product analysis if the measurement is only sensitive to the products of interest in a PCR mixture. To characterize this, the PLL-coated surface of the sensor was exposed to the individual components present in a PCR mixture: Taq polymerase, dNTP, and DNA including primers, templates, and PCR products. The components were introduced at the same concentrations used for PCR in order to quantify their corresponding surface potential response. Taq polymerase decreased the surface potential slightly during its introduction Figure 5–5), but the baseline potential was recovered after subsequent rinsing. The dNTP solution raised the sensor output during injection, but the change was again not permanent. While dNTP has four negative charges per molecule, this result shows that permanent electrostatic adsorption requires stronger interactions between the molecules in solution and the surface in order to prevent elution. In contrast, 40 ng/μL of dsDNA ladder resulted in a clearly resolvable baseline shift.

The types of nucleic acids in a PCR mixture include primers, templates, and products. The sensor's response to each component was characterized at the concentrations used for the PCR experiments. In particular, the sensor's response to 0.4 μM forward and reverse primers, 2 ng/μL genomic DNA (equivalent to 100 ng DNA template in 50 /μL of PCR buffer), and 30 ng/μL purified amplification product yielded average surface potential changes of 1 mV, 1 mV, and 10 mV, respectively. This result indicates that even though the primers and templates in a PCR mixture will produce background signals, the product is expected to contribute most significantly to the overall sensor readout when PCR saturates.

Developing PCR protocols for different targets inevitably involves varying the sizes and concentrations of the reagents and products. To demonstrate the generality of the sensing technique for different PCR conditions, this report provides further characterization of the sensors' response to nucleic acids of different lengths (including dNTP monomers) at a variety of mass concentrations. This provides a foundation for understanding how changing PCR parameters such as primer/dNTP concentrations, and/or final product concentrations can affect the sensor's response. Specifically, the sensor response to dNTP, 20 bp ssDNA, 50 bp DNA ladder (50 - 1000 bp, weighted average length = 222 bp) and 1 kbp (500 - 10,000 bp, average length = 1491 bp) ladder, each at 3.16 ng/μL, 10 ng/μL, 31.6 ng/μL, and 100 ng/μL, have been characterized. The 50 bp ladder and 1 kbp ladder were chosen to represent the low and high ends of average diagnostic PCR product size ranges. This concentration range was selected to represent typical product concentrations between 20 and 100 ng/μL (as verified from various saturated PCR using Labchip kits). Typical primer concentrations of 0.5 μM each and dNTP concentrations of 200 μM each type of nucleotide [146] correspond to a mass concentration of approximately 3 ng/μL and 100 ng/μL, respectively.

Indeed, as shown in Figure 5–6, the signal amplitudes correlate with both the length and concentrations of DNA. Injecting dNTP results in a transient response only (Figure 5–6a). Even though the injection of DNA of different lengths caused a permanent response, as shown in Figure 4b, the response to short 20 bp single-stranded oligonucleotide was weaker compared to those of longer double-stranded

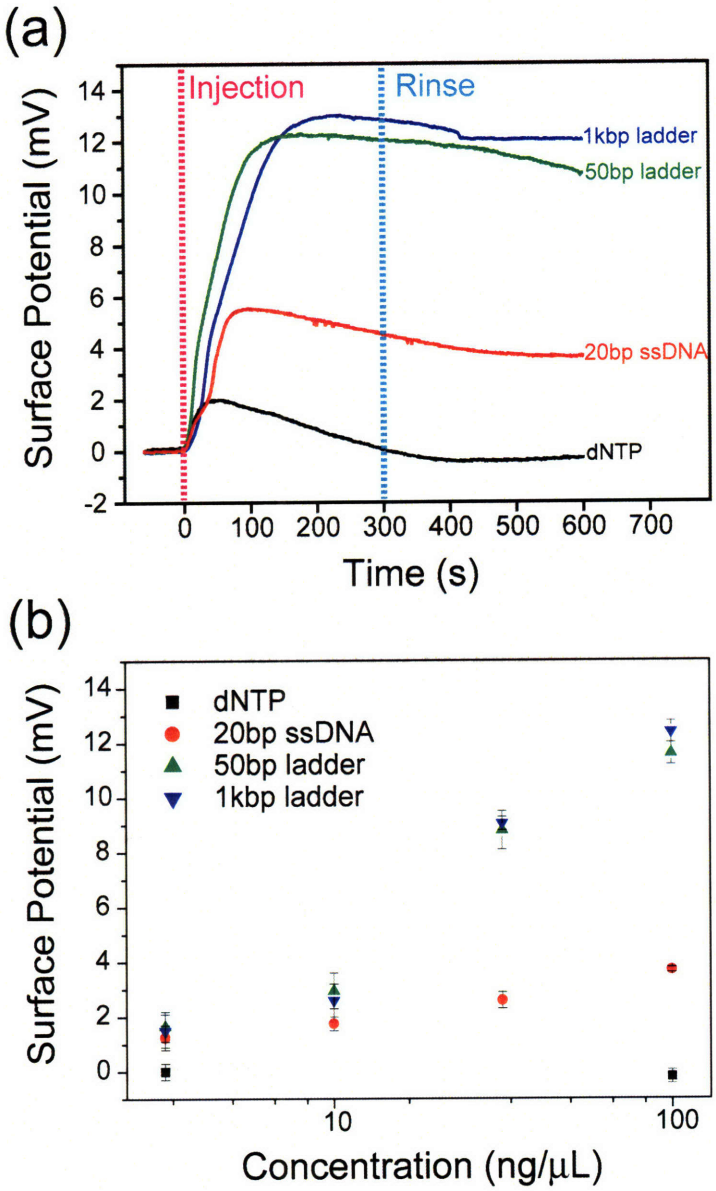

Figure5–6: Characterization of sensor response to different DNA lengths. (a) Time-course measurement of surface potential of dNTP, 20 bp ssDNA, 50 bp dsDNA ladder, and 1 kbp dsDNA ladder at 100 ng/μL. Samples were injected for 5 minutes each (left dotted line) onto a surface coated with PLL, followed by rinsing with buffer (right dotted line). (b) Dose-response curve of nucleic acids of different sizes using the same injection protocols described in (a). Each series of curves was obtained from a unique device using electronic polyelectrolyte multilayer detection technique. To ensure comparability between data, before the dose-response analysis, a control sample of 50 bp ladder at 40 ng/μL was measured, which yielded potential shifts 9.0 $\pm$ 0.2 mV. Each data point is an average of two measurements $\pm$ 1 SD

DNA ladders at the same mass concentrations. To demonstrate consistency among different devices, 40 ng/μL 50bp DNA ladder was injected during each experiment as a control, producing a change in surface potential of 9.0 $\pm$ 0.2 mV. This variability is relatively small compared to the difference of greater than 8 mV observed between signals from short nucleotides and 50 bp ladders at 100 ng/μL. In contrast, the sensors responded very similarly to injections of 50 bp DNA ladder and 1 kbp DNA ladder at the same mass concentrations (Figure 5–6b).

Several inferences can be drawn from the data. For relatively short DNA, the magnitude of the response correlates positively with length. However, as similar dose-response curves for 50 bp and 1 kbp DNA ladders were obtained, it could be inferred for sufficiently long DNA, the response becomes independent of length and is instead dominated by the total nucleotide mass concentrations. Since PCR is a process that converts short oligomers and nucleotide monomers to longer double-stranded DNA, the measurements shown in Figure 5–6 suggests that the magnitude of the sensor response can be used to determine whether or not the target sequence was amplified. This analysis also shows that when optimizing PCR protocols for sensitivity with field-effect readout, maximizing total product yield rather than product length should be the primary consideration. This property is desirable given that amplifying long templates can be very challenging. [147]

5.3 Microelectronic real-time PCR Quantification

A segment of the HIV-1 gag gene was amplified and the products were analyzed at various stages of the reaction. Figure 5–7a shows the time-course response of the electronic detector, and Figure 5–7b shows the comparison of end-point measurements by optical detection with an intercalating dye, by gel electrophoresis, and by electronic detection. Real-time Sybr Green I fluorescence readout showed a marked increase after approximately 20 cycles of amplification. Electronic measurements of PCR experiments terminating after various cycles also showed an increase in output after the 15th cycle, but the steepest rise was registered between the 15th and 20th cycle,

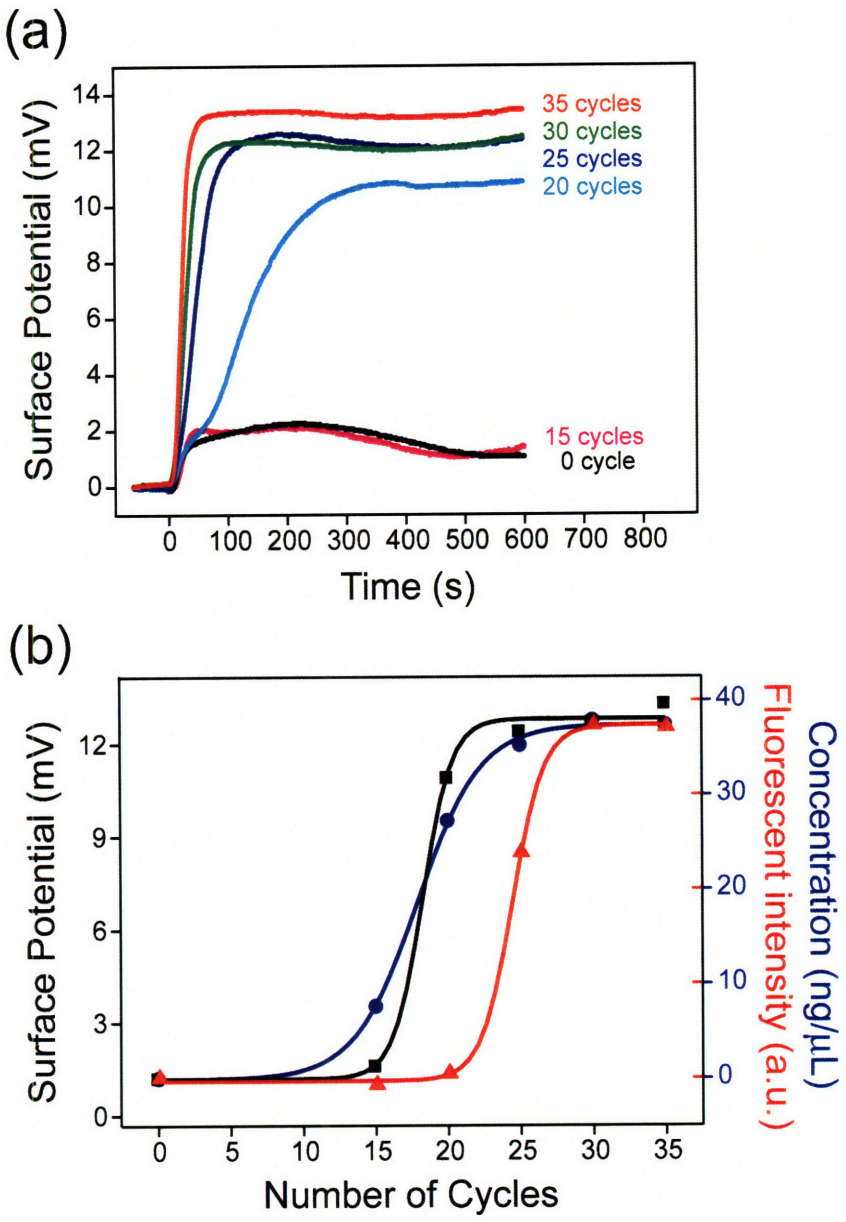

Figure 5–7: PCR progress monitoring using electronic and optical measurement methods. (a) Real-time electronic surface potential measurements for injections of PCR products. Reaction mixtures terminating after different number of cycles (0, 15, 20, 25, 30, 35) were introduced to the electronic sensors for 5 minutes followed by 5 min rinsing. The sensor was regenerated after each measurement by injecting PLL solution. (b) Comparison between steady state response of electronic measurements (black squares), real-time monitoring of PCR using Sybr Green I intercalating dye at 10,000 fold dilution from stock solution (red triangles), and concentration analysis of the products using DNA Labchip kits (blue circles). No fluorescent labels were used for electronic detection and concentration measurements.

compared to the 20th and 25th cycles for the Sybr Green measurement. To further analyze this discrepancy, the PCR products used for the electronic measurements were also separated and quantified using Labchip kits. As shown in Figure 5–7b, there is good correspondence between the product concentrations as measured by the Labchip kit and the electronic results. Both sets of data show the largest increase between 15th and 20th cycle, indicating the electronic readouts were representative of product concentrations. One possible explanation for the discrepancy with the Sybr Green I measurement is that the fluorescent reagent partially inhibits the PCR reaction [50, 49]; indeed total inhibition of PCR reaction occured when 3 times the factory recommended concentration (10,000x dilution of stock solution) of Sybr Green I dye was included in the PCR mixture at low starting template concentrations which otherwise yielded positive amplification. As a control, 40 ng/μL of DNA ladder was injected before and after analyzing the series of PCR products and observed similar responses. This confirms that the sensitivity of the sensor is preserved throughout the measurements.

Since this electronic PCR detection format measures total amplified products indiscriminately, it does not offer the additional specificity afforded by hybridization approaches. Thus, it must be viewed as a complement rather than a replacement for sequence-specific hybridization-based PCR detection schemes. However, electronic detection of PCR based on electrostatic association of polyelectrolytes offers several advantages over detection by hybridization. First, there is no need to denature the duplex PCR product as in cases where immobilized single-stranded DNA is used as capturing probe. Second, the association rate resulting from electrostatic interactions between DNA and PLL is up to 3 orders of magnitude faster than for hybridization events. [143, 144] Third, the structural robustness of layer-by-layer deposition allows multilayers of up to hundreds of layers [84], and a fresh layer of PLL is deposited before every analytical step. This feature contrasts with techniques that rely on washing to regenerate probe surfaces for additional hybridization experiments. Such regenerations can require harsh conditions and reduce the sensitivity of sensor by up to 20% between trials due to damage to the functionalized surface. [148]

Chapter 6

Device Integration

This chapter presents an integrated platform for amplification and label-free detection of nucleic acids. First, specific attempts to address the concerns with micro-PCR and the results achieved will be discussed. The operational principles of a microdevice that combines amplification and electronic detection will be shown. A simple strategy to convert the analog surface potential output of the field-effect sensor to a simple digital true/false readout for the presence/absence of a nucleic acid sequence will be demonstrated.

6.1 Micro-PCR Optimization

Since microchannels have a high surface-to-volume ratio, the channel surface properties are one of the most critical determinants of PCR product yield. Two major categories of surface passivation strategies for maximizing yield are: i) static passivation where channels are pre-treated with coatings during device fabrication or immediately before PCR, and ii) dynamic passivation where passivating chemicals are mixed directly in with the PCR solution. [40] Typical passivation coatings include silicon oxide surface modification for static passivation [52], bovine serum albumin (BSA) for both passive and static passivation [34, 149, 46], polyethylene glycol (PEG) for dynamic passivation [150, 151], and various channel silanizing agents for static passivation [152, 42]. In this work, both static and dynamic passivation have been

applied using a mild nonionic surfactant $n-$Dodecyl$-\beta-$D $-$ maltoside (DDM). [153] DDM adsorbs strongly on hydrophobic surfaces, such as graphite, and forms a monolayer. [154] This monolayer coverage causes the surface to become hydrophilic and nonionic, thus reducing the interaction between the protein and the surface. Because alkyl olyglucosides do not affect the functionality of many proteins, for example, by solublizing proteins without denaturation, it is possible to keep a certain concentration of DDM in solution so that it equilibrates with the adsorbed surfactant molecules. To investigate surface passivation by DDMS, the PCR channel was flushed the channel with deionized water containing 0.1% DDM for 10 minutes before a reaction, and PCR reagents mixed with 0.1% DDM were used for on-chip amplification.

The following PCR components were used in a reaction. Forward primer, 5' ATC AAG CAG CCA TGC AAA TG 3', and reverse primer, 5' CCT TTG GTC CTT GTC TTA TGT C 3', were used to amplify a 291 base pair (bp) fragment of the HIV-I GAG gene (Genebank accession no. K02007). The PCR buffer consisted of 10 mM Tris-HCl (pH 8.3), 20 mM KCl, 2 mM $MgCl_2$. The reaction mixture included the PCR buffer, 0.1 mM each of four dNTPs, 0.4 μM each of forward and reverse primers, 5 U Taq polymerase (New England BioLabs, Ipswich, MA), 0.1% DDM (Sigma, St. Louis, MO), and 0.1 ng/μL control template. Positive control template was an HIV-I proviral plasmid (Maxim Biotech, Rockville, MD), and the negative control template was ΦX174 Virion DNA (New England BioLabs). The PCR was performed for 25 cycles of 90 °C for 15 s, 52 °C for 15 s, and 68 °C for 30 s.

Two methods have been employed to optically detect chip-based PCR products. A fluorescent microscope setup based on Nikon SMZ-1000 stereo microscope (Nikon USA, Melville, NY), FITC Filter (31001, Chroma Technology Corp, Rockingham, VT), and MicroMAX 1300YHS CCD Camera (Princeton Instruments, Roper Scientific, Tucson, AZ) was constructed to directly measure product concentration level on-chip using a PCR mix with 10,000-fold standard dilution Sybr Green I (Molecular Probes). Because the microfluidic channel has 2 μL volume, product visualization by conventional gel electrophoresis (Sybr Safe Gel kit, Invitrogen, Carlsbad, CA) was also possible. Using these methods, an increase in the average pixel intensity was

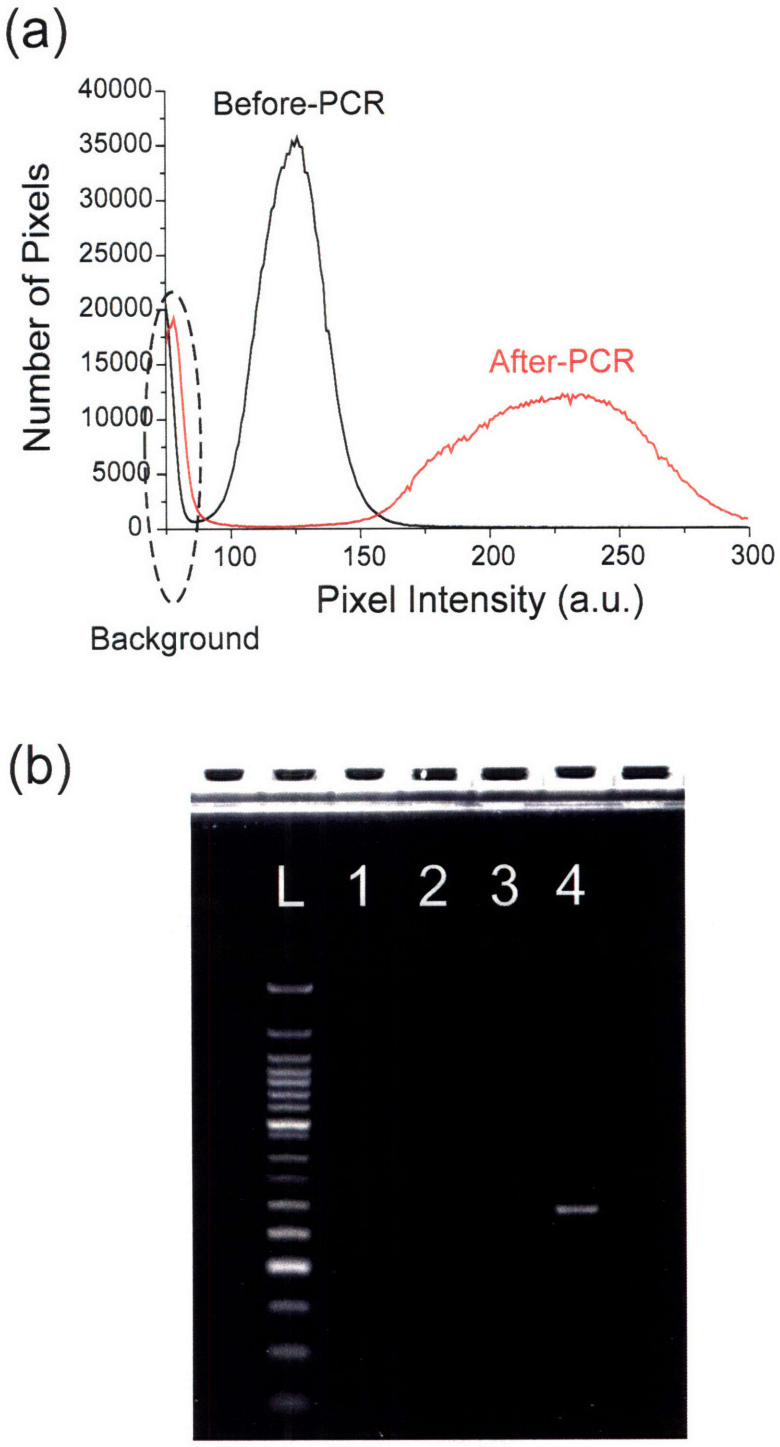

Figure6–1: On-chip PCR product detection by optical methods. (a) PCR product quantification on-chip using fluorescent Sybr Green I dye before and after a reaction with positive control template containing a 291bp segment of HIV-I GAG gene. (b) Analysis of chip PCR product by gel electrophoresis. PCR reactions were performed with a positive control gene and a negative control gene: Lane L, 50bp DNA ladder; lane 1, negative template before thermocycling; lane 2, positive template before thermocycling; lane 3, negative template after thermocycling; lane 4, positive template after thermocycling.

clearly observed on-chip, and a clear gel electrophoresis band was observed off-chip gel analysis using samples containing the HIV-I GAG positive control gene template (Figure 6–1). Furthermore, when quantified by Agilent LabChip kits, product concentrations in excess of 40 ng/μL was measured for on-chip PCR products, compared to 35 ng/μL and above for identical reagents amplified in a bench-top system. When control experiments were carried out to test whether DDM would interfere with electronic multilayer-based PCR detection, no transient signal or permanent baseline shift was observed, indicating that the passivating agent is compatible with the electronic sensing technique.

When conducting PCR with our device, it was occasionally noticed that the PDMS valve would remain shut permanently after thermocycling, preventing any subsequent analysis of the PCR product. It is anticipated that more comprehensive PDMS surface treatments can alleviate these issues. [155]

6.2 Integration of PCR and Electronic Sensing

The integrated device is configured to perform end-point detection of samples before and after on-chip thermocycling. The experimental protocol shown in Figure 6–2 is as follows: i) the sensor is first functionalized with PLL, ii) as the PCR channel is filled with PCR reagents, a measurement is simultaneously acquired, iii) once thermocycling is completed, the sensor is again functionalized with PLL, and iv) the previously closed valves which isolated the PCR channel are opened and the content is delivered to the electronic sensor for a second measurement. Since each chip has two electronic sensors, a set of four curves is expected for each PCR experiment.

To demonstrate the utility of this protocol, two control experiments were performed using: i) PCR mix which had a template containing HIV-I GAG gene and the primers designed to amplify a 291 segment in the template, and ii) PCR mix with the same conditions but with a virion template that did not contain the sequence. Figures 6–3(a) and 6–3(b) show the time course surface potential data for measurements taken before and after thermocycling, respectively. In Figure 6–3(a), prior to

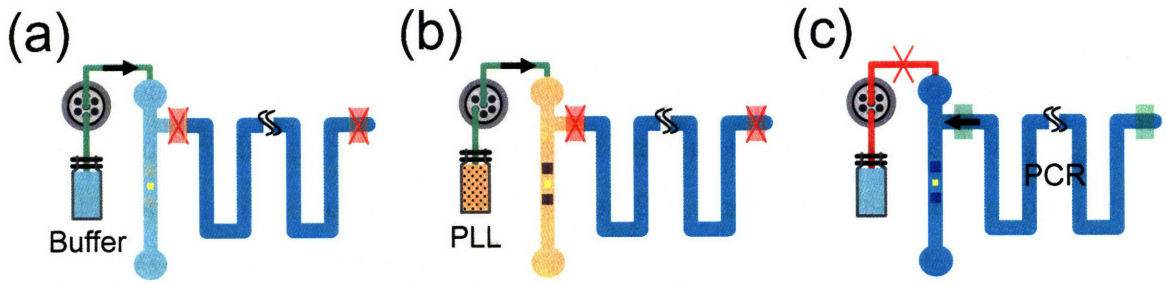

Figure6–2: Microfluidic operations for sensor functionalization and detection using a combination of on-chip and external selection valves. (a) PCR measurement buffer is injected through an external selection valve during sensor stand-by mode. (b) Injection of PLL from a different vial by switching the external selection valve to functionalize the sensor for DNA detection. (c) Valves isolating sensor channels from the PCR channel are opened to enable measurement of PCR product amplified on chip. After step (b) or (c), sensor rinsing by step (a) is necessary to wash away unbound molecules.

thermocycling, there was a transient response during injection of the PCR sample but the sustained response after restoring the measurement buffer was all below 3.2 mV. This transient response was created not only by the presence of charged molecules (e.g. dNTPs) that caused temporary baseline shifts, but also by disturbance from the opening (and subsequent closing) of microfluidic valves and the pressure fluctuations due to the injection of PCR sample. However, when the valves were closed, and the initial measurement buffer flow condition was restored, the electronic reading became directly comparable to the initial baseline value again. While the sensors were also affected by transient conditions after thermocycling, the two distinct positive control experiments on different devices produced a permanent increase of more than 10 mV over baseline value, whereas the response from negative controls were less than 3.2 mV. To ensure the sensor was functional after the thermocycling and that the negative post-PCR measurements was not simply due to a loss in sensitivity, the sensors were subjected to a third measurement of 40 ng/μL 50 bp ladder, which resulted in an approximately 9 mV response on all sensors. Based on the baseline shifts, a threshold value can be defined that converts the analog potential readings to a digital readout. For example, in this particular example, 10 mV was defined as a threshold for 'true'

and 3.2 mV as a threshold for 'false'; a digital sequence detector would require a pre-PCR value of 'false' and post-PCR value of 'true' for a positive amplification.

The throughput of the device can be estimated by considering the time required for the individual steps followed in the experimental protocols. Before analysis of PCR product, the sensor requires a 2 hour equilibration time following acid treatment. Analysis of a single product requires 5 minutes for PLL-functionalization, and another 5 minutes for DNA sensing. Assuming PCR requires 1 hour on a microdevice, the throughput of a device with a single PCR channel and single sensor would, in principle, be 20 samples/day. However, depending on the ultimate cost per device and specifics of the application, it may be more desirable to use the devices in a disposable format.

Detection throughput for electronic sensing of PCR product could potentially be improved using the following strategies. Since the sensor can be functionalized during thermocycling, the PLL functionalizing step does not need to be added to the required sample analysis time; therefore throughput is primarily limited by the combined time of the initial equilibration and the thermocycling. The sensor could also be left in a 'standby' mode indefinitely without losing its sensitivity. This feature could allow the initial equilibration to be performed during the manufacturing of a hand-held nucleic acid analytical device based this electronic sensing technology, and the device would be ready for PCR and sensing on demand. Several strategies also exist for improving PCR product measurement time. Currently, DNA measurement step involves flowing content in PCR channel through the sensor for 3 minutes to ensure sensor surface saturation for the maximum electronic signal. However, this time could potentially be minimized by characterizing the lowest possible injection volume required of a positively-amplified sample to yield a signal above a positive threshold value. Another rate-limiting step for DNA measurement is sensor stabilization time after injection of PCR sample. The reason for the temporary drift could be explained in part by the electrical couplings of mechanical events including the switching of on-chip valves and changing of injection pathways i.e. from reagents in PCR channel to measurement buffer. Thus, PCR measurement time could potentially be improved by modifying

the microfluidic design to better isolate it from possible external disturbances that could couple into the signal.

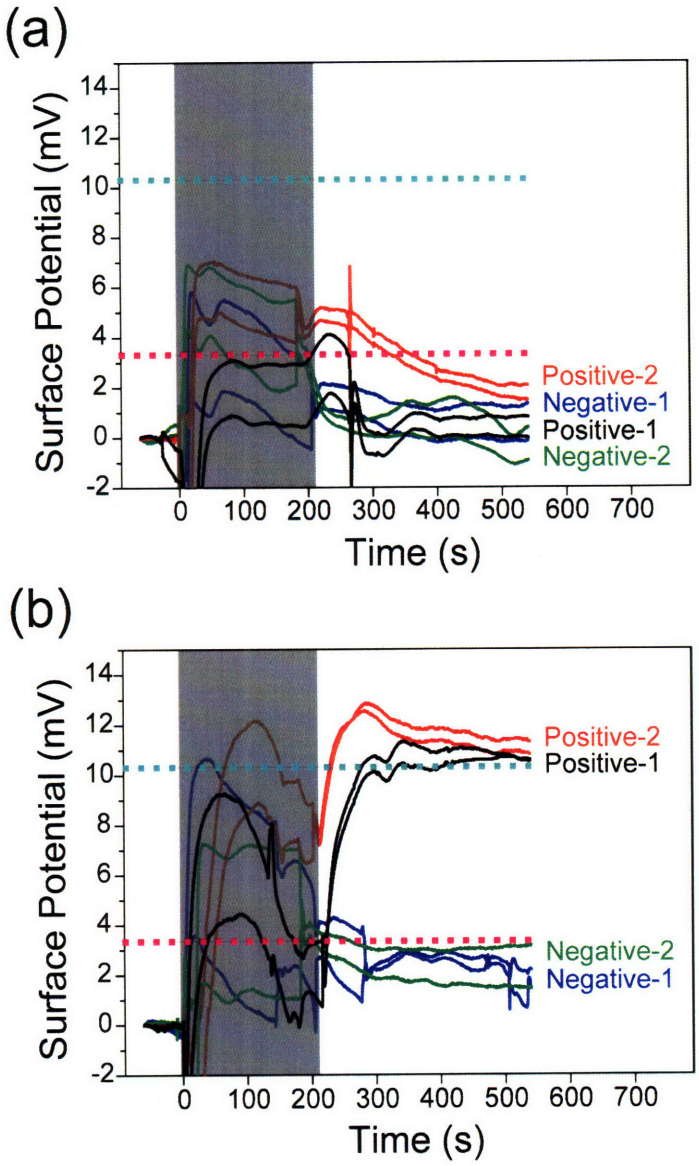

Figure6–3: Integrated PCR and field-effect sensing of product.For each PCR experiment, measurements were taken both (a) before and (b) after thermocycling. Every control experiment was performed on two distinct devices, each containing two sensors producing independent readouts. The same microfluidic operations were followed for both pre-PCR and post-PCR measurements. The PCR channel was replenished with starting PCR reagent as its content was flowed into the sensing channel. The grey-out area indicated the period of PCR channel injection. The higher and lower dotted segments are arbitrarily defined threshold levels for positive and negative signals, respectively.

Chapter 7

Heparin Sensing by Field-effect

This chapter presents the application of field-effect sensor to clinical heparin sensing using polyelectrolyte multilayer assembly. First, the clinical importance of heparin sensing and the limitations of current diagnostic tools will be discussed. The multilayer assembly of heparin and protamine will be described, and a microfabricated device architecture that employs differential sensing to allow accurate measurement of heparin in a sample with a high concentration of background molecules such as serum will be shown. The protocols of heparin sensing will be discussed, and measurements of heparin in pure buffer and serum will be analyzed. The detection of heparin-based drugs such as the low-molecular-weight heparin enoxaparin (Lovenox®) and the synthetic pentasaccharide heparin analog fondaparinux (Arixtra®), which cannot be monitored by the existing near-patient clinical methods, will also be described. The chapter concludes with a discussion of future directions to enhance specificity by immobilizing heparin-binding proteins to sensor surface.

7.1 Background

The complications associated with regulating blood coagulation present major health concerns that can be managed by careful administration and monitoring of anticoagulation drugs. [156, 157] In a clinical setting, it is critical to maintain anticoagulant levels that are sufficient to prevent thrombosis yet low enough to avoid bleeding risks.

Heparin has been used as a major anticoagulant, and it is second to insulin as a natural therapeutic agent. [158] Heparin is a linear glycosaminoglycan consisting of uronic acid-(1 → 4)-D-glucosamine repeating disaccharide subunits containing variable substitution with N-sulfate, O-sulfate and N-acetyl groups (Figure 7–1). [159] The biological activities of heparin result from sequence-specific interactions with proteins, most importantly with antithrombin III (AT-III), a serine protease inhibitor that mediates heparin's anticoagulant activity. [160,161,162] Heparin and other structurally similar glycosaminoglycans have been implicated in various other biological processes including embryonic development, cancer metastasis, and viral pathogenesis. [163, 164, 165]

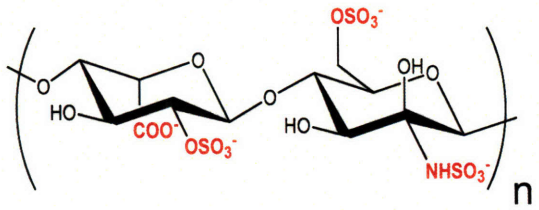

Figure 7–1: Heparin Structure.

Despite the widespread use, the native, unfractionated heparin has many limitations, such as interpatient variablility, non-specific protein binding, unstable pharmacokinetics, and side-effects such as hemorrhage and heparin-induced thrombocytopenia. [166] The variability of heparin arises from its complex molecular structure, intrinsic polydisperity (Mw ranges from 3 to 30 KDa) and heterogeneity of samples (only one in three molecules contains the active AT-III-binding site). [167] Clinical use of heparin remains high because it is the only anticoagulant drug that can be effectively controlled and neutralized by an antidote, namely cationic protein protamine. [168]

Low-molecular-weight heparins (LMWHs), i.e. heparin molecules with reduced chain length, have been designed as a class of heparin-based drugs with improved bioavailibilty, simplified administration, more predictable dose response and pharmacokinetics, and therefore improved safety. [169] LMWHs such as enoxaparin (Lovenox®),

which is generated by chemical β-elimination of heparin, have been used for prophylaxis of deep venous thromboembolysms (DVT), which occurs in as many as 50% of patients after undergoing elective orthopedic surgical procedures. Compared to heparin, LMWHs have a longer half-life and a lower incidence of complications. [170] Fondaparinux (Arixtra®), a synthetic heparin-based drug based on the unique pentasaccharide AT-III binding domain of heparin, has antithrombotic anti-Xa activity superior to LMWHs, and is therefore used for the prevention of thromboembolic events following elective orthopedic surgery and other prophylactic indications, as well as the treatment of DVT, pulmonary embolisms, and coronary artery diseases. [171] Although LMWHs and fondaparinux improve upon heparin's therapeutic limitations, they also have shortcomings. The most important safety concerns are that the anticoagulant activity of LMWHs and fondaparinux cannot be effectively neutralized [172], and that their blood level cannot be effectively monitored by current point-of-care clinical methods. Without the ability to monitor and control their blood level, LMWH are unsuitable for certain critical and unmet clinical needs. For example, patients with acute coronary syndrome taking LMWH are at high risk of bleeding complications in the case of an urgent surgical intervention. [173]

Standard clinical procedures for monitoring anticoagulant activity of heparin are based on measuring the activated clotting time (ACT) or activated partial thromboplastin time (APTT). [174,156] Although widely used, these tests often fail to provide the actual heparin level because the clotting time can be affected by additional factors commonly encountered during surgery, such as hypothermia or hemodilution, as well as abnormal levels of clotting factors. [156, 175, 176] It has been demonstrated that careful patient-specific assessment of heparin levels would reduce the occurrence of anticoagulation complications. [175, 177] Standard colorimetric assays of heparin levels based on the anti-Xa or other activities are available, but they require laboratory settings and elaborate sample handling. There have been extensive efforts to develop new devices suitable for routine measurement of heparin levels in clinical settings. [156, 178] Various approaches such as, for example, quartz crystal microbalance, surface plasmon resonance, ion-sensitive field-effect transistor, and membrane-

based ion-selective electrode involve either protamine or synthetic cationic polymers as heparin probes, and are either based on surface affinity capture or on an automated heparin titration. [178, 179] Such methods have had variable success in fully achieving the required objectives: selectivity, sensitivity, robustness and reusability. Moreover, because the heparin capture is based on non-specific, activity-independent electrostatic binding, these measurements are of limited utility since they can only determine total rather than clinically active heparin. [167]

7.2 Assembly of Heparin-Protein Multilayer

Since heparin is a strong linear polyanion of polysaccharide nature that is heavily sulfated (~3.3 mmol sulfate groups/g), it is possible to construct a multilayer based on heparin and positively charged proteins through layer-by-layer depositions. This property has been investigated for the heparin-albumin multilayer system. [180] In the study, the heparin with various ranges of molecular weights from averages of 2000 to 15,000 were tested for their abilities to form multilayers with albumin. It was observed that all heparins tested were very effective links for the layer-by-layer assembly with albumin, and based on the amount of heparin adsorbed in each layer, it was concluded that heparin is one of the most efficient polyelectrolytes in forming multilayers with albumin. Several reasons are possible for this efficient interaction. First, the interaction of heparin and various proteins are not only of electrostatic origins, but the specific structure strengthens association with these proteins. For example, it has been shown that even the interaction of heparin with albumin is not specific, it can interact with albumin even at pH above its isoelectric pointwhere albumin bears a net negative charge. [181] Such interactions are usually explained by uneven distribution of charges on protein resulting in local charge clusters that can bind polyelectrolyte of the same charge polarity as the net charge of the proteins. [182] However, heparin is a very strong polyanion, which may shift ionization of the protein, and the stoichiometry of the multilayer may correspond to a lower pH than is the bulk pH. [181]

In this study, the ability of heparin to form multilayers with protamine, a clinical heparin antagonist, was investigated. The layer-by-layer deposition of protamine and heparin was examined using Sentech SE400 ellipsometer (Sensor Technologies America, Carrollton, TX), with the assumed refractive index of organic film of 1.5. The experiments were done by the alternating 5-min exposure of a 1 cm^2 piece of silicon wafer to a 20 μM protamine solution and 1 U/mL heparin solution, separated by a buffer rinse. The first deposition of protamine-heparin pair yielded a 0.78 $\pm$ 0.29 nm thick film, whereas ten deposition cycles produced a film with thickness of 7.36 $\pm$ 0.56 nm, consistent with ten protamine-heparin layers. This feature suggests that just as in the studies involving DNA and polylysine multilayers, it could be possible to regenerate the sensor surface and the recover the initial signal baseline after a round of heparin measurement by simply flowing a protamine solution through the sensor. This allows for multiple measurements on the same device, a feature necessary for clinical applications requiring real-time monitoring.

7.3 Device Design

Figure 7–2a shows an optical micrograph of two EIS structures with $50 \times 50\,\mu m^2$ sensing surfaces in separate microfluidic channels. Twenty sensors (two in each channel for redundancy) were fabricated on a single chip using the process described in Section 3.3 and were subsequently encapsulated with glass microchannels. Glass microchannels which were fabricated using a metal-based HF etch mask were more robust to stringent cleaning procedures, and they eliminated defects and tediousness associated with hand packaging individual devices with PDMS slabs. A cross-section of the structures (Figure 7–2b) illustrates the use of two adjacent channels for differential molecular measurements. Specific detection of biomolecules requires prior sensor surface functionalization with receptors that exhibit high specificity towards the target analyte. In order to reduce unwanted interference from bulk properties of the solution (e.g. ionic strength and pH) and, to some extent, the interference from nonspecific binding, measure the difference in surface potential between two sensors

in adjacent channels were measured. The active sensor is modified with a heparin receptor, protamine, and the control sensor is passivated with BSA.

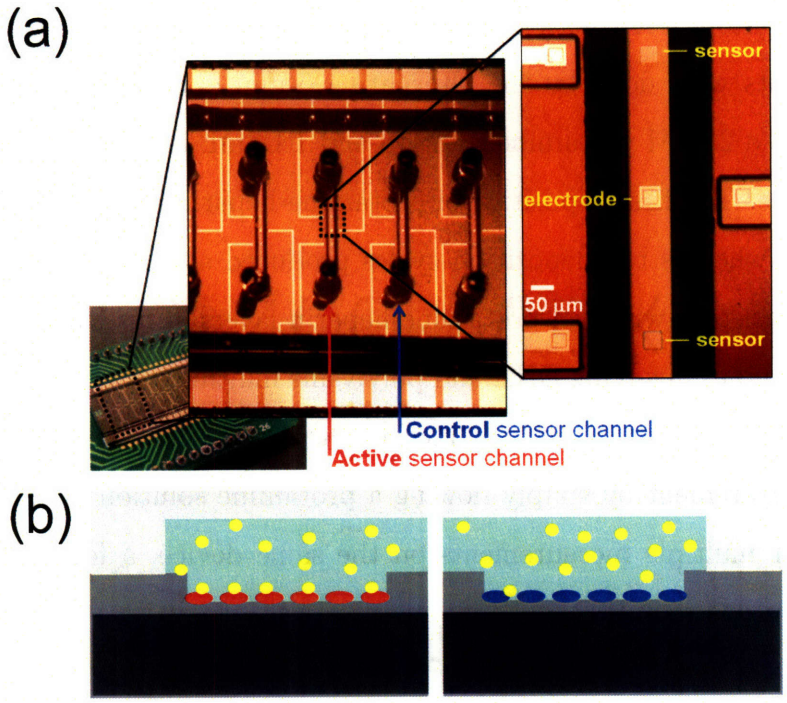

Figure 7–2: Glass-encapsulated device for differential heparin measurements. (a) Optical micrograph showing an array of parallel anodically bonded glass microfluidic channels, each containing two field-effect sensors and a gold signal electrode. Differential measurements involved two channels, one for the active sensor and another for the control sensor. b) Schematic illustration of device operation showing the use of two adjacent channels for differential measurements. Heparin (yellow) binds to the surface of the sensor containing the protamine receptor (red) whereas this binding is absent for the control sensor passivated by BSA (blue).

7.4 Heparin Sensing

Total heparin concentration is measured by modifying the active sensor with protamine, a high affinity (Kd $< 10^{-7}$M) [183] cationic protein used as a heparin antagonist. Figure 7–3a shows absolute and differential surface potential response of protamine sensor to a 0.3 U/mL heparin solution, and the subsequent recovery of the protamine surface. During the injection (blue shaded region) the active and con-

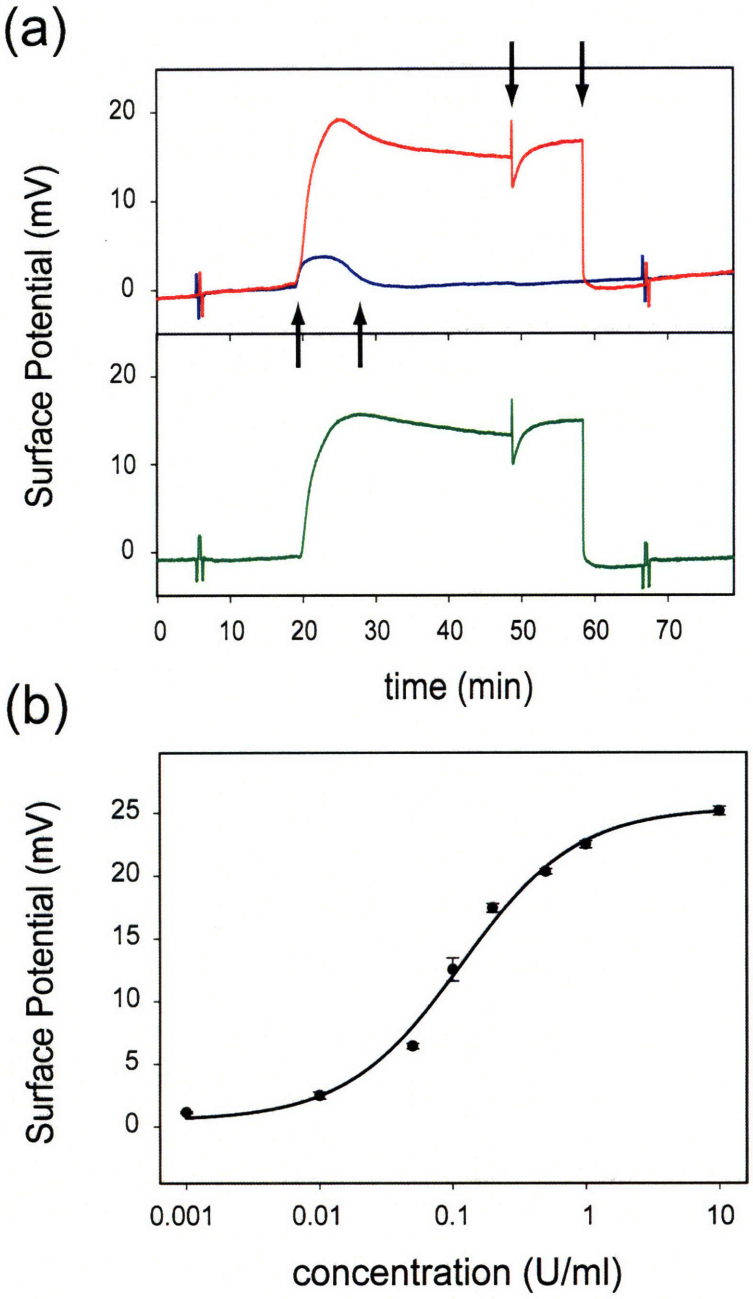

Figure 7–3: Differential heparin measurements with protamine sensors. (a) The response to a 0.3 U/mL heparin solution in 10% PBS of the active sensor (red) and the control sensor (blue). The differential response (green) reveals the surface potential change caused by heparin binding by eliminating bulk solution effects. The arrows from left to right correspond to the injection of heparin solution, rinse with running buffer, injection of protamine solution, and the second buffer rinse. The spikes at 6 and 67 min corresponds to externally applied positive and negative 2.5 mV calibration signal. (b) Dose-response curve for heparin in 10% PBS from a protamine functionalized sensor

trol sensor respond to surface adsorption as well as to the slight difference between ionic strength and pH of the sample and the running buffer. The resulting differential response, however, eliminates the bulk effects, and the signal primarily represents heparin binding to the active sensor. Arrows (from left to right) indicate the injection of heparin solution, buffer, a 20.0 μM protamine solution, and the final buffer rinse. The increased baseline upon injection of heparin solution, expected from its negative charge, gradually decreases during the buffer rinse, which suggests a slow dissociation of sensor-bound heparin in the non-equilibrium conditions of the flow-through setup. The transient baseline change during protamine injection over the active sensor originates from the variations in ionic strength and pH between the 20 μM protamine solution and the running buffer.

The baseline recovery to the original level prior to heparin injection is consistent with the surface deposition of a fresh protamine layer on top of the existing heparin layer. Importantly, as in previous measurements involving DNA and polylysine multilayers, the deposition of multiple layers does not decay signal amplitude over multiple measurements, suggesting that the overcompensated surface charge at the top layer is effectively propagated to the sensor surface, a feature that allows for multiple measurements on the same device.

To evaluate the performance of the protamine sensor, the dose-response curve for heparin in buffer (Figure 7–3b) was measured and it was found that the sensitive region ranges over two orders of magnitude, from approximately 0.01 to 1 U/mL. Heparin doses given to patients are typically in the range of 2-8 U/mL (0.8-3.2μM) during bypass surgery, and an order of magnitude lower for postsurgical therapy. [156] Evidently, the protamine sensor is capable of detecting heparin at and below clinically relevant concentrations. In this way, the most sensitive range of the dose-response curve could be matched to a desired range by an appropriate dilution of a clinical sample.

To demonstrate clinical utility of the protamine sensor, samples of diluted human serum spiked with known heparin concentrations were analyzed. The resulting calibration curve, shown in Figure 7–4, corresponds to the range of 0.5 U/mL to 20

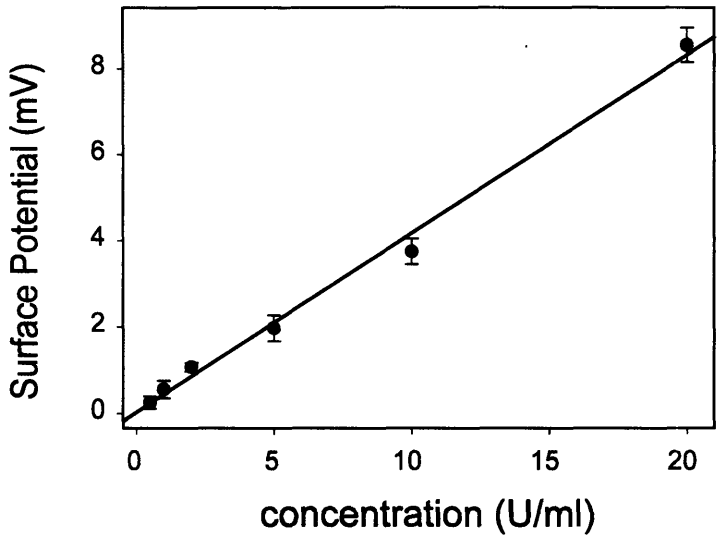

Figure7–4: Clinically relevant range of the dose response curves from the protamine sensor for heparin in 10% human serum. Each data point is an average of two measurements and the error bars represent two standard deviations.

U/mL for the original undiluted serum. The observed decreased sensitivity (detection limit of 0.05 U/mL in 10% serum) compared to the buffer samples can be attributed to partial heparin neutralization by serum proteins such as platelet factor IV [174], as well as to surface fouling by interfering molecular species present in the serum sample. Importantly, the device response remained linear in the clinically relevant range, providing simple device calibration and easy readout and data interpretation.

The demand for laboratory monitoring of LMWH is not as frequent as for heparin since the interpatient variability in dosage requirements is much lower. There is, however, a growing view that monitoring is necessary in certain cases. The guidelines of the College of American Pathologists recommends laboratory monitoring in pediatric patients and suggests laboratory monitoring in patients with renal insufficiency, those receiving prolonged therapy including pregnancy, those at high risk of bleeding or thrombotic recurrence, and patients with obesity or low body weight. [175] The current inability to monitor LMWH levels particularly limits its usage in catheterization laboratory, and a simple and rapid point-of-care monitoring system would therefore improve the safety and efficacy of LMWH administration. [173]

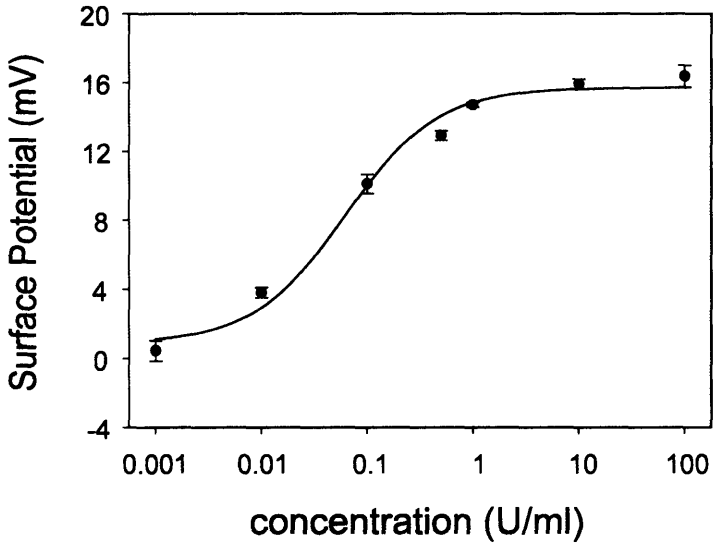

Figure 7–5: Dose response curves of the protamine sensor for enoxaparin in 10% PBS. Each data point is an average of two measurements and the error bars represent two standard deviations.

Figure 7–5 shows the dose-response curves of enoxaparin binding to the protamine sensor. As with unfractionated heparin, the sensitive region of the dose-response curve includes the clinically relevant concentrations. Although protamine is not effective at completely neutralizing the activity of LMWHs *in vivo*(it neutralizes the anti-thrombin activity but not the anti-Xa activity) [184], the interaction is sufficient to detect enoxaparin using protamine sensor. The somewhat lower sensitivity and the signal amplitude compared to heparin can be attributed to lower electrostatic binding affinity of relatively shorter polysaccharide chains, and less overall negative charge introduced to the surface.

7.5 Comparison with Anti-Xa Assay

As a validation for clinical use, the electronic measurements were compared with an assay of heparin's anti-Xa activity (Coatest), a standard method for clinical assessment of heparin levels. Although ACT and APTT remain the dominant tests for monitoring anticoagulation, it is widely known that they poorly correlate to the actual

heparin level due to the lack of specificity and interference of other factors. [175,176] Enzymatic assays such as this anti-Xa assay (which has a correlation coefficient of $\geq$0.90 with the APTT), are more accurate in reporting heparin levels, but they are complex, reagent-intense, and they require laboratory settings, which makes them impractical for routine near-patient testing. Moreover, the anti-Xa assay relies on unstable reagents, is sensitive to the presence of other molecules that can affect stability of chromogenic substrate and activity of Xa, and is sensitive to Xa levels in test plasma.

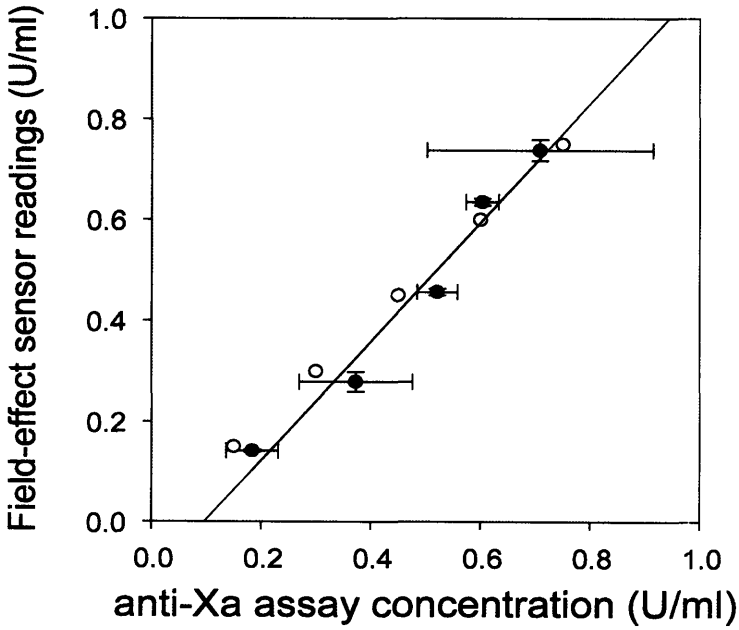

Figure7–6: Correlation between field-effect sensor and Anti-Xa assay measurements .Linear correlation ($rr^2 = 0.97$) between the values for different heparin concentrations in 10% PBS by field-effect measurements and by the colorimetric anti-Xa assay (•) were measured. The values were obtained using a five-point standard curve in the range of 0.1 to 0.9 U/mL. The actual values (o) were 0.1, 0.3, 0.45, 0.6, and 0.75 U/mL. The samples were diluted 10 times in the case of field-effect measurements. The horizontal error bars represent the standard deviation from three distinct anti-Xa assays and the vertical error bars represent the standard deviation from two field-effect measurements.

To compare the performance of protamine sensor to that of anti-Xa assay and to the actual heparin concentrations, a standard curve for each method using 0.1, 0.3, 0.5, 0.7 and 0.9 U/mL solutions of heparin to construct a standard curve was

obtained, and these were used to determine five 'unknown' concentrations in this range by both methods. Because the sensitivity of protamine sensor exceeds the range of anti-Xa assay (broadly 0.1-1.0 U/mL) by an order of magnitude, the samples were adequately diluted. Figure 7–6 shows a good correlation (correlation coefficient r^2 = 0.97) between the two methods. Importantly, the comparison of the standard deviations and the divergence from the expected values show that field-effect sensor exhibited both the better precision and the accuracy compared to anti-Xa assay.

7.6 Future Directions

While differential heparin sensing based on a protamine-functionalized surface offers the ability to measure heparin in a complex sample such as serum, the technique will not be able to distinguish the clinically active heparin from other highly charged molecular analogs such as chondroitin sulfate, which is structurally related to heparin and thus will bind electrostatically to the protamine-functionalized sensor. To overcome this issue, sensors that employ immobilized proteins with specific binding capability for heparin sensing are been developed. [185] The highly specific interaction between AT-III and heparin involves clinically active pentasaccharide domains, which are randomly distributed along the heparin chains and a single binding site on the AT-III surface. Using AT-III as surface probe, a dose response curve for heparin was obtained and revealed a K_d of 180 nM, while measurements of chondroitin sulfate yielded negligible response, thus confirming the selectivity of the AT-III sensor.

Although the sensor is capable of detecting heparin in plasma samples, the device exhibited a gradual decrease in sensitivity over successive sample runs, presumably due to non-specific deposition of plasma components in the sensor channel, a frequent problem of plasma-contacting medical devices. This limitation can be overcome by further suppressing non-specific binding (for example by coating the device surfaces by polyethylene glycol or adding mild surfactants to the sample) and by incorporating an efficient surface recovery regimen. Also, while the current device design requires

prolonged times for measurement and rinsing due to a complex fluid delivery system. This shortcoming can be overcome by incorporating the sensor into an integrated microfluidic system capable of handling small volumes and rapid on-chip exchange of samples.

Chapter 8

Conclusions

8.1 Conclusions

An integrated microelectronic device for the amplification and label-free detection of nucleic acids has been presented [186, 187]. This device consists of microfluidic channels and integrated valves molded in a silicone substrate which is bonded to silicon die with integrated heaters, temperature sensors, field-effect sensors and signal electrodes. The specific design allows direct endpoint product detections of a standard polymerase chain reaction without sample post-processing or use of additional sequence-specific reagents. As such, the device offers capability to directly detect double-stranded PCR product similar to existing optical approaches that use intercalating agents such as SYBR Green I, while in contrast the system does not require the additional optimization to a standard PCR reaction to avoid inhibitory effects of the dyes.

The sensor consists of a microfabricated charge sensing Electrolyte-Insulator-Semiconductor (EIS) structure embedded in a silicon substrate. The field-effect sensor behaves as a variable capacitor whose impedance value is sensitive to the charge density of surface-bound molecules. By applying an AC voltage to a signal electrode inside the microfluidic channel, the resulting current that traverses the solution through the capacitor can be measured and converted to a relative surface potential value. Buried conductive traces are used to connect the signal electrode

and the field-effect sensor to metal traces that interface with external electronics in order to maintain a locally planar topography around channel area for robust sealing of microfluidic channels. Amplification by polymerase chain reaction (PCR) is achieved with on-chip metal resistive heaters, temperature sensors, and microfluidic valves. On-chip temperature sensing which enables close-loop temperature control is achieved by measuring the temperature coefficient of resistance of metal wires. The reduced thermal mass and high thermal conductivity of a silicon microdevice permits rapid thermocycling with rates of up to 50 °C/s and excellent uniformity of less than 1 °C within the channel.

Direct label-free detection of PCR product is enabled by electronic sensing of layer-by-layer assembly of polyelectrolytes. First, the sensor surface is exposed to a solution containing positively charged polyelectrolytes PLL which bind to the negatively charged silicon oxide surface. This gives the sensor the ability to bind negatively charged DNA such as PCR product DNA. The adsorption of DNA to the PLL-coated surface reverses the polarity of the sensor surface, making it capable of binding a fresh layer of PLL. The alternating depositions can be repeated indefinitely with no noticeable degradation in signal amplitude, hence allowing quantifications of multiple unprocessed PCR products. The technique measures nucleic acid concentration in the PCR relevant range and specifically detects the PCR products over reagents such as Taq polymerase and nucleotide monomers. The system is capable of differentiating nucleic acid concentrations at various stages of PCR by producing a readout which resembles that of fluorescent measurements using intercalating dyes in real-time PCR. By employing a nonionic microfluidic channel passivating agent $n-\text{Dodecyl}-\beta-\text{D}-\text{maltoside}$, PCR product yield equivalent to that of a bench-top system has been achieved. Active on-chip microfluidic control is employed to interface the amplification and detection subunits, which are independently functional. Finally, it has been shown that the presence or absence of a particular DNA sequence can be determined by converting the analog surface potential output of the field-effect sensor to a simple digital true/false readout.

Direct electronic label-free quantification of heparin has also been demonstrated

with layer-by-layer assembly of protein-polyelectrolyte complexes [185]. A glass-encapsulated microdevice with arrays of sensors and channels has been developed for differential sensing of heparin in a complex biological fluid such as serum. Heparin's clinical antagonist, protamine, has been used as the capture agent, and the dose-response curves revealed a detection limit of less than 0.01 U/ml, which is an order of magnitude lower than clinically relevant concentrations. This detection format also allows the measurement of heparin-based drugs such as the low molecular weight heparin enoxaparin (Lovenox®) and the synthetic pentasaccharide heparin analog fondaparinux (Arixtra®). To validate the potential for clinical applications, a strong correlation ($r^2 = .97$) between the electronic measurement and a standard assay of heparin's anti-Xa activity has been demonstrated.

8.2 Recommendations for Future Work

While electronic sensing of multilayer assembly is capable of multiple rounds of PCR product quantitation, there lacks a detailed understanding of the properties of the multilayer film and its scaling properties. Such understanding is necessary to predict the sensitivity of the sensing technique given a particular combination of reagents and buffer conditions for PCR.

Currently, native oxide is used as the gate dielectric of the sensor due to the simplicity of fabrication and high sensitivity. However, the composition and thickness of native oxide depends heavily on surface preparation conditions and is prone to drift, thus it is worthwhile to explore whether employing a gate oxide with defined thickness can improve stability and reproducibility of different devices. In addition, other gate materials such as tantalum pentoxide film have been shown to exhibit higher pH sensitivity and linearity. It is interesting to see if a similar improvement can be achieved for the measurement of polyelectrolyte multilayers.

The integrated device has been designed to perform a single measurement of PCR product after thermocycling, and the PCR channel has been designed to carry a relatively high volume of reagents. However, it was discovered during the injection of

chip-amplified product that for a positive amplification, the sensor did not require all the volume to in order obtain a saturated sensor response, thus the volume can clearly be scaled down without affecting the sensor sensitivity. Also, it is relatively unknown what proportion of DNA in solution that flows through the sensor binds to it. It could be possible to develop a fluidic architecture that flows PCR reagents through a sensor in a closed loop using peristaltic pumping to ensure complete binding of product. The current integrated device is designed to give a digital response for the presence or absence of a particular sequence, while it has been demonstrated that the sensor can monitor multiple products and follow the progress of a reaction for real-time quantification of initial template concentration. Such prospect can potentially be realized by integrating multiple channels to a device and monitoring the content of each channel after different numbers of cycles of reaction.

The small footprint of the device can potentially allow packaging into a handheld device for field diagnostics. However, for direct analysis of crude samples, additional sample pre-processing capabilities must be added such as cell lysis and nucleic acid purification stages.

By integrating additional capabilities such as magnetic bead-based affinity capture, the integrated PCR-electronic sensing platform could potentially enable automated selection of protein-binding nucleic acid species (aptamers) with feedback capabilities. In vitro selection is a general and powerful technique for evolving nucleic aptamers against a large variety of molecules ranging in size and structure from cations to cells, but the procedure is time-consuming and error-prone. Protocols have been developed for automated workstations, reducing selection time from months to several days; however, robots cannot fine-tune parameters based on observed intermediate results as their human counterpart, thus they frequently generate spurious parasitic species. With improved thermocycling performance, a microfabricated device could potentially not only increase the throughput of automated selection, but also performs electronic label-free PCR endpoint readout to ensure the integrity of the aptamer pool during a selection.

Bibliography

[1] M. J. Dennison and A. P. F. Turner. Biosensors for environmental monitoring. *Biotechnology Advances*, 13(1):1–12, 1995.

[2] R. K. Saiki, S. Scharf, F. Faloona, K. B. Mullis, G. T. Horn, H. A. Erlich, and N. Arnheim. Enzymatic amplification of beta-globin genomic sequences and restriction site analysis for diagnosis of sickle-cell anemia. *Science*, 230(4732):1350–1354, 1985.

[3] M. Schena, D. Shalon, R. W. Davis, and P. O. Brown. Quantitative monitoring of gene-expression patterns with a complementary-dna microarray. *Science*, 270(5235):467–470, 1995.

[4] J. D. Hoheisel. Microarray technology: beyond transcript profiling and genotype analysis. *Nature Reviews Genetics*, 7(3):200–210, 2006.

[5] T. G. Drummond, M. G. Hill, and J. K. Barton. Electrochemical dna sensors. *Nature Biotechnology*, 21(10):1192–1199, 2003.

[6] M. Minsky. Memoir on inventing the confocal scanning microscope. *Scanning*, 10(4):128–138, 1988.

[7] D. Axelrod, T. P. Burghardt, and N. L. Thompson. Total internal-reflection fluorescence. *Annual Review of Biophysics and Bioengineering*, 13:247–268, 1984.

[8] S. Nagl, M. Schaeferling, and O. S. Wolfbeis. Fluorescence analysis in microarray technology. *Microchimica Acta*, 151(1-2):1–21, 2005.

[9] E. Waddell, Y. Wang, W. Stryjewski, S. McWhorter, A. C. Henry, D. Evans, R. L. McCarley, and S. A. Soper. High-resolution near-infrared imaging of dna microarrays with time-resolved acquisition of fluorescence lifetimes. *Analytical Chemistry*, 72(24):5907–5917, 2000.

[10] H. Harma, A. M. Pelkkikangas, T. Soukka, P. Huhtinen, S. Huopalahti, and T. Lovgren. Sensitive miniature single-particle immunoassay of prostate-specific antigen using time-resolved fluorescence. *Analytica Chimica Acta*, 482(2):157–164, 2003.

[11] W. Lian, S. A. Litherland, H. Badrane, W. H. Tan, D. H. Wu, H. V. Baker, P. A. Gulig, D. V. Lim, and S. G. Jin. Ultrasensitive detection of biomolecules with fluorescent dye-doped nanoparticles. *Analytical Biochemistry*, 334(1):135–144, 2004.

[12] P. Alivisatos. The use of nanocrystals in biological detection. *Nature Biotechnology*, 22(1):47–52, 2004.

[13] L. Zhang, T. Hurek, and B. Reinhold-Hurek. Position of the fluorescent label is a crucial factor determining signal intensity in microarray hybridizations. *Nucleic Acids Research*, 33(19), 2005.

[14] E. Engvall and P. Perlmann. Enzyme-linked immunosorbent assay (elisa) quantitative assay of immunoglobulin g. *Immunochemistry*, 8(9):871–874, 1971.

[15] T. Bacarese-Hamilton, L. Mezzasoma, C. Ingham, A. Ardizzoni, R. Rossi, F. Bistoni, and A. Crisanti. Detection of allergen-specific ige on microarrays by use of signal amplification techniques. *Clinical Chemistry*, 48(8):1367–1370, 2002.

[16] K. Baggerly, R. Mitra, R. Grier, D. Medhane, G. Lozano, and M. Kapoor. Comparison of sample-labeling techniques in dna microarray experiments. *Analytica Chimica Acta*, 506(2):117–125, 2004.

[17] T. A. Taton, C. A. Mirkin, and R. L. Letsinger. Scanometric dna array detection with nanoparticle probes. *Science*, 289(5485):1757–1760, 2000.

[18] Y. C. Cao, R. C. Jin, J. M. Nam, C. S. Thaxton, and C. A. Mirkin. Raman dye-labeled nanoparticle probes for proteins. *Journal of the American Chemical Society*, 125(48):14676–14677, 2003.

[19] J. Wang, R. Polsky, A. Merkoci, and K. L. Turner. "electroactive beads" for ultrasensitive dna detection. *Langmuir*, 19(4):989–991, 2003.

[20] O. Smithies. Zone electrophoresis in starch gels: group variations in the serum proteins of normal human adult. *Biochemical Journal*, 61(4):629–641, 1955.

[21] R. Higuchi, C. Fockler, G. Dollinger, and R. Watson. Kinetic pcr analysis - real-time monitoring of dna amplification reactions. *Bio-Technology*, 11(9):1026–1030, 1993.

[22] S. Tyagi and F. R. Kramer. Molecular beacons: Probes that fluoresce upon hybridization. *Nature Biotechnology*, 14(3):303–308, 1996.

[23] C. A. Heid, J. Stevens, K. J. Livak, and P. M. Williams. Real time quantitative pcr. *Genome Research*, 6(10):986–994, 1996.

[24] I. A. Nazarenko, S. K. Bhatnagar, and R. J. Hohman. A closed tube format for amplification and detection of dna based on energy transfer. *Nucleic Acids Research*, 25(12):2516–2521, 1997.

[25] D. Klein. Quantification using real-time pcr technology: applications and limitations. *Trends in Molecular Medicine*, 8(6):257–260, 2002.

[26] S. J. Skidmore, M. Zuckerman, and J. V. Parry. Accuracy of plasma hiv rna quantification: A multicentre study of variability. *Journal of Medical Virology*, 61(4):417–422, 2000.

[27] B. de Barbeyrac, M. Geniaux, C. Hocke, M. Dupon, and C. Bebear. Detection of chlamydia trachomatis in symptomatic and asymptomatic populations with

urogenital specimens by amp ct (gen-probe incorporated) compared to others commercially available amplification assays. *Diagnostic Microbiology and Infectious Disease*, 37(3):181–185, 2000.

[28] Ojhm Verhagen, M. J. Willemse, W. B. Breunis, A. J. M. Wijkhuijs, D. C. H. Jacobs, S. A. Joosten, E. R. van Wering, J. J. M. van Dongen, and C. E. van der Schoot. Application of germline igh probes in real-time quantitative pcr for the detection of minimal residual disease in acute lymphoblastic leukemia. *Leukemia*, 14(8):1426–1435, 2000.

[29] Milena Koudelka-Hep and Peter D. van der Wal. Microelectrode sensors for biomedical and environmental applications. *Electrochimica Acta*, 45(15-16):2437–2441, 2000.

[30] A. T. Woolley and R. A. Mathies. Ultra-high-speed dna fragment separations using microfabricated capillary array electrophoresis chips. *PNAS*, 91(24):11348–11352, 1994.

[31] Mark A. Burns, Brian N. Johnson, Sundaresh N. Brahmasandra, Kalyan Handique, James R. Webster, Madhavi Krishnan, Timothy S. Sammarco, Piu M. Man, Darren Jones, Dylan Heldsinger, Carlos H. Mastrangelo, and David T. Burke. An integrated nanoliter dna analysis device. *Science*, 282(5388):484–487, 1998.

[32] N. Zhang, H. Tan, and E. S. Yeung. Automated and integrated system for high-throughput dna genotyping directly from blood. *Anal. Chem.*, 71(6):1138–1145, 1999.

[33] R. H. Liu, J. Yang, R. Lenigk, J. Bonanno, and P. Grodzinski. Self-contained, fully integrated biochip for sample preparation, polymerase chain reaction amplification, and dna microarray detection. *Anal. Chem.*, 76(7):1824–1831, 2004.

[34] Mark A. Burns, Carlos H. Mastrangelo, Timothy S. Sammarco, Francis P. Man, James R. Webster, Brian N. Johnson, Bradley Foerster, Darren Jones, Yakeitha

Fields, Adam R. Kaiser, and David T. Burke. Microfabricated structures for integrated dna analysis. *PNAS*, 93(11):5556–5561, 1996.

[35] E. T. Lagally, C. A. Emrich, and R. A. Mathies. Fully integrated pcr-capillary electrophoresis microsystem for dna analysis. *Lab on a Chip*, 1(2):102–107, 2001.

[36] P. Belgrader, C. J. Elkin, S. B. Brown, S. N. Nasarabadi, G. D. Marshall, R. G. Langlois, F. P. Milanovich, and B. W. Colston. A reusable flow-through polymerase chain reaction instrument for the continuous monitoring of infectious biological agents. *Anal. Chem.*, 75(14):3446–3450, 2003.

[37] Phillip Belgrader, William Benett, Dean Hadley, Gary Long, Jr. Mariella, Raymond, Fred Milanovich, Shanavaz Nasarabadi, William Nelson, James Richards, and Paul Stratton. Rapid pathogen detection using a microchip pcr array instrument. *Clin Chem*, 44(10):2191–2194, 1998.

[38] M. A. Northrup, B. Benett, D. Hadley, P. Landre, S. Lehew, J. Richards, and P. Stratton. A miniature analytical instrument for nucleic acids based on micromachined silicon reaction chambers. *Anal. Chem.*, 70(5):918–922, 1998.

[39] Y. K. Cho, J. Kim, Y. Lee, Y. A. Kim, K. Namkoong, H. Lim, K. W. Oh, S. Kim, J. Han, C. Park, Y. E. Pak, C. S. Ki, J. R. Choi, H. K. Myeong, and C. Ko. Clinical evaluation of micro-scale chip-based pcr system for rapid detection of hepatitis b virus. *Biosensors & Bioelectronics*, 21(11):2161–2169, 2006.

[40] C. S. Zhang, J. L. Xu, W. L. Ma, and W. L. Zheng. Pcr microfluidic devices for dna amplification. *Biotechnology Advances*, 24(3):243–284, 2006.

[41] J. Liu, M. Enzelberger, and S. Quake. A nanoliter rotary device for polymerase chain reaction. *Electrophoresis*, 23(10):1531–1536, 2002.

[42] A. Gulliksen, L. Solli, F. Karlsen, H. Rogne, E. Hovig, T. Nordstrom, and R. Sirevag. Real-time nucleic acid sequence-based amplification in nanoliter volumes. *Analytical Chemistry*, 76(1):9–14, 2004.

[43] M. Krishnan, D. T. Burke, and M. A. Burns. Polymerase chain reaction in high surface-to-volume ratio sio2 microstructures. *Analytical Chemistry*, 76(22):6588–6593, 2004.

[44] P. Belgrader, S. Young, B. Yuan, M. Primeau, L. A. Christel, F. Pourahmadi, and M. A. Northrup. A battery-powered notebook thermal cycler for rapid multiplex real time pcr analysis. *Analytical Chemistry*, 73(2):286–289, 2001.

[45] J. A. Higgins, S. Nasarabadi, J. S. Karns, D. R. Shelton, M. Cooper, A. Gbakima, and R. P. Koopman. A handheld real time thermal cycler for bacterial pathogen detection. *Biosensors & Bioelectronics*, 18(9):1115–1123, 2003.

[46] N. C. Cady, S. Stelick, M. V. Kunnavakkam, and C. A. Batt. Real-time pcr detection of listeria monocytogenes using an integrated microfluidics platform. *Sensors and Actuators B-Chemical*, 107(1):332–341, 2005.

[47] C. G. J. Schabmueller, J. R. Pollard, A. G. R. Evans, J. S. Wilkinson, G. Ensell, and A. Brunnschweiler. Integrated diode detector and optical fibres for ¡i¿in situ¡/i¿ detection within micromachined polymerase chain reaction chips. *Journal of Micromechanics and Microengineering*, 11(4):329–333, 2001.

[48] D. Baechi, R. Buser, and J. Dual. A high density microchannel network with integrated valves and photodiodes. *Sensors and Actuators a-Physical*, 95(2-3):77–83, 2002.

[49] K. Nath, J. W. Sarosy, J. Hahn, and C. J. Di Como. Effects of ethidium bromide and sybr (r) green i on different polymerase chain reaction systems. *Journal of Biochemical and Biophysical Methods*, 42(1-2):15–29, 2000.

[50] P. T. Monis, S. Giglio, and C. P. Saint. Comparison of syt09 and sybr green i for real-time polymerase chain reaction and investigation of the effect of dye concentration on amplification and dna melting curve analysis. *Analytical Biochemistry*, 340(1):24–34, 2005.

[51] L. J. Kricka and P. Wilding. Microchip pcr. *Analytical and Bioanalytical Chemistry*, 377(5):820–825, 2003.

[52] J. Cheng, M. A. Shoffner, G. E. Hvichia, L. J. Kricka, and P. Wilding. Chip pcr .2. investigation of different pcr amplification systems in microfabricated silicon-glass chips. *Nucleic Acids Research*, 24(2):380–385, 1996.

[53] Y. Matsubara, K. Kerman, M. Kobayashi, S. Yamamura, Y. Morita, and E. Tamiya. Microchamber array based dna quantification and specific sequence detection from a single copy via pcr in nanoliter volumes. *Biosensors Bioelectronics*, 20(8):1482–1490, 2005.

[54] M. A. Cooper. Label-free screening of bio-molecular interactions. *Analytical and Bioanalytical Chemistry*, 377(5):834–842, 2003.

[55] C. Fredriksson, S. Kihlman, M. Rodahl, and B. Kasemo. The piezoelectric quartz crystal mass and dissipation sensor: A means of studying cell adhesion. *Langmuir*, 14(2):248–251, 1998.

[56] M. A. Cooper, F. N. Dultsev, T. Minson, V. P. Ostanin, C. Abell, and D. Klenerman. Direct and sensitive detection of a human virus by rupture event scanning. *Nature Biotechnology*, 19(9):833–837, 2001.

[57] R. Raiteri, M. Grattarola, H. J. Butt, and P. Skladal. Micromechanical cantilever-based biosensors. *Sensors and Actuators B-Chemical*, 79(2-3):115–126, 2001.

[58] T. P. Burg and S. R. Manalis. Suspended microchannel resonators for biomolecular detection. *Applied Physics Letters*, 83(13):2698–2700, 2003.

[59] S. C. Minne, S. R. Manalis, and C. F. Quate. Parallel atomic force microscopy using cantilevers with integrated piezoresistive sensors and integrated piezoelectric actuators. *Applied Physics Letters*, 67(26):3918–20, 1995.

[60] M. Ozsoz, A. Erdem, D. Ozkan, P. Kara, H. Karadeniz, B. Meric, K. Kerman, and S. Girousi. Allele-specific genotyping by using guanine and gold electrochemical oxidation signals. *Bioelectrochemistry*, 67(2):199–203, 2005.

[61] I. V. Yang and H. H. Thorp. Modification of indium tin oxide electrodes with repeat polynucleotides: Electrochemical detection of trinucleotide repeat expansion. *Analytical Chemistry*, 73(21):5316–5322, 2001.

[62] E. M. Boon, D. M. Ceres, T. G. Drummond, M. G. Hill, and J. K. Barton. Mutation detection by electrocatalysis at dna-modified electrodes. *Nature Biotechnology*, 18(10):1096–1100, 2000.

[63] E. Souteyrand, J. P. Cloarec, J. R. Martin, C. Wilson, I. Lawrence, S. Mikkelsen, and M. F. Lawrence. Direct detection of the hybridization of synthetic homo-oligomer dna sequences by field effect. *Journal of Physical Chemistry B*, 101(15):2980–2985, 1997.

[64] J. Fritz, E. B. Cooper, S. Gaudet, P. K. Sorger, and S. R. Manalis. Electronic detection of dna by its intrinsic molecular charge. *Proceedings of the National Academy of Sciences of the United States of America*, 99(22):14142–14146, 2002.

[65] F. Wei, B. Sun, Y. Guo, and X. S. Zhao. Monitoring dna hybridization on alkyl modified silicon surface through capacitance measurement. *Biosensors & Bioelectronics*, 18(9):1157–1163, 2003.

[66] D. S. Kim, Y. T. Jeong, H. J. Park, J. K. Shin, P. Choi, J. H. Lee, and G. Lim. An fet-type charge sensor for highly sensitive detection of dna sequence. *Biosensors & Bioelectronics*, 20(1):69–74, 2004.

[67] F. Uslu, S. Ingebrandt, D. Mayer, S. Bocker-Meffert, M. Odenthal, and A. Offenhausser. Labelfree fully electronic nucleic acid detection system based on

a field-effect transistor device. *Biosensors & Bioelectronics*, 19(12):1723–1731, 2004.

[68] F. Pouthas, C. Gentil, D. Cote, and U. Bockelmann. Dna detection on transistor arrays following mutation-specific enzymatic amplification. *Applied Physics Letters*, 84(9):1594–1596, 2004.

[69] M. J. Schoning and A. Poghossian. Recent advances in biologically sensitive field-effect transistors (biofets). *Analyst*, 127(9):1137–1151, 2002.

[70] J. Hahm and C. M. Lieber. Direct ultrasensitive electrical detection of dna and dna sequence variations using nanowire nanosensors. *Nano Letters*, 4(1):51–54, 2004.

[71] L. Bousse. Single electrode-potentials related to flat-band voltage measurements on eos and mos structures. *Journal of Chemical Physics*, 76(10):5128–5133, 1982.

[72] P. Bergveld. The future of biosensors. *Sensors and Actuators a-Physical*, 56(1-2):65–73, 1996.

[73] D. Kern, M. Collins, T. Fultz, J. Detmer, S. Hamren, J. J. Peterkin, P. Sheridan, M. Urdea, R. White, T. Yeghiazarian, and J. Todd. An enhanced-sensitivity branched-dna assay for quantification of human immunodeficiency virus type 1 rna in plasma. *Journal of Clinical Microbiology*, 34(12):3196–3202, 1996.

[74] J. Kong, N. R. Franklin, C. W. Zhou, M. G. Chapline, S. Peng, K. J. Cho, and H. J. Dai. Nanotube molecular wires as chemical sensors. *Science*, 287(5453):622–625, 2000.

[75] Z. Li, Y. Chen, X. Li, T. I. Kamins, K. Nauka, and R. S. Williams. Sequence-specific label-free dna sensors based on silicon nanowires. *Nano Letters*, 4(2):245–247, 2004.

[76] P. R. Nair and M. A. Alam. Performance limits of nanobiosensors. *Applied Physics Letters*, 88(23), 2006.

[77] G. F. Zheng, F. Patolsky, Y. Cui, W. U. Wang, and C. M. Lieber. Multiplexed electrical detection of cancer markers with nanowire sensor arrays. *Nature Biotechnology*, 23(10):1294–1301, 2005.

[78] P. E. Sheehan and L. J. Whitman. Detection limits for nanoscale biosensors. *Nano Letters*, 5(4):803–807, 2005.

[79] Y. Huang, X. F. Duan, Q. Q. Wei, and C. M. Lieber. Directed assembly of one-dimensional nanostructures into functional networks. *Science*, 291(5504):630–633, 2001.

[80] D. A. Buchanan. Scaling the gate dielectric: Materials, integration, and reliability. *Ibm Journal of Research and Development*, 43(3):245–264, 1999.

[81] E. B. Cooper. *Silicon Field-Effect Sensors for Biomolecular Assays*. PhD thesis, Massachusetts Institute of Technology, 2003.

[82] A.G. Mayes. Immobilization chemistry of biological recognition molecules. In E. Gizeli and C. Lowe, editors, *Biomolecular Sensors*. Taylor & Francis, London, 2002.

[83] Gero Decher. Fuzzy nanoassemblies: Toward layered polymeric multicomposites. *Science*, 277(5330):1232–1237, 1997.

[84] J. Zhang, B. Senger, D. Vautier, C. Picart, P. Schaaf, J. C. Voegel, and P. Lavalle. Natural polyelectrolyte films based on layer-by layer deposition of collagen and hyaluronic acid. *Biomaterials*, 26(16):3353–3361, 2005.

[85] M. F. Durstock and M. F. Rubner. Dielectric properties of polyelectrolyte multilayers. *Langmuir*, 17(25):7865–7872, 2001.

[86] J. J. Harris, J. L. Stair, and M. L. Bruening. Layered polyelectrolyte films as selective, ultrathin barriers for anion transport. *Chemistry of Materials*, 12(7):1941–1946, 2000.

[87] J. J. Harris and M. L. Bruening. Electrochemical and in situ ellipsometric investigation of the permeability and stability of layered polyelectrolyte films. *Langmuir*, 16(4):2006–2013, 2000.

[88] J. H. Dai, A. W. Jensen, D. K. Mohanty, J. Erndt, and M. L. Bruening. Controlling the permeability of multilayered polyelectrolyte films through derivatization, cross-linking, and hydrolysis. *Langmuir*, 17(3):931–937, 2001.

[89] A. A. Antipov, G. B. Sukhorukov, E. Donath, and H. Mohwald. Sustained release properties of polyelectrolyte multilayer capsules. *Journal of Physical Chemistry B*, 105(12):2281–2284, 2001.

[90] G. B. Sukhorukov, E. Donath, H. Lichtenfeld, E. Knippel, M. Knippel, A. Budde, and H. Mohwald. Layer-by-layer self assembly of polyelectrolytes on colloidal particles. *Colloids and Surfaces a-Physicochemical and Engineering Aspects*, 137(1-3):253–266, 1998.

[91] J. B. Schlenoff, H. Ly, and M. Li. Charge and mass balance in polyelectrolyte multilayers. *Journal of the American Chemical Society*, 120(30):7626–7634, 1998.

[92] T. R. Farhat and J. B. Schlenoff. Ion transport and equilibria in polyelectrolyte multilayers. *Langmuir*, 17(4):1184–1192, 2001.

[93] M. J. Deen, M. W. Shinwari, J. C. Ranuarez, and D. Landheer. Noise considerations in field-effect biosensors. *Journal of Applied Physics*, 100(7), 2006.

[94] D. Landheer, G. Aers, W. R. McKinnon, M. J. Deen, and J. C. Ranuarez. Model for the field effect from layers of biological macromolecules on the gates of metal-oxide-semiconductor transistors. *Journal of Applied Physics*, 98(4), 2005.

[95] K. Nortemann, J. Hilland, and U. Kaatze. Dielectric properties of aqueous nacl solutions at microwave frequencies. *Journal of Physical Chemistry A*, 101(37):6864–6869, 1997.

[96] G. Decher, J. D. Hong, and J. Schmitt. Buildup of ultrathin multilayer films by a self-assembly process .3. consecutively alternating adsorption of anionic and cationic polyelectrolytes on charged surfaces. *Thin Solid Films*, 210(1-2):831–835, 1992.

[97] M. Schonhoff and O. Soderman. Pfg-nmr diffusion as a method to investigate the equilibrium adsorption dynamics of surfactants at the solid/liquid interface. *Journal of Physical Chemistry B*, 101(41):8237–8242, 1997.

[98] G. B. Sukhorukov, E. Donath, S. Davis, H. Lichtenfeld, F. Caruso, V. I. Popov, and H. Mohwald. Stepwise polyelectrolyte assembly on particle surfaces: a novel approach to colloid design. *Polymers for Advanced Technologies*, 9(10-11):759–767, 1998.

[99] G. Ladam, P. Schaad, J. C. Voegel, P. Schaaf, G. Decher, and F. Cuisinier. In situ determination of the structural properties of initially deposited polyelectrolyte multilayers. *Langmuir*, 16(3):1249–1255, 2000.

[100] A. F. Xie and S. Granick. Local electrostatics within a polyelectrolyte multilayer with embedded weak polyelectrolyte. *Macromolecules*, 35(5):1805–1813, 2002.

[101] M. Schonhoff. Self-assembled polyelectrolyte multilayers. *Current Opinion in Colloid & Interface Science*, 8(1):86–95, 2003.

[102] Y. Lvov, G. Decher, and H. Mohwald. Assembly, structural characterization, and thermal-behavior of layer-by-layer deposited ultrathin films of poly(vinyl sulfate) and poly(allylamine). *Langmuir*, 9(2):481–486, 1993.

[103] F. Caruso, K. Niikura, D. N. Furlong, and Y. Okahata. Ultrathin multilayer polyelectrolyte films on gold: Construction and thickness determination .1. *Langmuir*, 13(13):3422–3426, 1997.

[104] P. Lavalle, C. Gergely, F. J. G. Cuisinier, G. Decher, P. Schaaf, J. C. Voegel, and C. Picart. Comparison of the structure of polyelectrolyte multilayer films exhibiting a linear and an exponential growth regime: An in situ atomic force microscopy study. *Macromolecules*, 35(11):4458–4465, 2002.

[105] J. Ruths, F. Essler, G. Decher, and H. Riegler. Polyelectrolytes i: Polyanion/polycation multilayers at the air/monolayer/water interface as elements for quantitative polymer adsorption studies and preparation of hetero-superlattices on solid surfaces. *Langmuir*, 16(23):8871–8878, 2000.

[106] M. Losche, J. Schmitt, G. Decher, W. G. Bouwman, and K. Kjaer. Detailed structure of molecularly thin polyelectrolyte multilayer films on solid substrates as revealed by neutron reflectometry. *Macromolecules*, 31(25):8893–8906, 1998.

[107] S. T. Dubas and J. B. Schlenoff. Factors controlling the growth of polyelectrolyte multilayers. *Macromolecules*, 32(24):8153–8160, 1999.

[108] G. Ladam, P. Schaad, J. C. Voegel, P. Schaaf, G. Decher, and F. Cuisinier. In situ determination of the structural properties of initially deposited polyelectrolyte multilayers. *Langmuir*, 16(3):1249–1255, 2000.

[109] E. Donath, D. Walther, V. N. Shilov, E. Knippel, A. Budde, K. Lowack, C. A. Helm, and H. Mohwald. Nonlinear hairy layer theory of electrophoretic fingerprinting applied to consecutive layer by layer polyelectrolyte adsorption onto charged polystyrene latex particles. *Langmuir*, 13(20):5294–5305, 1997.

[110] B. Schwarz and M. Schonhoff. A h-1 nmr relaxation study of hydration water in polyelectrolyte mono and multilayers adsorbed to colloidal particles. *Colloids and Surfaces a-Physicochemical and Engineering Aspects*, 198:293–304, 2002.

[111] A. Plech, T. Salditt, C. Munster, and J. Peisl. Investigation of structure and growth of self-assembled polyelectrolyte layers by x-ray and neutron scattering under grazing angles. *Journal of Colloid and Interface Science*, 223(1):74–82, 2000.

[112] M. Schonhoff. Layered polyelectrolyte complexes: physics of formation and molecular properties. *Journal of Physics-Condensed Matter*, 15(49):R1781–R1808, 2003.

[113] D. Finkenstadt and D. D. Johnson. Model of ionization response of weak polyacids in a layered polyelectrolyte self-assembly. *Langmuir*, 18(4):1433–1436, 2002.

[114] D. Korneev, Y. Lvov, G. Decher, J. Schmitt, and S. Yaradaikin. Neutron reflectivity analysis of self-assembled film superlattices with alternate layers of deuterated and hydrogenated polysterenesulfonate and polyallylamine. *Physica B*, 213:954–956, 1995.

[115] M. Muller, M. Brissova, T. Rieser, A. C. Powers, and K. Lunkwitz. Deposition and properties of polyelectrolyte multilayers studied by atr-ftir spectroscopy. *Materials Science & Engineering C-Biomimetic and Supramolecular Systems*, 8-9:163–169, 1999.

[116] B. Schwarz and M. Schonhoff. Surface potential driven swelling of polyelectrolyte multilayers. *Langmuir*, 18(8):2964–2966, 2002.

[117] M. Castelnovo and J. F. Joanny. Formation of polyelectrolyte multilayers. *Langmuir*, 16(19):7524–7532, 2000.

[118] A. Shafir and D. Andelman. Polyelectrolyte adsorption: Chemical and electrostatic interactions. *Physical Review E*, 70(6), 2004.

[119] R. R. Netz and J. F. Joanny. Adsorption of semiflexible polyelectrolytes on charged planar surfaces: Charge compensation, charge reversal, and multilayer formation. *Macromolecules*, 32(26):9013–9025, 1999.

[120] O. Henegariu, N. A. Heerema, S. R. Dlouhy, G. H. Vance, and P. H. Vogt. Multiplex pcr: Critical parameters and step-by-step protocol. *Biotechniques*, 23(3):504–511, 1997.

[121] R. K. Saiki. Optimization of polymerase chain reaction. In H. A. Erlich, R. Gibbs, and H. H. Kazazian Jr., editors, *Current Communications in Molecular Biology*. CSH Laboratory Press, Cold Spring Harbor, NY, 1989.

[122] P. M. Howley, M. A. Israel, M. F. Law, and M. A. Martin. Rapid method for detecting and mapping homology between heterologous dnas - evaluation of polyomavirus genomes. *Journal of Biological Chemistry*, 254(11):4876–4883, 1979.

[123] J. SantaLucia. A unified view of polymer, dumbbell, and oligonucleotide dna nearest-neighbor thermodynamics. *Proceedings of the National Academy of Sciences of the United States of America*, 95(4):1460–1465, 1998.

[124] N. von Ahsen, M. Oellerich, V. W. Armstrong, and E. Schutz. Application of a thermodynamic nearest-neighbor model to estimate nucleic acid stability and optimize probe design: Prediction of melting points of multiple mutations of apolipoprotein b-3500 and factor v with a hybridization probe genotyping assay on the lightcycler. *Clinical Chemistry*, 45(12):2094–2101, 1999.

[125] P. R. Russo. Integrated silicon field-effect sensors and microfluidics for biomolecular detection. Master's thesis, Massachusetts Institute of Technology, 2004.

[126] J. Plummer, M. Deal, and P. Griffin. *Silicon VLSI Technology: Fundamentals, Practice and Modeling*. Prentice Hall, Upper Saddle River, NJ, 2000.

[127] M. U. Kopp, A. J. de Mello, and A. Manz. Chemical amplification: Continuous-flow pcr on a chip. *Science*, 280(5366):1046–1048, 1998.

[128] C. Grosjean, X. Yang, and Y.-C. Tai. A thermopneumatic microfluidic system. In *The Fifteenth IEEE International Conference on Micro Electro Mechanical Systems, 2002*, pages 24–27, 2002.

[129] T. L. Loh. Integrated microfluidics, heaters, and electronic sensors for lab-on-a-chip applications. Master's thesis, Massachusetts Institute of Technology, 2005.

[130] C. L. Hansen, M. O. A. Sommer, and S. R. Quake. Systematic investigation of protein phase behavior with a microfluidic formulator. *Proceedings of the National Academy of Sciences of the United States of America*, 101(40):14431–14436, 2004.

[131] M. A. Unger, H. P. Chou, T. Thorsen, A. Scherer, and S. R. Quake. Monolithic microfabricated valves and pumps by multilayer soft lithography. *Science*, 288(5463):113–116, 2000.

[132] X. Yang, C. Grosjean, and Y. C. Tai. Design, fabrication, and testing of micromachined silicone rubber membrane valves. *Journal of Microelectromechanical Systems*, 8(4):393–402, 1999.

[133] W. H. Grover, A. M. Skelley, C. N. Liu, E. T. Lagally, and R. A. Mathies. Monolithic membrane valves and diaphragm pumps for practical large-scale integration into glass microfluidic devices. *Sensors and Actuators B-Chemical*, 89(3):315–323, 2003.

[134] H. Yang, C.-K. Chao, and C. P. Lin. Micro-ball lens array modeling and fabrication using thermal reflow in two polymer layers. *Journal of Micromechanics and Microengineering*, 14(2):277–282, 2004.

[135] J. Voldman. A microfabricated liquid mixer for biomedical applications. Master's thesis, Massachusetts Institute of Technology, 1997.

[136] D. E. Yates, S. Levine, and T. W. Healy. Site-binding model of electrical double-layer at oxide-water interface. *Journal of the Chemical Society-Faraday Transactions I*, 70:1807–1818, 1974.

[137] Y. G. Vlasov, Y. A. Tarantov, and P. V. Bobrov. Analytical characteristics and sensitivity mechanisms of electrolyte-insulator-semiconductor system-based chemical sensors - a critical review. *Analytical and Bioanalytical Chemistry*, 376(6):788–796, 2003.

[138] C. Cane, I. Gracia, and A. Merlos. Microtechnologies for ph isfet chemical sensors. *Microelectronics Journal*, 28(4):389–405, 1997.

[139] R. E. G. vanHal, J. C. T. Eijkel, and P. Bergveld. A general model to describe the electrostatic potential at electrolyte oxide interfaces. *Advances in Colloid and Interface Science*, 69:31–62, 1996.

[140] R. Wiberga and N. Lior. Errors in thermochromic liquid crystal thermometry. *Review of Scientific Instruments*, 75(9):2985–2994, 2004.

[141] D. Ross, M. Gaitan, and L. E. Locascio. Temperature measurement in microfluidic systems using a temperature-dependent fluorescent dye. *Analytical Chemistry*, 73(17):4117–4123, 2001.

[142] G. I. Taylor. Dispersion of soluble matter in solvent flowing slowly through a tube. In *Proceedings ofthe Royal Society of London Series A - Mathematical and Physical Sciences*, volume 219, pages 186–203, 1953.

[143] T. Wink, J. de Beer, W. E. Hennink, A. Bult, and W. P. van Bennekom. Interaction between plasmid dna and cationic polymers studied by surface plasmon resonance spectrometry. *Analytical Chemistry*, 71(4):801–805, 1999.

[144] D. F. Yao, J. Kim, F. Yu, P. E. Nielsen, E. K. Sinner, and W. Knoll. Surface density dependence of pcr amplicon hybridization on pna/dna probe layers. *Biophysical Journal*, 88(4):2745–2751, 2005.

[145] C. Picart, J. Mutterer, L. Richert, Y. Luo, G. D. Prestwich, P. Schaaf, J. C. Voegel, and P. Lavalle. Molecular basis for the explanation of the exponential growth of polyelectrolyte multilayers. *Proceedings of the National Academy of Sciences of the United States of America*, 99(20):12531–12535, 2002.

[146] Michael A. Innis and David H. Gelfand. Optimization of pcrs. In Michael A. Innis, David H. Gelfand, and John J. Sninsky, editors, *PCR applications : protocols for functional genomics*, pages 3–13. Academic Press, San Diego, 1990.

[147] S. Cheng, C. Fockler, W. M. Barnes, and R. Higuchi. Effective amplification of long targets from cloned inserts and human genomic dna. *PNAS*, 91(12):5695–5699, 1994.

[148] C. H. Fan, K. W. Plaxco, and A. J. Heeger. Electrochemical interrogation of conformational changes as a reagentless method for the sequence-specific detection of dna. *Proceedings of the National Academy of Sciences of the United States of America*, 100(16):9134–9137, 2003.

[149] W. C. Dunn, S. C. Jacobson, L. C. Waters, N. Kroutchinina, J. Khandurina, R. S. Foote, M. J. Justice, L. J. Stubbs, and J. M. Ramsey. Pcr amplification and analysis of simple sequence length polymorphisms in mouse dna using a single microchip device. *Analytical Biochemistry*, 277(1):157–160, 2000.

[150] B. C. Giordano, E. R. Copeland, and J. P. Landers. Towards dynamic coating of glass microchip chambers for amplifying dna via the polymerase chain reaction. *Electrophoresis*, 22(2):334–340, 2001.

[151] J. N. Yang, Y. J. Liu, C. B. Rauch, R. L. Stevens, R. H. Liu, R. Lenigk, and P. Grodzinski. High sensitivity pcr assay in plastic micro reactors. *Lab on a Chip*, 2(4):179–187, 2002.

[152] M. A. Shoffner, J. Cheng, G. E. Hvichia, L. J. Kricka, and P. Wilding. Chip pcr .1. surface passivation of microfabricated silicon-glass chips for pcr. *Nucleic Acids Research*, 24(2):375–379, 1996.

[153] B. Huang, H. K. Wu, S. Kim, and R. N. Zare. Coating of poly(dimethylsiloxane) with n-dodecyl-beta-d-maltoside to minimize nonspecific protein adsorption. *Lab on a Chip*, 5(10):1005–1007, 2005.

[154] L. Zhang, P. Somasundaran, and C. Maltesh. Adsorption of n-dodecyl-beta-d-maltoside on solids. *Journal of Colloid and Interface Science*, 191(1):202–208, 1997.

[155] J. Goulpeau, D. Trouchet, A. Ajdari, and P. Tabeling. Experimental study and modeling of polydimethylsiloxane peristaltic micropumps. *Journal of Applied Physics*, 98(4), 2005.

[156] George J. Despotis, Glenn Gravlee, Kriton Filos, and Jerrold Levy. Anticoagulation monitoring during cardiac surgery: A review of current and emerging techniques. *Anesthesiology*, 91(4):1122–1151, 1999.

[157] Jack Hirsh and Agnes Y. Y. Lee. How we diagnose and treat deep vein thrombosis. *Blood*, 99(9):3102–3110, 2002.

[158] D.L. Rabenstein. Heparin and heparan sulfate: structure and function. *Nat. Prod. Rep.*, 19:312–331, 2002.

[159] L. Roden. Heparin; chemical and biological properties, clinical applications. In *Heparin; Chemical and Biological Properties, Clinical Applications*, Heparin; Chemical and Biological Properties, Clinical Applications, pages 81–96. CRC Press, Inc, Boca Raton, FL, 1989.

[160] U.R. Desai, M. Petitou, I. Bjork, and S.T. Olson. Mechanism of heparin activation of antithrombin. role of individual residues of the pentasaccharide activating sequence in the recognition of native and activated states of antithrombin. *J. Biol. Chem.*, 273:7478–87, 1998.

[161] Lei Jin, Jan Pieter Abrahams, Richard Skinner, Maurice Petitou, Robert N. Pike, and Robin W. Carrell. The anticoagulant activation of antithrombin byeparin. *Proc. Natl. Acad. Sci. USA*, 94(26):14683–14688, 1997.

[162] Zachary Shriver, Rahul Raman, Ganesh Venkataraman, Katherine Drummond, Jeremy Turnbull, Toshihiko Toida, Robert Linhardt, Klaus Biemann, and Ram Sasisekharan. From the cover: Sequencing of 3-o sulfate containing heparin decasaccharides with a partial antithrombin iii binding site 10.1073/pnas.97.19.10359. *Proc. Natl. Acad. Sci. USA*, 97(19):10359–10364, 2000.

[163] R. Sasisekharan, Z. Shriver, G. Venkataraman, and U. Narayanasami. Roles of heparan-sulphate glycosaminoglycans in cancer. *Nat Rev Cancer*, 2(7):521–8, 2002.

[164] U. Hacker, K. Nybakken, and N. Perrimon. Heparan sulphate proteoglycans: the sweet side of development. *Nat Rev Mol Cell Biol*, 6(7):530–41, 2005.

[165] P. Gallay. Syndecans and hiv-1 pathogenesis. *Microbes Infect*, 6(6):617–22, 2004.

[166] Mallik Sundaram, Yiwei Qi, Zachary Shriver, Dongfang Liu, Ganlin Zhao, Ganesh Venkataraman, Robert Langer, and Ram Sasisekharan. Rational design of low-molecular weight heparins with improved invivo activity 10.1073/pnas.252643299. *Proceedings of the National Academy of Sciences of the United States of America*, 100(2):651–656, 2003.

[167] B. Casu and G. Torri. Structural characterization of low molecular weight heparins. *Seminars in Thrombosis and Hemostasis*, 25:17–25, 1999.

[168] T. Ando, M Yamsaki, and K Suzuki. Protamine. In *Molecular Biology Biochemistry and Biophysics,*, pages 1–109. Springer-Verlag, New York, 1973.

[169] B. Kaiser, D. A. Hoppensteadt, and J. Fareed. Tissue factor pathway inhibitor: an update of potential implications in the treatment of cardiovascular disorders. *Expert Opinion on Investigational Drugs*, 10(11):1925–1935, 2001.

[170] R. D. Hull and G. F. Pineo. Low-molecular-weight heparin treatment of venous thromboembolism. *Progress in Cardiovascular Diseases*, 37(2):71–78, 1994.

[171] M. Petitou and C. A. A. van Boeckel. A synthetic antithrombin iii binding pentasaccharide is now a drug! what comes next? *Angewandte Chemie-International Edition*, 43(24):3118–3133, 2004.

[172] M. Makris, R. E. Hough, and S. Kitchen. Poor reversal of low molecular weight heparin by protamine. *British Journal of Haematology*, 108(4):884–885, 2000.

[173] R. A. Kadakia, S. R. Baimeedi, and J. J. Ferguson. Low-molecular-weight heparins in the cardiac catheterization laboratory. *Texas Heart Institute Journal*, 31(1):72–83, 2004.

[174] P. D. Raymond, M. J. Ray, S. N. Callen, and N. A. Marsh. Heparin monitoring during cardiac surgery. part 1: validation of whole-blood heparin concentration and activated clotting time. *Perfusion-Uk*, 18(5):269–276, 2003.

[175] S. Kitchen. Problems in laboratory monitoring of heparin dosage. *British Journal of Haematology*, 111(2):397–406, 2000.

[176] M. N. Levine, J. Hirsh, M. Gent, A. G. Turpie, M. Cruickshank, J. Weitz, D. Anderson, and M. Johnson. A randomized trial comparing activated thromboplastin time with heparin assay in patients with acute venous thromboembolism requiring large daily doses of heparin. *Archives of Internal Medicine*, 154(1):49–56, 1994.

[177] D. R. Jobes, G. L. Aitken, and G. W. Shaffer. Increased accuracy and precision of heparin and protamine dosing reduces blood-loss and transfusion in patients undergoing patients cardiac operations. *Journal of Thoracic and Cardiovascular Surgery*, 110(1):36–45, 1995.

[178] R. Jelinek and S. Kolusheva. Carbohydrate biosensors. *Chemical Reviews*, 104(12):5987–6015, 2004.

[179] J. C. Vankerkhof, P. Bergveld, and R. B. M. Schasfoort. The isfet based heparin sensor with a monolayer of protamine as affinity ligand. *Biosensors & Bioelectronics*, 10(3-4):269–282, 1995.

[180] M. Houska, E. Brynda, and K. Bohata. The effect of polyelectrolyte chain length on layer-by-layer protein/polyelectrolyte assembly-an experimental study. *Journal of Colloid and Interface Science*, 273(1):140–147, 2004.

[181] M. Houska and E. Brynda. Interactions of proteins with polyelectrolytes at solid/liquid interfaces: Sequential adsorption of albumin and heparin. *Journal of Colloid and Interface Science*, 188(2):243–250, 1997.

[182] R. K. Hallberg and P. L. Dubin. Effect of ph on the binding of beta-lactoglobulin to sodium polystyrenesulfonate. *Journal of Physical Chemistry B*, 102(43):8629–8633, 1998.

[183] J. H. Yun, S. C. Ma, B. Fu, V. C. Yang, and M. E. Meyerhoff. Direct potentiometric membrane-electrode measurements of heparin-binding to macromolecules. *Electroanalysis*, 5(9-10):719–724, 1993.

[184] J. I. Weitz. Low-molecular-weight heparins. *New England Journal of Medicine*, 337(10):688–698, 1997.

[185] N. M. Milovic, J. R. Behr, M. Godin, C. S. J. Hou, K. R. Payer, A. Chandrasekaran, P. R. Russo, R. Sasisekharan, and S. R. Manalis. Monitoring of heparin and its low-molecular-weight analogs by silicon field effect. *Proceedings of the National Academy of Sciences of the United States of America*, 103(36):13374–13379, 2006.

[186] Chih-Sheng Johnson Hou, Nebojsa Milovic, Michel Godin, Peter R. Russo, Raj Chakrabarti, and Scott R. Manalis. Label-free microelectronic pcr quantification. *Analytical Chemistry*, 78(8):2526–2531, 2006.

[187] Chih-Sheng Johnson Hou, Michel Godin, Kristopher Payer, Raj Chakrabarti, and Scott R. Manalis. Integrated microelectronic device for label-free nucleic acid amplification and detection. *Lab on a Chip*, in press.